POLITECNICO DI MILANO

Dept. of Environmental, Hydraulic, Infrastructures and Surveying Engineering

Doctoral programme in Environmental and Infrastructure Engineering

XXIV Cycle (2009-2011)

EARTH SURFACE DEFORMATION AND ELEVATION FIELDS FROM DIFFERENT OBSERVATION TECHNIQUES: VALIDATION AND FUSION PROBLEMS

Doctoral Dissertation of

Maddalena GILARDONI

Student Id. 738793

Supervisor: Ing. Giovanna VENUTI

Tutor: Prof. Fernando SANSÒ

The Chair of Doctoral programme: Prof. Fernando SANSÒ

Abstract

The validation of novel Earth observations from satellite borne sensors is an actual and important issue for the scientific community. The exploitation of the large amount of data coming from space requires their accuracy assessment by comparison with well consolidated satellite or ground based techniques. This is the case of the SAR products, different either for the kind of sensors used or for the mission characteristics or for the kind of data and data processing.
This thesis collects the results obtained in the framework of two different projects both funded by the Italian Space Agency in tackling the above problem. In the first case data come from the ENVISAT satellite mission, and the products under analysis are DInSAR time series of deformations, in the second case data come from the COSMO-SkyMed satellite mission and the products are radargrammetry digital surface models, DSMs.
The focus of the work is on the comparison strategies rather than on the validation results themselves. In order to make different observations of a same phenomenon comparable, they have to be transformed, very often predicted in space and time, thus introducing errors. Of course it is possible to design validation campaigns in such a way to avoid as much as possible a subsequent data manipulation (for instance making reference observations in the same place and simultaneously with respect to those under evaluation) but very often already existent datasets are used and the way to compare them is to be defined.
A general formulation of the problem would be that of finding the transformation which minimize those errors. This approach was initially pursued by giving a stochastic interpretation to the observations and invoking as optimality principle that of minimizing the variance of prediction errors. The solution found, however, requires an observations behaviour that is not obeyed in the actual world unless some data pre-processing is applied. Different ad hoc solutions were therefore adopted and a-posteriori compared. The question is still open, but some key elements have been pointed out.
This dissertation reflects in part the way we approached the problem: a general

introduction is given on stochastic fields modelling as well as on collocation and kriging prediction techniques and a general optimal validation procedure is presented. Then the two real cases we dealt with within MORFEO and COSMO-SkyMed are presented, each in a different part of the manuscript. After recalling the techniques used in the former case to monitor landslide deformations and in the latter to produce digital surface models, the data handling is described. The strategies adopted are then introduced and compared by using a reference DSM as benchmark. Finally the results are reported both in terms of evaluating strategies and in terms of validation results.

More precisely, within the ASI MORFEO project the main goal was to find a procedure to validate deformation time series obtained using two DInSAR algorithms (SBAS developed by the IREA of Naples and SPINUA developed by Politecnico of Bari). The validation was done making a local comparison of LOS deformation values and LOS deformation velocities between SBAS and SPINUA time series themselves, and between independent time series derived from GPS observations on the landslide of Ivancich (Assisi, central Italy). This study area was selected because already monitored by SAR and GPS from several years. The comparison was performed at a local level since the deformation field irregularity makes the spatial-temporal prediction error so high to compromise the result of the validation itself. More precisely, the deformation velocity of each GPS point was compared with the velocity of the three nearest SAR permanent scatterers and the cross-comparison between SBAS and SPINUA was done per areas of homogeneous deformation behaviour, testing the equality between the mean deformation velocities of the two datasets.
One of the limit of the comparison procedure is in the GPS dataset used as truth: it revealed to have a too poor accuracy for the validation purpose. It would be necessary to: select GPS stations in areas with high density of permanent scatterers, and recognized to be zones of homogeneous deformation behaviour (GPS permanent stations would be preferable), locate SAR corner reflectors near GPS stations to avoid additional interpolation errors, make more measurement campaigns with sessions longer than 24 hours in order to obtain very accurate coordinate estimates (few millimeters).
Regarding SPINUA and SBAS cross-comparison, statistical tests on mean velocities in areas with homogeneous behaviour show that the two algorithms, when applied to the same image dataset and after a planimetric bias correction see a statistically equal deformation movement.

To what concern height fields, namely the COSMO-SkyMed project, the purpose was to find a methodology to validate and merge together different

DSMs of comparable accuracy; the work was performed on a test area located near the city of Como on ASTER and SRTM height models, used as test fields, in view to be applied to COSMO-SkyMed products initially not available to the project.
The validation was performed in two ways always on the grid of the DSM under analysis: an internal validation permits to identify and remove outliers on the base of their statistical behaviour with respect to their neighbours; both the model resulted to have a very low percentage of outliers (lower then 1%). After that, an external validation procedure was defined; it consists in a proper comparison with a higher precision DSM taken as reference, in this case it has been considered a LiDAR DSM. The estimated accuracies of ASTER and SRTM agreed with those found in literature.
Subsequently, different methodologies for merging different DSMs, with comparable accuracy and resolution, were tested. In particular, a generalized collocation procedure to make predictions of the height field or of its linear functional from different functionals of the field itself was implemented. This technique was applied to merge the point-wise ASTER DSM with 30m resolution and the average SRTM DSM with 90m resolution either to produce an average DSM on the SRTM grid or a point-wise DSM on the ASTER grid. The final DSM is as or more accurate than the original one. However this strategy is strongly penalized by the empirical estimation of the covariance function as well as by data managing problems. One has always to select areas with a homogeneous behaviour, to be treated separately. This choice is quite arbitrary and heavy.
Merging strategies based on morphology dependent weighted average between height values referred to a same grid were finally adopted, as they prove to be more efficient than weighted average based on global constant weights.
Once the products of COSMO-SkyMed were made available within the project, the procedure to validate and merge different datasets were partially applied to create a DSM starting from sparse point coordinates, computed applying radargrammetry to ascending and descending COSMO-SkyMed stereo-pairs in two test areas near the city of Como (northern Italy).
The results showed that applying the radargrammetric approach to COSMO SkyMed Spotlight images is worthy; DSMs with an accuracy of about 7-8m with a resolution of 5m x 5m can be obtained. These DSMs could be used to improve and detail the SRTM DSM, freely available all over the world; to this aim the developed generalized collocation technique could represent an useful tool.

Contents

Introduction

This dissertation reports the work done by the author within two projects: MORFEO and COSMO-SkyMed.
MORFEO (the acronym stands for "MOnitoraggio del Rischio da Frana utilizzando dati EO" that in English is "Monitoring land slide risk exploiting Earth observation technology") was a project financed by the Italian Space Agency (ASI) which lasted three years and ended in November 2010. The goal of the project was the integration of traditional field information with satellite data to increase the capability of mapping, monitoring and forecasting landslide events (ASI [2011], Guzzetti et al. [2009a]). In particular, our group had to tackle the problem of validation of deformation time series obtained from SAR-ENVISAT images with independent GNSS data.
COSMO-SkyMed (ASI [2007]) is a project, financed by ASI, which exploits data coming from four satellites (the last one was launched on November 6^{th}, 2010) equipped with high resolution SAR sensors operating in X band and endowed with innovative and flexible data acquisition and transmission systems; new digital terrain models and deformation maps will be produced both at regional and local scale from those data. Within this project our group had to validate the new digital terrain models against ones with higher accuracy and resolution and eventually merge them to obtain an improved model.

A mathematical interpretation of the two problems is the following: the same field is observed by two different techniques, at different times, in different positions, with different accuracies. How can we use one observation set to validate the other one, namely to say that this latter is observing the same field of the former one? Deterministic and random fields theory can be exploited to make predictions of the common field from the two datasets in such a way to make them comparable. Statistical tests will be then applied to the validation purposes.

We studied this validation problem both on a theoretical basis, by assuming to deal with a homogeneous and isotropic random field, and on a more practical way, by taking into account the peculiar nature of the available datasets.

This thesis begins with an introductory overview on fields with an emphasis on their stochastic modelling (**Chapter 1**). We then come to the particular cases of the MORFEO (**Part I**) and the COSMO-SkyMed (**Part II**) projects, the first related to a deformation field, the second to an height one. In both cases, we firstly describe the data nature: the characteristics of the considered field and the kind of observations used in the comparison and then the procedures applied to the validation purposes.
This dissertation is organized as follows.
Chapter 1 reports an introduction about fields and the way they are described. This Chapter also includes a part dedicated to the description of predictors and in particular to collocation and kriging. Prediction is an important element because to compare two datasets it is necessary they refer to the same time-spatial position. In **Chapter 2** the work carried out within the MORFEO project is described. **Appendix A** describes an optimal validation technique developed within this project.
With **Chapter 3** begins the second part of the thesis devoted to the work done within the COSMO-SkyMed project. This Chapter reports an overview regarding Digital Elevation Models, the techniques used to acquire data and a description of the available DSMs in the study area. **Chapter 4** illustrates the developed validation procedure while **Chapter 5** the problem of fusion of different DSMs. **Chapter 6** is dedicated to the study of DSMs from radargrammetry and in particular to the methods that can be used to create DSMs starting from sparse point height information.
Conclusions will end this document.

Chapter 1

Fields

In this Chapter some basic notations regarding fields are introduced. The validation and fusion problems we have to face are in fact solved by exploiting the fields theory. The same field is observed in different ways, and field prediction and transformation techniques are needed to derive comparable values. The emphasis is here on the stochastic field theory because it is useful to better understand most of the data processing. In Section 1.1 a general reasoning on how to model a field is described. It follows a focus on the problem of predicting the stochastic part of a field: Section 1.2 reports some basic theory, Section 1.3 illustrates the Wiener-Kolmogorov principle, Section 1.4 and Section 1.5 describe collocation and kriging which apply this principle.

1.1 The prediction problem

Natural fields are often subjected to not perfectly known laws and their geometric and material structure is usually variable in a way that cannot be precisely defined. As a result, even a very detailed and precise knowledge of the field $F(\underline{t})$ at many points $\underline{t}_1, \ldots, \underline{t}_M$ will leave room for an unpredictable variation when moving to a new point $\underline{t}$.
Therefore, very much as in statistics, an empirical approach has to be adopted trying to learn from observations how the field $F(\underline{t})$ behaves and use this information to make predictions.
Let us start with a classification of possible components of $F(\underline{t})$ which can be useful to the empirical analysis of its observations.
Assuming that the domain D, on which the observations are given, has a diameter Δ defined as:

$$\Delta = \max_{\underline{t}_1 \underline{t}_2 \in D} |\underline{t}_2 - \underline{t}_1| \tag{1.1}$$

where $|\underline{t}_2 - \underline{t}_1|$ can be the Euclidean distance between two points but also a different distance.
Assume further that the observations are given at M points $\underline{t}_i, i = 1, 2, \ldots, M$ with a mean distance $\bar{d}$ defined as:

$$\bar{d} = \frac{1}{M} \sum_{i=1}^{M} |\underline{t}_i - \underline{t}_{n(i)}| \tag{1.2}$$

where $t_{n(i)}$ is the nearest neighbour of $\underline{t}_i$ such that:

$$|\underline{t}_i - \underline{t}_{n(i)}| \leq |\underline{t}_i - \underline{t}_j| \quad \forall j \neq i \tag{1.3}$$

The field $F(\underline{t})$ can be in general split into four components:

$$F(\underline{t}) = T(\underline{t}) + P(\underline{t}) + R(\underline{t}) + S(\underline{t}) \tag{1.4}$$

$T(\underline{t})$ is the trend component and it represents a significant variation of $F(\underline{t})$ on the scale of Δ. Typically $T(\underline{t})$ is represented by a polynomial of some order p.
$P(\underline{t})$ is the periodic component, on scales comparable to Δ. This component can be represented by means of a Fourier basis up to some maximum frequency N.
The regional component $R(\underline{t})$ represents localized effects, with a resolution that can be around $\frac{1}{10}\Delta$. It is typically reconstructed by combining splines, i.e. functions with limited support, translated to the centres of a regular grid.
So $T(\underline{t})$, $P(\underline{t})$ and $R(\underline{t})$ represent the deterministic part of the field while $S(\underline{t})$ is the stochastic or random component of $F(\underline{t})$.
$S(\underline{t})$ is considered as a sample from a random function defined by some probability distribution on a suitable space containing all the possible signals $S(\underline{t})$.
A prediction theory is developed on the basis of simple hypotheses regarding the stochastic behaviour of the field as presented in Section 1.3. Of course representation 1.4 does not apply to all cases. There might be cases in which one or more components are not present, or where there is no clear-cut separation between one and the other. Therefore a parsimony criterion has to be followed in constructing the empirical model: a simpler model is always preferable to a richer one even if it leaves larger residuals. Furthermore it is convenient to follow a stepwise strategy, where one component at a time is estimated via least squares, and the residuals of this estimation are considered as new observations where the next component has to be sought. Here we focus our attention on the description of the stochastic part of the field and on the methods available to make a prediction of the random field at any point t; they will be recalled frequently in this thesis.

1.2 Basic definitions and notations

1.2.1 Random functions

Let T be a subset of $\Re^n (n = 1, 2, 3, \dots)$ and Ω be an event space endowed with a probability distribution $\mathbf{P}$; a function $\mathbf{u}$ defined on $T \otimes \Omega$, i.e. $u(t, \omega)$, with $t \in T$ and $\omega \in \Omega$, is a **random function**.
It can have two interpretations.
In the first case, for each sample value ω, $u(t, \omega)$ is a function belonging to some space U. Take any set $V \subset U$ such that

$$A_V \equiv \{\omega, u(t, \omega) \in V\} \tag{1.5}$$

is an event, i.e. a set of which we know $P(A_V)$, then put

$$P_U(V) = P(A_V). \tag{1.6}$$

If we extend P_U to the (minimal) σ-algebra containing all $\{V\}$ of the form (1.5), we induce on U a probability distribution and we can view $\{u(t, \omega)\}$ as a **stochastic variable** with **values** in U.
The particular $u(t, \bar{\omega})$ for a given $\bar{\omega} \in \Omega$ is called a **realization** of the random function. This can be considered as a **sample** value in U of the random variable $\{u(t, \omega)\}$.
In the second case, we consider for each value of the parameter t the function $u(t, \omega)$ as a random variable, so that all together $\{u(t, \omega)\}$ represents a family of random variables.
When T is a finite set, we can always conventionally put

$$T \equiv \{t_1 = 1, t_2 = 2, \dots, t_N = N\} \tag{1.7}$$

and then we have a collection of N random variables $\underline{u} = [u_1, u_2, \dots, u_N]^+$ which is completely described, in a probabilistic sense, by a joint distribution function

$$P(u_1 \leq a_1, u_2 \leq a_2, \dots, u_N \leq a_N) = F_{\underline{u}}(a_1, a_2, \dots, a_N). \tag{1.8}$$

When T is infinite, we distinguish between two cases: T is **discrete** (e.g. $T \equiv 1, 2, \dots$) or **T has the power of continuum** (e.g. $T \equiv [0, 1]$ or $T \equiv \Re^n \dots$); in the former case we say that the random function is discrete, in the latter that it is continuous.
In this last case we have to identify a tool to represent the probability distribution of $\{u(t, \omega)\}$. This is usually done by specifying a sequence

of distributions, called **finite dimensional distribution** of the random function $\{u(t,\omega)\}$, defined as

$$F(t_1,\ldots,t_N;a_1,\ldots,a_N) = P\{u(t_1,\omega)\le a_1,\ldots,u(t_N,\omega)\le a_N\} \tag{1.9}$$

for $\forall N>0$ and, given N, for every N-tuple $(t_1,t_2,\ldots,t_N)$.
It is by means of a theorem by Kolmogorov, that we know when we can use a sequence

$$F_N(\underline{t}_N,\underline{a}_N) \tag{1.10}$$

where $\underline{t}_N=[t_1,t_2,\ldots,t_N]^+$ and $\underline{a}_N=[a_1,t_2,\ldots,a_N]^+$, to build a **true probability distribution** on the space of all functions defined on $T,\mathcal{F}_T$.
An example, where the full sequence of $F_N(\underline{t}_N,\underline{a}_N)$ is specified, is given by means of a so called gaussian family, i.e. a family of gaussian distributions:

$$\underline{u}_N=\begin{bmatrix}u(t_1,\omega)\\u(t_2,\omega)\\\vdots\\u(t_N,\omega)\end{bmatrix}\approx N\left[\underline{\bar{u}},C_{\underline{u},\underline{u}}\right] \tag{1.11}$$

where

$$\underline{\bar{u}}=\begin{bmatrix}\bar{\underline{u}}(t_1)\\\bar{\underline{u}}(t_1)\\\vdots\\\bar{\underline{u}}(t_N)\end{bmatrix} \tag{1.12}$$

and

$$C_{\underline{u}\underline{u}}=\begin{bmatrix}C(t_1,t_1) & C(t_1,t_2) & \cdots & C(t_1,t_N)\\ \vdots & C(t_2,t_2) & \cdots & C(t_2,t_N)\\ \vdots & \cdots & \ddots & \vdots\\ \vdots & \cdots & \cdots & C(t_N,t_N)\end{bmatrix} \tag{1.13}$$

In the above definition we must have indeed

$$\bar{u}(t)=E\{u(t,\omega)\} \tag{1.14}$$

and

$$C(t,t')=E\{[u(t,\omega)-\bar{u}(t)]\,[u(t',\omega)-\bar{u}(t')]\} \tag{1.15}$$

Since we know that the marginal distribution of a gaussian variate is again gaussian, we have only to be sure that the function $C(t,t')$ (also called the **covariance function**) used to construct the matrices (1.13) is always

symmetric and **positive definite**.
These properties are guaranteed if $C(t,t') = C(t',t)$ and for instance

$$C(t,t') = \sum_{n=1}^{+\infty} c_n \varphi_n(t)\varphi_n(t') \tag{1.16}$$

with $c_n > 0$ and $\{\varphi_n(t)\}$ any sequence of smooth functions.
In such a case in fact the quadratic form

$$\sum_{i,k=1}^{N} \lambda_i \lambda_k C(t_i,t_k) = \sum_{n=1}^{+\infty} c_n \sum_{i,k=1}^{N} \varphi_n(t_i)\varphi_n(t_k)\lambda_i\lambda_k = \sum_{n=1}^{+\infty} c_n \left[\sum_{k=1}^{N} \varphi_n(t_k)\lambda_k\right]^2 > 0 \tag{1.17}$$

is always positive definite, as it should be.
When T is all of $\Re^1$, or a subset of it, and we think of t as a "time" variable, we say that $\{u(t,\omega)\}$ is a **stochastic process**; when T is $\Re^2$ (or a subset) or a surface (e.g a sphere), we say that $\{u(t,\omega)\}$ is a **random field**(R.F.). In this dissertation we will refer to deformation and height random fields.

1.2.2 Moments

The average or first moment of the R.F. $\{u(t,\omega)\}$ is the function defined on T

$$\bar{u}(t) = E\{u(t,\omega)\} \tag{1.18}$$

The R.F. $\{u(t,\omega)\}$ is said to be centred if $\bar{u}(t) = 0$. If $\{u(t,\omega)\}$ is not centred, however, as it is obvious, the R.F. $\{u(t,\omega)\} - \bar{u}(t)$ is.
We call **simple moments** of order N of the R.F., the functions defined on T^N,

$$\overline{M}_N(t_1\, t_2\, \ldots\, t_N) = E\{u(t_1,\omega)\, u(t_2,\omega)\, \ldots u(t_N,\omega)\} \tag{1.19}$$

We call **central moments** of order N of $\{u(t,\omega)\}$ the functions

$$\overline{M}_N(t_1\, t_2\, \ldots\, t_N) = E\{[u(t_1,\omega) - \bar{u}(t_1)][u(t_2,\omega) - \bar{u}(t_2)] \ldots [u(t_N,\omega) - \bar{u}(t_N)]\} \tag{1.20}$$

Among the central moments, it is of paramount importance the central moment of order 2, also called **covariance function**

$$\begin{aligned} &C(t_1,t_2) = \overline{M}_2(t_1,t_2) = E\{[u(t_1,\omega) - \bar{u}(t_1)]\,[u(t_2,\omega) - \bar{u}(t_2)]\} = \\ &E\{u(t_1,\omega)u(t_2,\omega)\} - \bar{u}(t_1)\bar{u}(t_2) \end{aligned} \tag{1.21}$$

We note, by taking $t_1 = t_2 = t$ in (1.21), that the **variance** of the process is given by

$$\sigma^2[u(t,\omega)] = C(t,t) \tag{1.22}$$

which implies that $C(t,t)$ has to be always positive.
The notion of covariance function is so important that it raises the question on whether some given $C(t_1,t_2)$ can be considered as the covariance function of some R.F.; i.e. we want to characterize the **family of all covariance functions**.
To this aim the following lemma is providing a first idea.
$C(t_1,t_2)$ is a covariance function if and only if it is a positive definite function, i.e., given by any N-tuple $(t_1,t_2,\dots t_N)$ and $\forall N$, the matrix

$$C_N = \{C(t_i,t_k)\} \quad i,k = 1,2,\dots,N \tag{1.23}$$

is a covariance matrix (i.e. symmetric and positive definite).

1.2.3 Homogeneous and isotropic random fields

A random field is said to be **strongly homogeneous** if all shifted fields $\{v_\tau(t,\omega) = u(t+\tau,\omega)\}$ have the same probability distributions as $\{u(t,\omega)\}$ $\forall \tau \in T$.
This essentially means that $\forall N$, $\forall t_1,t_2,\dots,t_N$ the vector

$$[u(t_1+\tau,\omega)\dots u(t_N+\tau,\omega)]^+ \tag{1.24}$$

has the same distribution as the vector $[u(t_1,\omega)\dots u(t_N,\omega)]^+$, irrespectively of the value of τ. We notice that such a concept can indeed be applied only on condition that the domain T is invariant under translation, i.e., T is $\Re^1, \Re^2$, etc. A field is said to be **isotropic** when it is uniform in all orientations.
It can be useful to remark that the concept of homogeneity translates the property that, whatever window of size $L \times L$ we open on $u(t,\omega)$, we expect to find in it a statistically similar behaviour. Therefore if we take any particular function $u_0(t)$ and we ask ourselves if it can be considered as a sample drawn from a homogeneous R.F., at first we should see whether there are features in one part of $u_0(t)$ which are significantly different from those contained into another part.
Let us now turn to the characterization of the moments of a homogeneous R.F.
If $\{u(t,\omega)\}$ is homogeneous, then

$$\bar{u}(t) = E\{u(t,\omega)\} = \bar{u} \quad (constant) \tag{1.25}$$

$$C(t_1,t_2) = E\{[u(t_1,\omega)-\bar{u}][u(t_2,\omega)-\bar{u}]\} = C(t_1-t_2) \tag{1.26}$$

Taking $\tau = -t$, since $\{u(t,\omega)\}$ and $\{u(t+\tau,\omega)\} \equiv \{u(0,\omega)\}$ must have the same distribution, we immediately see that

$$E\{u(t,\omega)\} = E\{u(0,\omega)\}, \quad \forall t \tag{1.27}$$

i.e (1.25) holds true.
The vectors $[\{u(t_1,\omega)\}, \{u(t_2,\omega)\}]^+$ and $[\{u(t_1+\tau,\omega)\}, \{u(t_2+\tau,\omega)\}]^+$ must also have the same distribution, and in particular, putting $\tau = -t_1$, they must have the same distribution as $[u(0,\omega), u(t_2-t_1,\omega)]$.
Accordingly

$$\begin{array}{l} C(t_1,t_2) = E\{[u(t_1,\omega)-\bar{u}]\,[u(t_2,\omega)-\bar{u}]\} = \\ = E\{[u(0,\omega)-\bar{u}]\,[u(t_2-t_1,\omega)-\bar{u}]\} = C(t_1-t_2) \end{array} \tag{1.28}$$

which proves (1.26).
It is useful to notice that, by taking $t_2 = t_1 = t$, we can claim that

$$\sigma^2[u(t,\omega)] = E\left\{[u(t,\omega)-\bar{u}]^2\right\} = C(0) \tag{1.29}$$

which we already know since all $\{u(t,\omega)\}$ have the same distribution, $\forall t$.
A R.F. $\{u(t,\omega)\}$ is said to be **weakly homogeneous**, or homogeneous up to the **second order**, if (1.25) and (1.26) hold.
Nevertheless (1.25) and (1.26) are not enough to say that $\{u(t,\omega)\}$ is homogeneous, in fact they do not even imply that the distributions of the first and second order $F(t_1;a_1)$, $F(t_1,t_2;a_1,a_2)$ are shift-invariant.
Thus, strong homogeneity does imply weak homogeneity, while the vice-versa is not true in general.
Nevertheless, due to the particular form of their distribution functions, for **gaussian R.F.**, it is true that (1.25), (1.26) **imply strong homogeneity**.
Without entering in the details (more in Reguzzoni and Venuti [2011]), some properties about the covariance function are reported.
If $C(\tau)$ is a covariance function of a homogeneous R.F., it has to be an even function

$$C(-\tau) = C(\tau) \tag{1.30}$$

$C(\tau)$ is a covariance function (of a homogeneous R.F.) only if

$$|C(\tau)| \leq C(0) \tag{1.31}$$

In particular (1.31) shows that a covariance function is always bounded outside the origin and that it can only be unbounded if the R.F. has not a finite variance.
To be specific, in what follows, we consider random fields with finite variances everywhere, so that $C(0)$ is always finite and $C(\tau)$ is always absolutely bounded.

1.3 Wiener-Kolmogorov predictors

The following theory aims at solving the first basic problem of predicting the value of a R.F. $u(t)$ at any point t, from a set of scattered noisy data Y_i sampled from $u(t)$. It is assumed that:

1. $u(t)$ is a HIRF (Homogeneous Isotropic Random Field) on $T = \Re^1, \Re^2, \ldots$;
2. $E\{u(t)\} = 0$ on T;
3. $E\{u(t)\, u(t+\tau)\} = C(|\tau|)$ known, where τ represents the distance between the points t and $t+\tau$;
4. $Y_i = u(t_i) + \nu_i$ with $i = 1, 2, \ldots, N$ observations;
5. $E\{u(t_i)\, \nu_k\} = 0, \quad \forall i, k$;
6. ν_i is white noise that means:

$$E\{\nu_i\} = 0 \quad E\{\nu_i \nu_k\} = \sigma_\nu^2 \delta_{ik} \tag{1.32}$$

The objective is to build a predictor of the R.F. based on the observables $\{Y_i\}$ and the variance of its estimation error. Where:

- $\hat{u}(t) = G(t; Y_i, \ldots, Y_N)$ is the predictor;
- $e(t) = \hat{u}(t) - u(t)$ is the pointwise estimation error;
- $\mathcal{E}^2(G) = E\{e^2(t)\}$, is the mean square estimation error ($m.s.e.e.$).

In order to have a good predictor, it is natural to try to choose a predictor G in some class $\mathcal{G}$, in such a way that the m.s.e.e. is as small as possible; this is known as the Wiener Kolmogorov (W.K.) principle [1].
In the following W.K. principle is illustrated.
Choose the optimal predictor $\hat{u}(t) = G(t; Y_i, \ldots, Y_N)$ such that:

$$\hat{u}(t) = arg \min_{G \in \mathcal{G}} \mathcal{E}^2. \tag{1.33}$$

Written in this way the problem is purely finite dimensional and its solution depends entirely on what is assumed to be known of the composite $N+1$ dimensional R.V.

[1] Note that N. Wiener and A. Kolmogorov developed this theory in a quite independent way and along different lines of thought.

$$\underline{V} = \begin{bmatrix} u(t) \\ \underline{Y} \end{bmatrix} \tag{1.34}$$

$$\underline{Y} = \begin{bmatrix} Y_i \\ \vdots \\ Y_N \end{bmatrix} \tag{1.35}$$

If, for instance, the full probability distribution of vector $\underline{V}$ is known, a theorem of elementary probability theory can provide a quite general answer to the problem as illustrated in the following.
Define $\mathcal{G}$ as the L_Y^2 class, namely the class of those measurable functions $G(\underline{Y})$ such that:

$$E\left\{G(\underline{Y})^2\right\} < +\infty \tag{1.36}$$

then the solution of the W.K. problem is given by

$$\hat{u}(t) = E\left\{u(t)\,|\underline{Y}\right\} = u(t)\,|_Y, \tag{1.37}$$

i.e. the conditional average $u(t)$ given the observables, minimizes the m.s.e.e. In this case the corresponding m.s.e.e. is given by

$$\mathcal{E}^2 \equiv E\left\{[u(t) - u(t)]^2\,|Y\right\} \tag{1.38}$$

The proof of this theorem can be found in Papoulis [1991]; it can be noticed that in order to compute $\hat{u}(t)$, the conditional distribution of $u(t)$ given $\underline{Y}$ should be known, meaning that the distribution of the whole vector $\underline{V}$ should be known.
Nevertheless there is a notable exception for which the predictor can be computed with the information given in hypothesis 1 to 6. This is when $\underline{V}$ is a Gaussian variable; in this case it is known that the average of $\hat{u}(t)$ given $\underline{Y}$ is just a linear function of $\underline{Y}$ and a homogeneous function, since both $E\{u(t)\} = 0$ and $E\{\underline{Y}\} = 0$; as a matter of fact this means that there is a constant vector $\underline{\lambda}$ such that:

$$\hat{u}(t) = u(t)\,|_Y = \underline{\lambda}^+ \underline{Y} \tag{1.39}$$

In other words, the class of admissible estimators is limited to the class of Homogeneous Linear Functions, namely

$$\mathcal{G}_L \equiv \left\{G(\underline{Y}) = \underline{\lambda}^+ \underline{Y}, \underline{\lambda} \in \Re^N\right\} \tag{1.40}$$

The solution of the W.K. principle in the class $\mathcal{G}_L$ is given by

$$\begin{cases} \hat{u}(t) = \underline{\lambda}^+ \underline{Y} \\ C_{\underline{Y}Y} = C_{\underline{u}u(t)} \\ C_{\underline{Y}\underline{Y}} = C_{\underline{u}\underline{u}} + \sigma_\nu^2 I \end{cases} \tag{1.41}$$

where:

$$\underline{u} = \begin{bmatrix} u(t_1) \\ \vdots \\ u(t_N) \end{bmatrix} \tag{1.42}$$

$$C_{\underline{u}\underline{u}} = E\left\{\underline{u}\underline{u}^t\right\} = \begin{bmatrix} C(0) & \cdots & C(t_1 - t_N) \\ \vdots & \ddots & \vdots \\ \vdots & \cdots & C(0) \end{bmatrix} \tag{1.43}$$

$$C_{\underline{u}u(t)} = E\left\{\underline{u}u(t)\right\} = \begin{bmatrix} C(t - t_1) \\ \vdots \\ C(t - t_N) \end{bmatrix} = C^t_{u(t)\underline{u}} \tag{1.44}$$

In addition the m.s.e.e. in $\mathcal{G}_L$ (1.40) is given by:

$$\mathcal{E}^2 \equiv E\left\{\left[u(t) - \underline{\lambda}^+ \underline{Y}\right]^2\right\} = C(0) - C_{u(t)\underline{u}} C_{\underline{Y}\underline{Y}} C_{\underline{u}u(t)} \tag{1.45}$$

In the following two W.K. predictors are presented: collocation and kriging. The former assumes that the signal has a zero mean, the latter provides an unbiased estimate when the signal has an unknown constant mean.

1.4 Collocation

Assume that the observations (Y_0) are sampled from a random field and they are composed by signal (s) plus noise (ν):

$$Y_0(t_i) = s(t_i) + \nu(t_i) \quad i = 1, 2, ..., N \tag{1.46}$$

with the following stochastic features:

- $E[s(t_i)] = E[\nu(t_i)] = 0 \quad \forall t_i$
- $E[s(t_i)\, s(t_j)] = C_s(t_i, t_j) =$ signal covariance function
- $E[\nu(t_i)\, \nu(t_j)] = C_\nu(t_i, t_j) = \sigma^2_\nu \delta_{ij}$; noise covariance function, with $\delta_{ij} = \begin{cases} 1 & i = j \\ 0 & i \neq j \end{cases}$

The aim is to estimate the signal value in t_0 by using a linear combination of the available observations:

$$\hat{s}\left(t_0\right) = \sum_i \lambda_i Y_{0_i} = \underline{\lambda}^{+} \underline{Y}_0 \tag{1.47}$$

To determine the combination weights $\underline{\lambda}$, the Wiener-Kolmogorov principle is invoked:

$$E\left\{\left[s(t_0) - \hat{s}(t_0)\right]^2\right\} = \min_{\underline{\lambda}.} \tag{1.48}$$

Namely the mean square estimation error should be minimized. The result of the minimization is:

$$\hat{s}(t_0) = C^{+}_{\underline{S}S_0} \left(C_{SS} + C_{\nu\nu}\right)^{-1} \underline{Y}_0 \tag{1.49}$$

where:

$$C_{\underline{S}S_0} = \begin{bmatrix} C_S(t_1, t_0) \\ C_S(t_2, t_0) \\ \cdots \\ C_S(t_N, t_0) \end{bmatrix} \tag{1.50}$$

$$C_{SS} = \begin{bmatrix} C_S\left(t_1, t_1\right) & C_S\left(t_1, t_2\right) & \ldots & \left(t_1, t_N\right) \\ C_S\left(t_2, t_1\right) & C_S\left(t_2, t_2\right) & \ldots & \left(t_2, t_N\right) \\ \vdots & \ldots & \ddots & \vdots \\ C_S(t_N, t_1) & \ldots & \ldots & C_S(t_N, t_N) \end{bmatrix} \tag{1.51}$$

$$C_{\nu\nu} = \begin{bmatrix} \sigma_\nu^2 & 0 & 0 & 0 \\ 0 & \sigma_\nu^2 & 0 & \vdots \\ 0 & 0 & \ddots & \vdots \\ \vdots & \cdots & \cdots & \sigma_\nu^2 \end{bmatrix} = \sigma_\nu^2 I \tag{1.52}$$

with N the number of available observations.
If t_0 is an observation point the procedure is indicated as "filtering" because it permits to separate the signal from the noise; if t_0 is not an observation point it is called "prediction".
The estimation error is the difference between the true signal and the estimated signal:

$$e\left(t_0\right) = s\left(t_0\right) - \hat{s}(t_0) \tag{1.53}$$

Since the true signal is unknown, just an estimate of the error variance can be done and it is evaluated as:

$$\mathcal{E}^2\left(t_0\right) = \sigma^2\left\{e\left(t_0\right)\right\} = C_S\left(t_0, t_0\right) - C^{+}_{\underline{S}S_0} \left(C_{SS} + C_{\nu\nu}\right)^{-1} C_{\underline{S}S_0} \tag{1.54}$$

It can be said that, in general, the signal covariance matrix is a symmetric matrix as follows:

$$C_{SS} = \begin{bmatrix} C_S(t_1,t_1) & C_S(t_1,t_2) & C_S(t_1,t_3) & \vdots \\ \vdots & C_S(t_2,t_2) & C_S(t_2,t_3) & \vdots \\ \vdots & \cdots & \ddots & \vdots \\ \vdots & \cdots & \cdots & C_S(t_N,t_N) \end{bmatrix} \tag{1.55}$$

and in case data are assumed to be extracted from an homogeneous field,

- $E[s(t)] = constant$, that is verified because $E[s(t)] = 0$;
- $E[s(t_i)\, s(t_j)] = C_S(t_i,t_j) = C_S(|t_i - t_j|)$.

Finally, if the data are regularly distributed (grid points), the signal covariance matrix is a Toeplitz matrix (where Δ is the grid step).

$$C_{SS} = \begin{bmatrix} C_S(0) & C_S(\Delta) & C_S(2\Delta) \\ \vdots & C_S(0) & C_S(\Delta) \\ \vdots & \cdots & C_S(0) \end{bmatrix} \tag{1.56}$$

1.4.1 Covariance function estimation

The procedure consists into three steps:

1. *Empirical covariance function estimation* assuming that the nD random field is homogeneous and isotropic (Section 1.2.3).

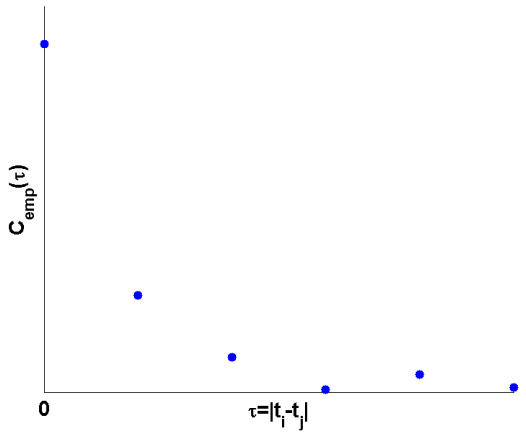

Figure 1.1: Empirical covariance.

2. *Covariance function interpolation* using a positive definite model. Possible models are, for instance:

$$C_S(\tau) = Ae^{-a|\tau|}, \quad C_S(\tau) = Ae^{-a\tau^2}, \quad C_S(\tau) = \begin{cases} A(a - |\tau|) & |\tau| \leq a \\ 0 & |\tau| > a \end{cases} \tag{1.57}$$

where A and a are parameters to be estimated.

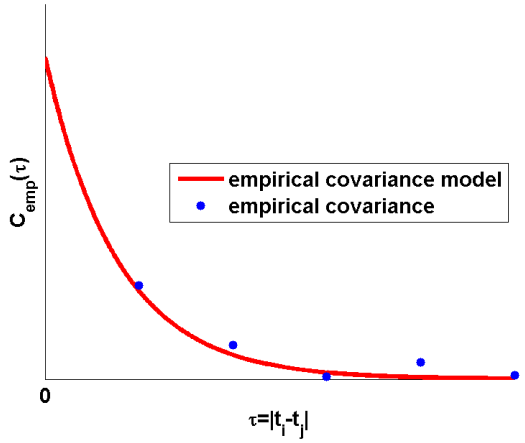

Figure 1.2: Empirical covariance and empirical covariance model.

3. *Noise variance estimation*

$$\sigma_\nu^2 = C_{emp}(0) - \hat{C}_s(0) \tag{1.58}$$

noting that the value of the empirical covariance function in the origin should not be used in the signal covariance function interpolation because it is the sum of the signal and the noise variance.

If $\hat{C}_S(0) > C_{emp}(0)$ for numerical reasons, then the variance of the noise has to be forced equal to zero or set-up to an a-priori value.

1.5 Kriging

Assume that the observations are sampled from a random field with an unknown constant mean value that is, in general, different from zero. They can be modelled as:

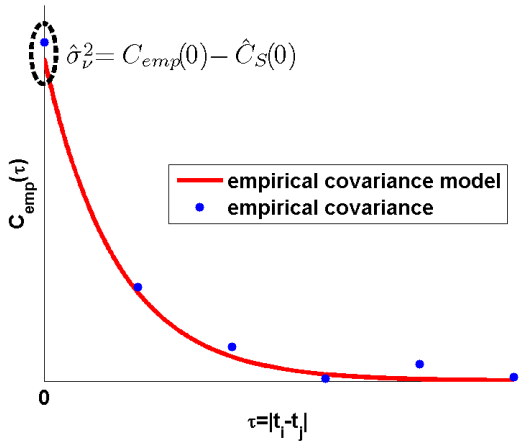

Figure 1.3: Empirical covariance and empirical covariance model; estimation of σ^2_ν.

$$Y_0(t_i) = s(t_i) + \nu(t_i) = \mu + u(t_i) + \nu(t_i) \tag{1.59}$$

where:

- $E[u(t_i)] = 0$
- $E[s(t_i)] = \mu =$ unknown mean
- $E[\nu(t_i)] = 0$
- $E[(s(t_i) - \mu)(s(t_j) - \mu)] = E[u(t_i)\, u(t_j)] = C_u(t_i, t_j) =$ signal covariance function
- $E[s(t_i)\, s(t_j)] = C_u(t_i, t_j) + \mu^2$
- $E[\nu(t_i)\, \nu(t_j)] = C_\nu(t_i, t_j) =$ noise covariance function
- $[s(t_i)\, \nu(t_j)] = E[u(t_i)\, \nu(t_j)] = 0$, meaning that the signal and the noise are uncorrelated.

Since μ is unknown, the direct estimate of the signal covariance function from the data is quite complicated; therefore the following function is defined in such a way that it does not depend on the mean value:

$$\gamma_s(t_i, t_j) = \frac{1}{2} E\left[(s(t_i) - s(t_j))^2\right] = \frac{1}{2} E\left[(u(t_i) - u(t_j))^2\right] = \gamma_u(t_i, t_j) \tag{1.60}$$

This function is called variogram. It is important to remind that $\gamma(t, t')$ is a variogram if and only if each matrix

$$\Gamma \equiv [\gamma(t_i, t_k)], \quad i, k = 1, \ldots, N \tag{1.61}$$

is conditionally definite negative, that is $\forall t_1, \ldots, t_N$, $\forall N$

$$\begin{cases} \underline{\lambda}^+ \Gamma \underline{\lambda} \leq 0 \quad \forall \underline{\lambda} \neq 0, \\ \underline{e}^+ \underline{\lambda} \equiv 0 \end{cases} \tag{1.62}$$

As for collocation, the purpose is to estimate the signal value in t_0 by using a linear combination of the available observations:

$$\hat{s}(t_0) = \sum_i \lambda_i Y_{0_i} = \underline{\lambda}^+ \underline{Y}_0 \tag{1.63}$$

and demanding that the estimate is unbiased:

$$E[\hat{s}(t_0)] = \mu \tag{1.64}$$

This condition corresponds to force that:

$$\sum_i \lambda_i = 1 \tag{1.65}$$

which is in general not satisfied in the case of collocation.
In order to determine the vector $\underline{\lambda}$ of combination weights, the following system must be solved:

$$\begin{cases} (\Gamma_{SS} - C_{\nu\nu})\, \underline{\lambda} + \alpha \underline{e} = \Gamma_{\underline{S}S_0} \\ \underline{e}^T \underline{\lambda} = 1 \end{cases} \tag{1.66}$$

where:

$$\underline{e} = \begin{bmatrix} 1 \\ 1 \\ \vdots \\ 1 \end{bmatrix} \tag{1.67}$$

$$\Gamma_{\underline{S}S_0} = \begin{bmatrix} \gamma_s(t_1, t_0) \\ \gamma_s(t_2, t_0) \\ \vdots \\ \gamma_s(t_N, t_0) \end{bmatrix} \tag{1.68}$$

$$\Gamma_{SS} = \begin{bmatrix} \gamma_S(t_1, t_1) & \gamma_S(t_1, t_2) & \ldots & \gamma_S(t_1, t_N) \\ \gamma_S(t_2, t_1) & \gamma_S(t_2, t_2) & \ldots & \gamma_S(t_2, t_N) \\ \vdots & \vdots & \ddots & \vdots \\ \gamma_S(t_N, t_1) & \gamma_S(t_N, t_2) & \cdots & \gamma_S(t_N, t_N) \end{bmatrix} \tag{1.69}$$

$$C_{\nu\nu} = \begin{bmatrix} \sigma_\nu^2 & 0 & 0 & 0 \\ 0 & \sigma_\nu^2 & 0 & \cdots \\ 0 & 0 & \ddots & \cdots \\ \vdots & \vdots & \vdots & \sigma_\nu^2 \end{bmatrix} = \sigma_\nu^2 I \tag{1.70}$$

with N the number of available observations and α the Lagrange multiplicator. The variance of the estimation error $e(t_0) = s(t_0) - \hat{s}(t_0)$ is given by:

$$\mathcal{E}^2(t_0) = \sigma^2[e(t_0)] = \alpha + \underline{\lambda}^+ \underline{\Gamma}_{SS_0} \tag{1.71}$$

It can be noticed that the variance of the estimation error of the kriging solution is always larger (or at most equal) than the corresponding variance of the collocation solution. On the other hand the unbiasness condition is not generally satisfied by collocation.

1.5.1 Variogram estimation

Like the covariance function estimation, an empirical variogram is evaluated from the data and then interpolated with a proper conditionally negative definite function.
When the field $u(t)$ is homogeneous and isotropic, there is a relation between the covariance function and the variogram:

$$\gamma_s(\tau) = C_S(0) - C_S(\tau) \tag{1.72}$$

where τ, under the hypothesis of homogeneous and isotropic field, is given by $|t_1 - t_2|$.
Figure 1.4 shows an example of variogram.
There exist also variogram models that do not have the corresponding covariance model since the class of processes $u(t)$ with homogeneous and isotropic increments is larger than that defined by homogeneous and isotropic fields. In fact, not all variograms can be derived from covariance functions by using (1.72). For example the class of variogram:

$$\gamma_s(\tau) = A|\tau|^a \quad 0 < a \leq 2 \tag{1.73}$$

does not come from a covariance family; consider for example a=1 (Figure 1.5), setting (1.72) the covariance model obtained is:

$$C_S(\tau) = C_S(0) - A|\tau| \tag{1.74}$$

that is not acceptable because the condition

$$|C_S(\tau)| < C_S(0) \quad \forall \tau \in \Re \tag{1.75}$$

is not satisfied.

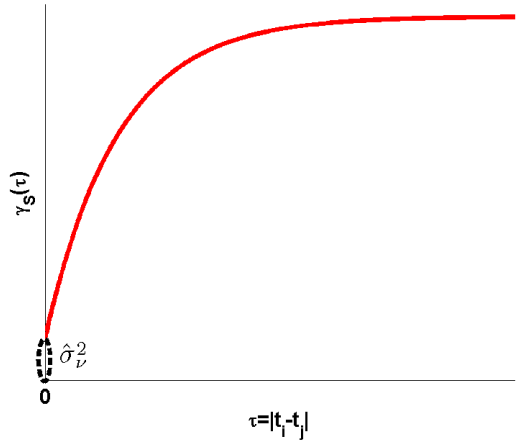

Figure 1.4: Example of variogram model.

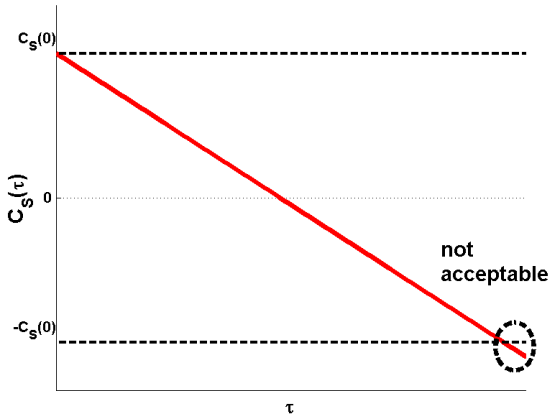

Figure 1.5: Example of a not acceptable covariance function.

Part I

Deformation fields

Chapter 2

Deformation fields: their analysis within MORFEO

This Chapter is a report of the work done by our group within the ASI MORFEO project. It consisted in the validation of EO-SAR deformation time series obtained applying two different DInSAR algorithms, SBAS developed by the IREA of Naples and SPINUA of Politecnico of Bari, to the elaboration of the same stack of SAR ENVISAT images.
Multipass Differential Interferometry Synthetic Aperture Radar (DInSAR, Section 3.2.3) is gaining a great importance in monitoring landslide events; compared with classical surveying techniques such as levelling, it provides advantages in terms of costs, coverage, data accessibility and availability of data archives. On the other hand, it is important to remind that not all the surface displacements can be detected by this technique; the following conditions have to be fulfilled:

- landslides should be located in a visible (from a radar sensor) area to avoid geometric distortions such as layover or foreshortening;
- terrain deformations should be detectable by the radar that acquires information just along the so called radar line of sight (LOS);
- displacements should be seen by the SAR system. The movement has to be slow with respect to sampling frequency, in turn depending on the satellite revisit time;
- the area of interest should contain permanent scatterers (PS), i.e. points characterized by high coherence. Urban areas are therefore more suited to be monitored by SAR techniques with respect to country ones where there are less man-made artefacts.

Since the application of DInSAR techniques to the study of slope instability is a relative new and challenging topic (Colesanti [2006]), they need to be validated on the base of more consolidate techniques.
Within MORFEO, DInSAR products obtained through the two algorithms were compared between themselves (cross-comparison) and with independent deformations obtained by GPS (validation). It has to be underlined that GPS and SAR do see different aspects of the same deformation field: they observe this field in different locations and at different times. Moreover, while SAR observes the spatial and temporal evolution of a slow-moving landslide just along its line of sight (Cascini et al. [2009], Guzzetti et al. [2009b]), GPS detects the 3D deformation vector.
The first step of the study was the choice of the test area. The landslide interesting the Ivancich quarter of Assisi, central Italy, was finally selected. This landslide is in fact slowly moving, about 1 cm/year, and involves an urbanized area. Moreover, it was monitored both by SAR and GPS already at the beginning of the project; more precisely, it was monitored by the University of Perugia through GPS annual campaigns whose data were made partially available to the MORFEO project. It is important to highlight that Ivancich GPS monitoring network was not designed according to validation purposes, that is to say, taking into account SAR PS disposal, GPS and SAR accuracies and deformation field spatial correlation. On the other hand, without historical data and a long GPS deformation series no validation could be done.
The definition of the way to compare these two kinds of observations, GPS and SAR, was the main goal of the work. Different strategies were considered before choosing the finally adopted ones, characterized by a local comparison of LOS deformation values and LOS deformation velocities.
More precisely, the deformation velocity of each GPS point was compared with the velocity of the three nearest SAR permanent scatterers. This is because, even in case the two systems observe the deformation field with comparable accuracies, the proximity between the SAR permanent scatterers and the GPS monitoring point under comparison is fundamental. The deformation field irregularity in fact makes the spatial-temporal prediction error so high to affect the result of the validation itself.
For the same reason, also the cross-comparison between SBAS and SPINUA was performed locally; in this case, the comparison between the two SAR datasets was done per areas of homogeneous deformation behaviour; more precisely, for each homogeneous area, the mean deformation velocities observed by SBAS and SPINUA were compared.
This Chapter contains a report on this validation work and it is organized as follows. Section 2.1 describes the characteristics of the Ivancich landslide used

as test area. Section 2.2 presents the two algorithms, SPINUA and SBAS, used to generate deformation time series from ENVISAT images and that had to be validated. Section 2.3 focuses on GPS: monitoring network description and data processing; it has to be specified that GPS observations resulted to be noisy and a great part of the work was dedicated to the elaboration of GNSS observations and to study the quality of the estimated coordinates. Section 2.4.1 illustrates the cross-comparison between SPINUA and SBAS data while Section 2.4.2 explains the validation procedure of SAR data using GPS. In this contest, an optimal validation procedure was developed and it is reported in Appendix A.
It should be said that this study grew up step by step, facing unexpected problems, acquiring a lot of knowledge on the critical aspect of the whole validation work. For this reason, more than a final result on GPS-SAR comparison, it is interesting to underline all those elements that have an important role in the validation process as explained in Section 2.5.

2.1 The landslide area

The landslide, considered as test area for the validation, interests a urban area of Assisi town (central Italy), whose edification started in the years 1950-1960, as a planned expansion toward East of the historical town center. It has an estimated extension of about 50 hectares, and its estimated perimeter can be seen in Figure 2.1. The area is located on a slope (average gradient 21%) where no signs of motion where noticed at the time of first edification. The urbanization of the area caused relevant changes to the flow regimen of surface waters, deviating and in some cases closing existing ditches and streams. Around 1970 the first phenomena connected with an active landslide started to show, with damages to buildings, walls and street paving. The landslide is a creep with a sliding surface located at an average depth of some tens of meters, with a maximum of about 60 meters. Even if the rate of movement is slow, the Assisi landslide has caused relevant damages to buildings, streets and infrastructures for the effect of accumulation in time (more than 50 years) of relative displacements. The damaged buildings include important complexes such as the civic Hospital and the Franciscan Cappuccini monastery. The area has been monitored since the years 1970-1980 using geotechnical techniques

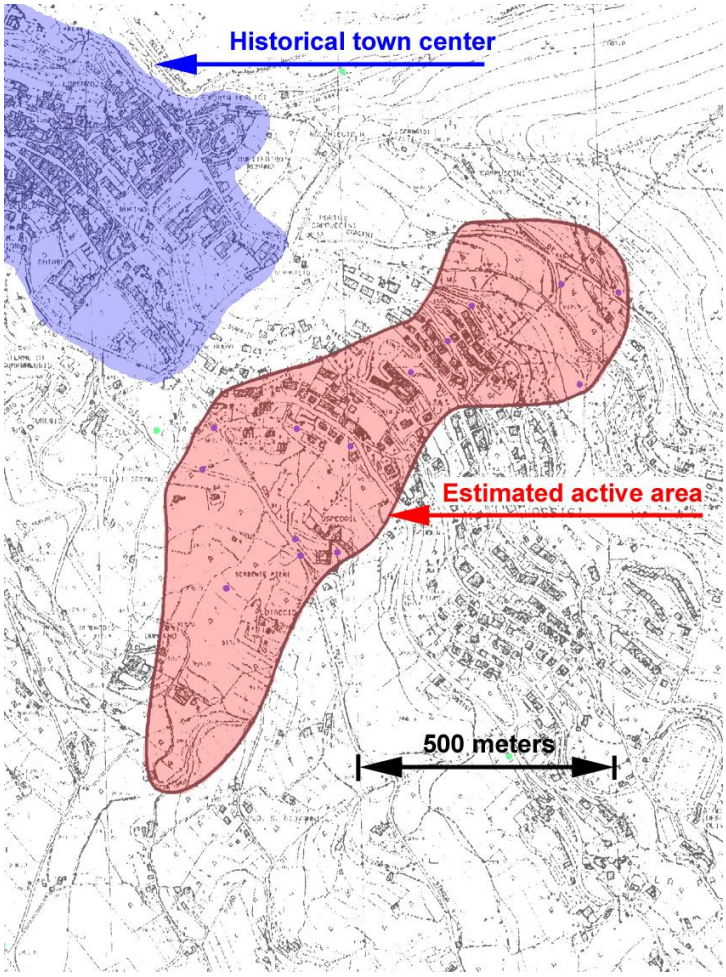

Figure 2.1: Location and estimated border of the landslide.

(drilling, inclinometers, piezometers, etc.), and by means of a conventional topographic survey (performed with total stations) of the surface movements for a number of control points. Around the end of the '80s, such measurement activity was interrupted for the excessive cost and the difficulty of terrestrial surveys in urban area. Since about 1980, some interventions have been undertaken on the landslide area by the Assisi municipality and other public subjects but most of the works realized acted on the surface waters regimen and did not interest the deep sliding surface. In the last years a more effective intervention campaign, finalized to a drainage of deep waters was started by *Provveditorato Interregionale alle Opere Pubbliche per la Toscana e l'Umbria* with funds of the Italian Government and it is still in progress. See Canuti et al. [1986] and Salvati et al. [2006] for more details about this landslide.

2.2 SBAS and SPINUA algorithms

Fundamentals about synthetic aperture radar (SAR), interferometric technique (InSAR) and differential interferometric technique (DInSAR) can be found in Section 3.2.3 and 3.2.3. In recent years several interferometric differential processing methodologies have been introduced and experimented on multi-temporal interferometric data with the aim of detecting long term deformations. In particular two strategies can be distinguished:

- the Persistent Scatter Interferometry (PSI) approach which studies the phase information over single isolated objects characterized by a high temporal phase stability. This approach is usually implemented by computing differential interferograms of all the acquisition with respect to the same reference master image, then performing advanced phase analysis on the pixels exhibiting a stable SAR response throughout the stack (Ferretti et al. [2001]);

- other methods that exploit more deeply the spatially distributed information in differential interferograms; these are obtained from pairs of images with the best value of spatial baseline. Those methods infer, with various procedure, the connected time series of phase value due to deformations (Usai [2003], Mora et al. [2003]).

In the first case, originated by PS technique, the analysis is carried out at full resolution on stable scatterers in order to separate the atmospheric, topographic and deformation components. Key assumption is the stability of the radar response, which occurs mainly in presence of dominant point scatterers. The SPINUA (Stable Point INterferometry over Un-urbanised Area) processing chain, which has been developed by the remote sensing group of Dipartimento Interateneo di Fisica - Politecnico di Bari follows mainly this PSI strategy (Bovenga et al. [2004]).
The SBAS (Small BAseline Subset) algorithm instead follows the second strategy (Berardino [2002]). Key features of the this technique are the large number of useful SAR data acquisitions, that allows an increase of the temporal sampling rate of the monitoring, and the high degree of spatial coverage over the area of interest, related to the use of small baseline interferograms only. The technique is applied pixel by pixel to all the areas exhibiting a sufficiently high coherence degree and it is robust with respect to possible errors of the DEM used in the derivation of the differential interferograms. Moreover, the availability of both time and space information permit to effectively remove the atmospheric artefacts in the results via a proper spacetime filtering operation. The scattering is supposed to be distributed within the resolution cell and

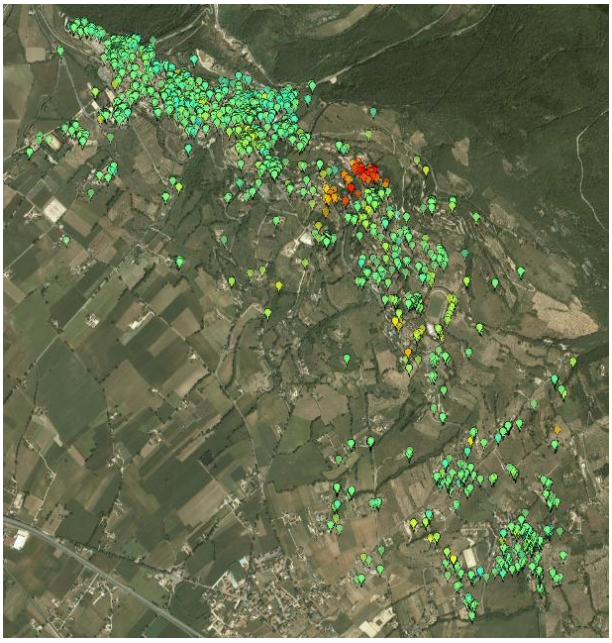

Figure 2.2: Visualization of permanent scatter position in a example map. In red those points located in the Ivancich landslide body.

spatial multilooking is implemented to enhance the phase stability. As a consequence of this operation, the spatial resolution is lower than the one obtained by the PSI approach. It this sense SBAS is particularly suitable for small scale analysis on wide areas. Nevertheless also with this algorithm it is possible to implement a subsequent large scale analysis carried out at full resolution (Berardino [2002]).
SBAS data used in this work are of this second type, that is high resolution data. It is out of this thesis to go deeply in the description of these algorithms; what is important to understand is that both the software provides coordinates and LOS deformation time series with respect to a reference time, for a set of points. Figure 2.2 illustrates the position of permanent scatterers in the area around Assisi, the point color depends on the estimated velocity of deformation; in red those points located in the Ivancich displacing zone.
DInSAR techniques observe the deformation field just along the line of sight with a frequency that depend on satellite revisit time (Figure 2.3 [1]).
In fact as explained in Section 3.2.3, DInSAR techniques exploit the concept of interference between SAR images acquired, as much as possible with the same angular view, in repeated passes of the SAR sensor over the same scene.

[1]This image has been taken from Cascini et al. [2009].

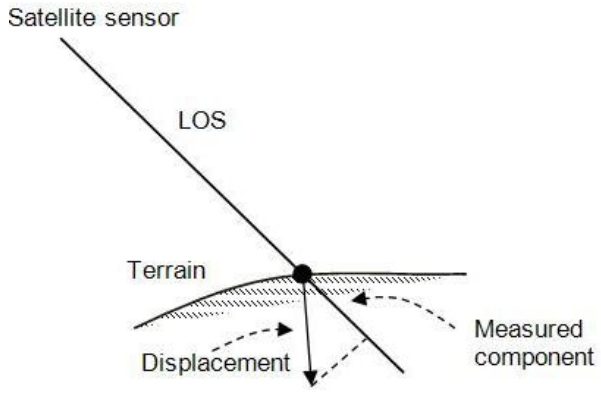

Figure 2.3: The radar geometry for displacement measurement.

The phase of each SAR image measures the distance of the target from the sensor with an accuracy of fraction of wavelength. Accordingly, the phase of the beating (interference) acquired in different times provide the measure, again with an accuracy of a fraction of wavelength, of the target displacement between the two passes along the radar line of sight. DInSAR data to be validated consist in a deformation dataset obtained by the elaboration of the same number of ENVISAT images acquired following descending orbits, the moving area remains in shadow with respect to ascending orbit, more or less with a temporal distance of about 35 days (Table 2.1 reports the date of the images used; yyyy-dd-mm stands for year-day-month). More information regarding the ENVISAT satellite can be found in ESA [2011]).

2.3 GPS data analysis

The Ivancich landslide has been monitored at first (1970 - 1980) by geotechnical techniques and by means of conventional topographic surveys (performed with total stations) of the surface movements for a number of control points. Then, since 1995, by classical plus GPS techniques (this is a well-known technology and it is not here described, see Biagi [2006] for details). The group of prof. Radicioni of University of Perugia was responsible for this monitoring (Cilli et al. [2002], Fastellini et al. [2011]). Thanks to an agreement with the *Provveditorato alle Opere Pubbliche di Firenze e Perugia*, raw data and the results of the GPS campaigns held in 2006, 2007 and 2008 by this group were made available within the MORFEO project; this permitted to make the validation of SAR products using GPS since the first year of the

Year	n	Elaborated Images (Single Look Complex)
2003	2	2003-10-10, 2003-11-14
2004	6	2004-01-23, 2004-02-27, 2004-04-02,<2004-06-09>, 2004-09-24,2004-10-29, 2004-12-03
2005	6	2005-02-11, 2005-04-22, [2005-05-27], 2005-07-01, 2005-09-09 , 2005-11-18
2006	5	2006-01-27, 2006-06-16, 2006-08-25, 2006-09-29, 2006-11-03
2007	6	2007-01-12, 2007-03-23, 2007-06-01, 2007-08-10, 2007-10-19, 2007-12-28
2008	5	2008-03-07, 2008-05-16, 2008-07-25, 2008-10-03, 2008-12-12
2009	6	2009-01-16, 2009-02-20, 2009-05-01, 2009-07-10, 2009-09-18, 2009-11-27
2010	3	2010-02-05, 2010-04-16, 2010-05-21 <2010-06-24>

Table 2.1: Date of the images elaborated with SPINUA, between [] the image elaborated with SPINUA and not with SBAS, between<> the images elaborated by SBAS and not by SPINUA.

project. The 1995 GPS network consisted in 6 reference (fiducial) points located in geologically stable sites (named from S01 to S06) and 14 monitoring points on the landslide body (named from M01 to M14) as represented in Figure 2.4. This scheme is typical of a monitoring network developed using classical instrumentation and it is not matter of discussion.
During the following years the network was enhanced and in 2006 it consisted in 28 monitoring points on the displacing area and 5 fiducial points (S04 was excluded because its marker was damaged). In 2009 and 2010 our group continued the landslide monitoring through three GPS campaigns (indicated as MORFEO campaigns in the following) on a sub-sample of the original network points (see Figure 2.5), changing the modality of data acquisition but using the same instrumentation: four receivers borrowed by University of Perugia (TOPCON receivers) plus two LEICA receivers bought with MORFEO funds. The instrumentation used consists in geodetic receivers able to acquire double frequency observations; in particular:

- TOPCON TPS E-GGD receivers with TPSLEGANT2 antennas;
- LEICA GX1230GG receivers with AX1202GG antennas;

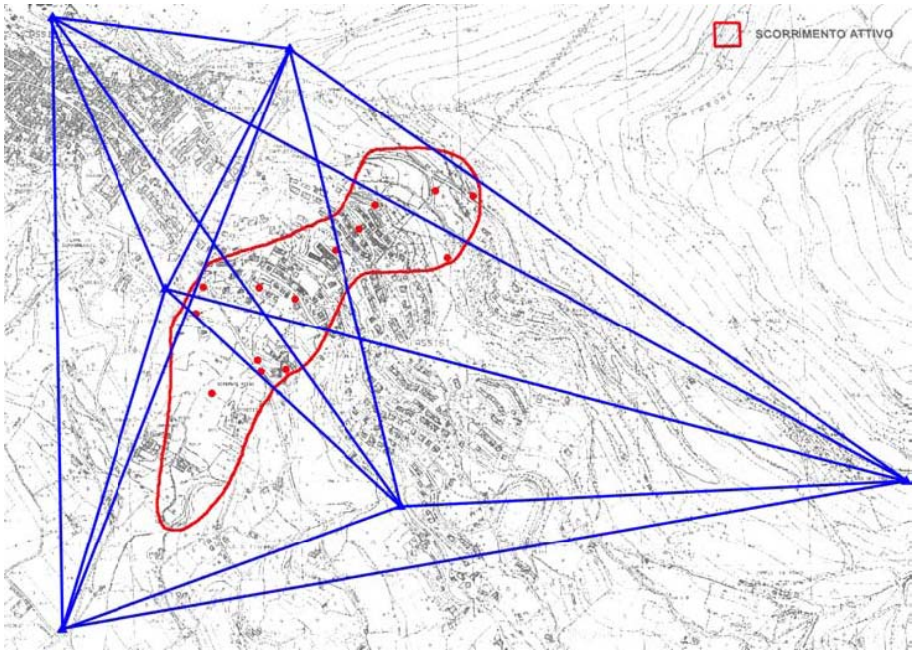

Figure 2.4: Ivancich GPS monitoring network (1995).

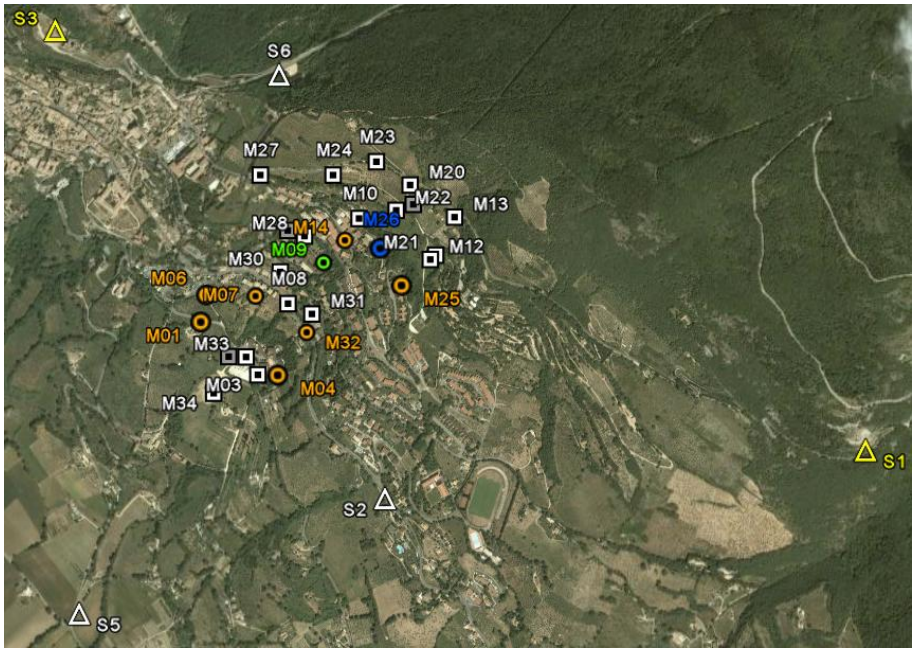

Figure 2.5: Location of GPS points monitored during MORFEO campaigns.

Figure 2.6: GPS landmark.

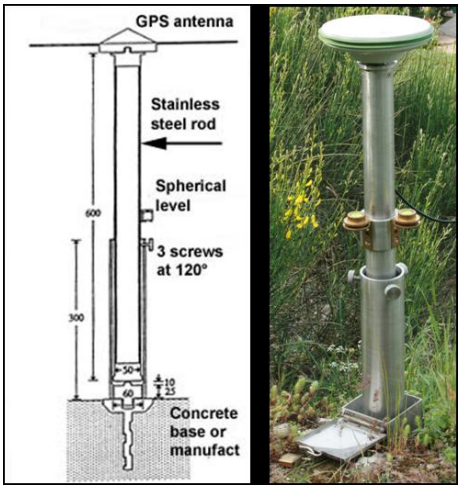

Figure 2.7: Instrumentation.

The monumentation of the vertices was realized with stainless steel centering devices mounted on concrete foundation (Figure 2.6). The GPS antenna was mounted on the fixed marker by means of removable stainless steel rod with a constant vertical offset of 60 or 90 centimetres (Figure 2.7).

In the following more details about the acquisition campaigns, GPS data treatment, obtained results and critical aspects in the use of GPS for validation will be given because they are needed to justify the accuracy of the data used in the validation. We underline again that the GPS network was not designed to validation purposes, but for the monitoring of the horizontal movement of the landslide, accurate height deformations being derived from levelling observations. Unfortunately these data were never made available to the project. Therefore, the accuracy of the monitoring points was not always sufficient for the validation purpose due to problem related to spatial location,

bad satellite visibility and multipath effects.
During the campaigns held in 2006, 2007 and 2008, framing points (S01 and S03) acquired data for all survey duration, executed in two consecutive days. Receivers located on the landslide body (indicated as M points), acquired data just for a hour session and only sometimes the survey was simultaneously done by more than one receiver. During the MORFEO campaigns the modality of acquisition for points S did not change. For the rover points M instead the survey consisted in two measurement sessions per day, held simultaneously by 4 receivers (4 points acquired data the first day and 4 the following day). Sessions lasted two hours during the 2009 campaign, three hours during that of April 2010 and two hours again in that of October 2010. From one session to the other, receivers and antennas were exchanged and the station setting remade to reduce some of the possible systematic errors. Double and independent determinations of the same coordinates in two different sessions supported an outlier rejection phase; the duration of each measurement session is reflected into the coordinate accuracy: the longer the time, the higher the accuracy. The accuracy of estimated coordinates obtainable using phase double differences in static relative positioning, as a function of measurement duration and baseline length, is shown in Table 2.2.

Distance/Time	**1 km**	**10 km**	**20 km**	**100 km**	**1000 km**
10 minutes	1.5 cm	2.5 cm	5 cm	na	na
1 hour	1.0 cm	1.5 cm	2 cm	5 cm	na
24 hours	0.3 cm	0.5 cm	$<$ cm	1 cm	1.5 cm
1 week	0.1 cm	0.1 cm	0.3 cm	0.3 cm	$<$ 1 cm

Table 2.2: Obtainable accuracies with double frequency phase observations using relative static positioning. Accuracies are function of the distance between the receivers and the measurement duration ("na" stands for not assessable) (Biagi [2006]).

As it will be explained later, long deformation time series are necessary to validate SAR deformation series; for this reason only those points surveyed also during MORFEO campaigns, held in 2009 and in 2010, could be considered for the validation; 2 points belonging to the framing network, S01 and S03, and 9 points located on the landslide body: M01, M04, M06, M07, M09, M14, M25, M26, M32 (see Figure 2.5). Figures 2.8 to 2.19 show the duration of the different measurement campaigns in different years.

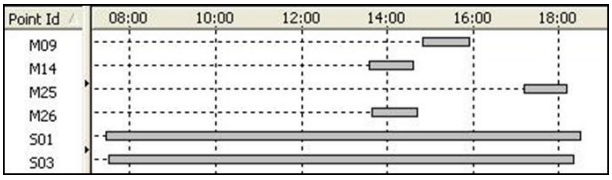

Figure 2.8: 2006 GPS campaign: GPS points surveyed during the first day of measurement (May 23^{rd} 2006).

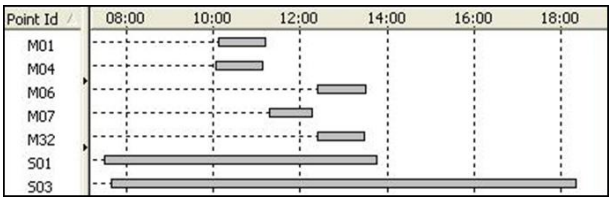

Figure 2.9: 2006 GPS campaign: GPS points surveyed during the second day of measurement (May 24^{th} 2006).

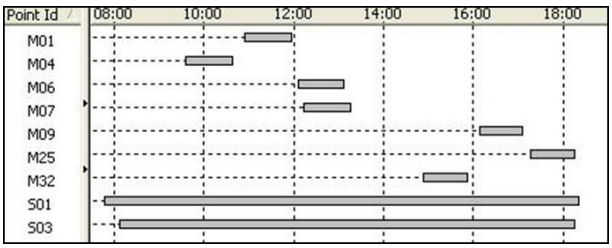

Figure 2.10: 2007 GPS campaign: GPS points surveyed during the first day of measurement (May 16^{th} 2007).

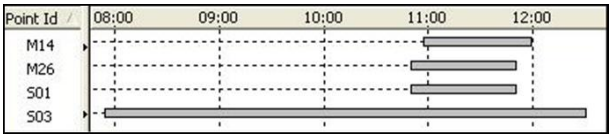

Figure 2.11: 2007 GPS campaign: GPS points surveyed during the second day of measurement (May 17^{th} 2007).

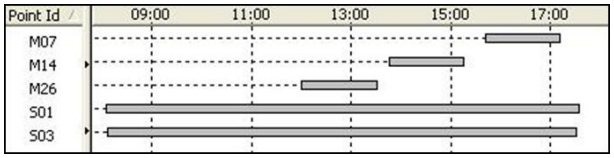

Figure 2.12: 2008 GPS campaign: GPS points surveyed during the first day of measurement (November 19^{th} 2008).

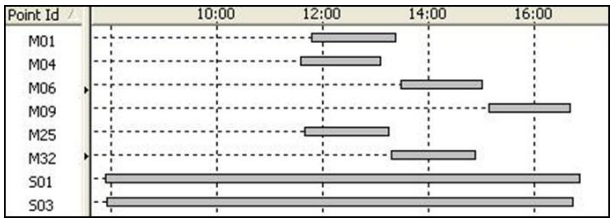

Figure 2.13: 2008 GPS campaign: GPS points surveyed during the second day of measurement (November 21^{st} 2008).

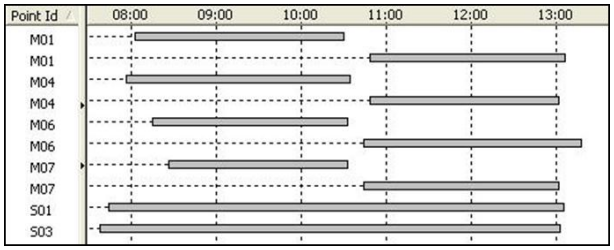

Figure 2.14: 2009 GPS campaign: GPS points surveyed during the first day of measurement (May 5^{th} 2009).

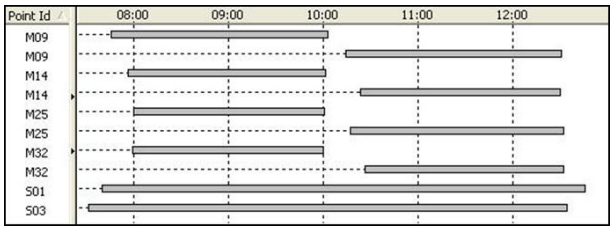

Figure 2.15: 2009 GPS campaign: GPS points surveyed during the second day of measurement (May 6^{th} 2009).

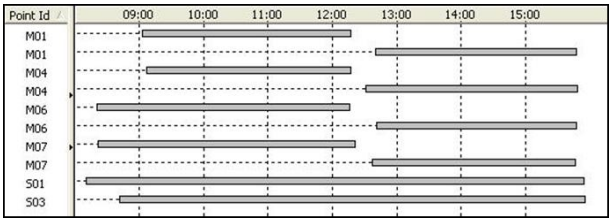

Figure 2.16: 2010 GPS campaign: GPS points surveyed during the first day of measurement (April 13^{th} 2010).

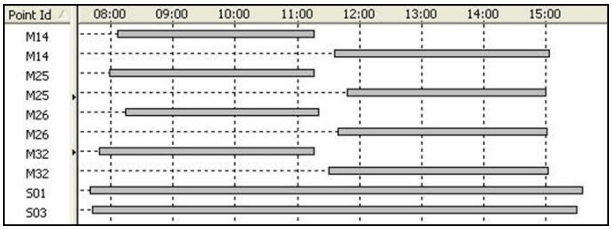

Figure 2.17: 2010 GPS campaign: GPS points surveyed during the second day of measurement (April 14^{th} 2010).

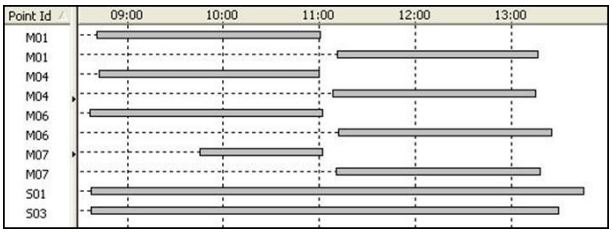

Figure 2.18: 2010 GPS autumn campaign: GPS points surveyed during the first day of measurement (October 6^{th} 2010).

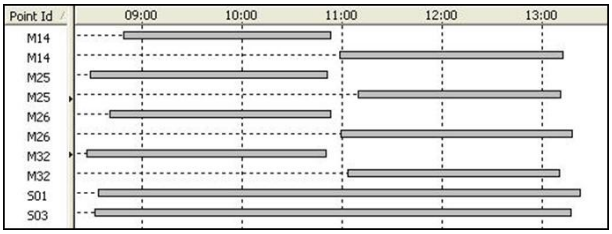

Figure 2.19: 2010 GPS autumn campaign: GPS points surveyed during the second day of measurement (October 7^{th} 2010).

2.3.1 GPS data processing

At the beginning (first year of the project) a comparison between GPS and DInSAR products was done by using the coordinates of 2006, 2007 and 2008 campaigns obtained by University of Perugia using the commercial software Geogenius developed by Spectra Precision Terrasat (Fastellini et al. [2011]). GPS information was simply a list of projected coordinates (E, N, h) for 28 GPS points located in the moving area; at that time the raw data were not available to us.
In the meanwhile the GPS observations of MORFEO campaigns were collected. They were elaborated using the commercial software Leica LGO and the scientific Bernese GPS software 5.0 of Astronomical Institute, University of Bern (Dach et al. [2007]). The new coordinates showed large discontinuities with respect to the Perugia ones, much more than the ones expected by the single landslide movement, that we addressed to the different data processing (Figure 2.20 show an example of how the estimate coordinates differ according to the used software).

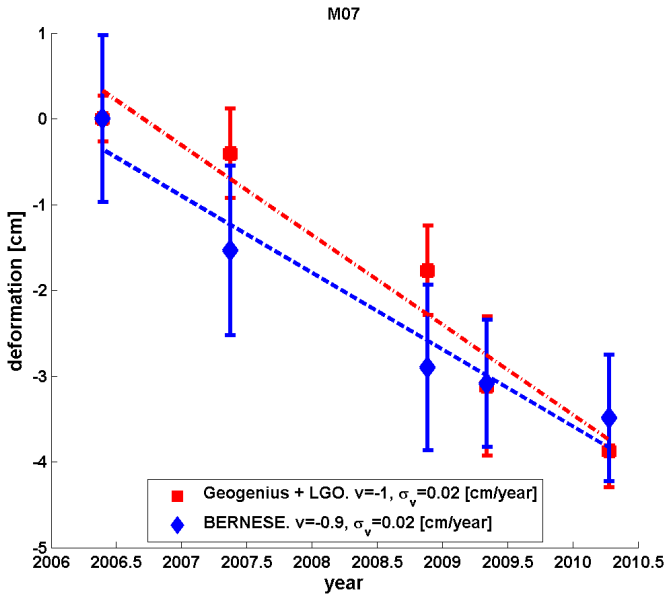

Figure 2.20: Deformation velocities estimates using different software; the example of GPS point M07.

To overcome these inconsistencies, it was decided to homogeneously ri-elaborate raw data files of the GPS campaigns held by University of Perugia

in 2006, 2007 and 2008. Data adjustment regarded just the subset of rover points surveyed also during the MORFEO campaigns.
The data processing was done firstly using the Leica LGO software just to make a first screening of data and subsequently by using Bernese software which besides a more careful and aware definition of the observations processing, allowed more affordable results. The main difference between the two software is that LGO elaborates single-base adjustment only while Bernese allows for a multi-base data adjustment, namely a least square compensation of the observations of all the stations acquiring data simultaneously. This adjustment strategy generates a better control on the quality of the observations. Compensations was done by fixing just one framing station (S01 or S03) at a time. The baseline S01-S03 was used to verify the quality of the observations of the chosen reference station. In single-base elaboration, observations of station S03 were not used to estimate the M points coordinates while in multi-base adjustment point S03 was estimated together with the other M points. Results obtained using S03 as reference point rather than S01 were used to detect possible outliers. Tropospheric effects were removed (both for the dry and the wet component) using a Saastamoinen-Niell model without any further analysis.

2.3.2 Elaboration results and outlier removal

The comparison between LGO and BERNESE estimated coordinates and between those estimated using the observations of different sessions highlightened differences not compatible with the coordinate estimated precision. An exam of the results was therefore performed to look for outliers and noisy observations. When observations have no particular problems, results are stable and don't depend on the elaboration strategy. On the contrary when observations are noisy and contain some cycle-slips, different processing strategies can bring to erroneous results, different from one software to another. When the estimated coordinates are significantly different from one session to the other, it is necessary to understand which are the problematic observations. Problems in the observations can depend on different factors, such as:

- multipath;
- satellite visibility from measuring points;
- errors in the modelling of delays in the signal propagation.

In the first case the errors depend on the acquisition period, for example from the session in the morning to the session in the afternoon; in fact multipath

effects depend on satellites position, that is on the direction of coming signals and on the electromagnetic behaviour of the area around the receiver. Since satellites configuration recurs from one day to the other with a delay of 4 minutes, multipath effects have almost the same periodical behaviour; furthermore few satellites in view with a bad distribution can reduce the positioning precision. Finally sudden variations in the water vapour content, that usually cannot be modelled a priori, cause a variation of the accuracy of the height component of all the stations.
Points affected by problems during different campaigns are probably subjected to multipath, that is by a bad environmental resonance. Once those problematic surveying points have been identified, there are different ways to detect and eliminate inaccurate observations:

- make a direct control of the quality of the observations interesting the problematic station;
- evaluate the results of adjustment made on different data sub-samples;

It can be noticed that even if adjustment software applies algorithms for automatic control and rejection of outliers, it cannot identify problems caused by the elaboration of simultaneous observations referring to more than one satellite and more than one station at a time, as it happens in the least squares adjustment. As a matter of fact, the procedure for outlier rejection based on raw observations is able to identify true outliers that are those spiky values much higher than the noise with respect to the mean. Vice versa, if in a certain time interval the noise changes a lot, also the mean value can be interested by some changes not identifiable point by point. This shifting can be identified only a posteriori, after the introduction of a deterministic model that describes the geometric congruence of observation scheme.
Another way to select bad observations is the compensation of the suspected baseline in cinematic mode; that means that the relative position of a rover point with respect to a master is estimated epoch by epoch. When an outlier or a cycle slip is present, the estimated coordinates change a lot in the different epochs.
It is important to underline that the outlier detection capability starting from adjustment results depend upon the survey scheme (this aspect was taken into account during the MORFEO campaigns). For example, sessions done in the morning and repeated in the afternoon of the same day make accidental the errors related to satellite configuration: a bad configuration in the morning can change in the afternoon and vice versa. Simultaneous sessions from different points underline problems related to particular station or to particular satellites. Long sessions permit to select just those intervals

without problems, since they last enough to estimate point coordinates with a sufficient accuracy. This analysis brought to the elimination of 4 points over the 9 considered. Data cleaning followed a conservative approach: it was decided to remove a point rather than degrade its accuracy, as this would have made the subsequent validation completely unreliable. The points considered affordable for the validation were: M01, M04, M07, M09 and M25.
The result of phase observations adjustment is the determination of GPS stations coordinates in a global cartesian reference frame, in this case the WGS84 IGS05 reference frame. It is important to notice that GPS coordinates were estimated using as reference the point S01 whose coordinates were in turn estimated using as reference point the Perugia permanent station. More precisely, the position of S01 was determined using the simultaneous observations of S01 and Perugia acquired during the campaign in 2009. The coordinates of point S01 in IGS05 used to fix the landslide monitoring network are: X=4554648.2317m, Y=1021932.8953m and Z=4333034.8895m.

2.3.3 GPS coordinates

Table 2.3 reports the estimated coordinates in WGS84-IGS05 of the points used in the validation. By comparing the results of 2006-2008 and 2009-2010 campaigns, it can been observed that the standard deviation of the last campaigns are halved with respect to the ones of the first three campaigns. This effect is linked to the session duration that changed from 1 hour in the campaigns of 2006-2007 and 2008 to 2 hours in the 2009 and 3 hours in the campaign held in April 2010 (see Figures 2.8 -2.19). It can also be underlined that the coordinate variances don't change significantly between sessions of 2 and sessions of 3 hours. This is the reason that justifies measuring sessions of 2 hours duration during the last campaign held in October 2010. The accuracy of the estimated coordinates reported in Table 2.3 was evaluated applying a calibration of the coordinates variance-covariance matrix as explained in Section 2.3.4.
From global cartesian coordinates (Table 2.3), the projected ones (E, N, h) can be computed simply applying a reference system transformation. They are reported in Table 2.4.

GPS POINT	X [m]	Y [m]	Z [m]	σ_X [mm]	σ_Y [mm]	σ_Z [mm]
2006						
M01	4554563.1820	1019749.8958	4333073.2578	5.7	4.2	5.4
M04	4554610.5765	1020011.4264	4332939.5432	6.1	4.2	5.4
M07	4554481.5745	1019909.6058	4333142.8540	7.5	4.3	5.8
M09	4554393.2091	1020111.3531	4333248.8523	6.0	4.6	6.1
M25	4554420.4888	1020373.5136	4333234.9886	7.4	4.4	8.7
2007						
M01	4554563.1711	1019749.8998	4333073.2587	6.0	5.1	5.1
M04	4554610.5577	1020011.4307	4332939.5218	6.8	4.5	5.5
M07	4554481.5682	1019909.5954	4333142.8446	8.1	4.9	6.5
M09	4554393.1990	1020111.3362	4333248.8424	5.8	3.9	6.0
M25	4554420.4711	1020373.5102	4333234.9684	7.3	4.2	6.5
2008						
M01	4554563.1606	1019749.8909	4333073.2448	6.8	4.7	6.3
M04	4554610.5668	1020011.4272	4332939.5224	7.0	4.5	6.7
M07	4554481.5660	1019909.5969	4333142.8188	5.0	3.6	4.5
M09	4554393.2252	1020111.3193	4333248.8444	7.7	4.9	6.2
M25	4554420.4683	1020373.5118	4333234.9629	6.9	4.5	6.6
2009						
M01	4554563.1637	1019749.8996	4333073.2499	2.7	2.3	2.4
M04	4554610.5597	1020011.4241	4332939.5265	2.7	2.1	2.4
M07	4554481.5662	1019909.5922	4333142.8271	3.0	2.2	2.6
M09	4554393.2240	1020111.3275	4333248.8286	2.8	2.1	2.5
M25	4554420.4747	1020373.5100	4333234.9607	2.9	2.1	2.5
Spring 2010						
M01	4554563.1718	1019749.8943	4333073.2469	2.5	2.0	2.3
M04	4554610.5784	1020011.4210	4332939.5214	3.5	2.2	2.8
M07	4554481.5881	1019909.5913	4333142.8191	2.6	2.0	2.3
M25	4554420.4881	1020373.5030	4333234.9590	2.8	2.1	2.5
Autumn 2010						
M01	4554563.1591	1019749.8846	4333073.2548	3.0	2.4	2.4
M04	4554610.5594	1020011.4189	4332939.5411	2.8	2.0	2.3
M07	4554481.5796	1019909.5593	4333142.8250	2.9	2.0	2.3
M25	4554420.4754	1020373.5091	4333234.9653	3.0	1.9	2.4

Table 2.3: GPS point estimated coordinates X, Y, Z and relative standard deviation.

GPS POINT	E [m]	N [m]	h [m]	$\sigma_{\mathbf{E}}$ [mm]	$\sigma_{\mathbf{N}}$ [mm]	$\sigma_{\mathbf{h}}$ [mm]
2006						
M01	306225.7590	4770790.4286	419.9440	4.3	4.2	6.6
M04	306465.7433	4770615.2640	404.1817	4.5	4.3	6.8
M07	306401.6785	4770866.8647	434.7822	4.7	4.4	8.2
M09	306620.7803	4770966.9098	476.3778	4.5	4.9	7.0
M25	306868.6247	4770892.4318	528.2247	4.3	4.7	10.4
2007						
M01	306225.7655	4770790.4358	419.9375	4.7	4.5	6.7
M04	306465.7515	4770615.2601	404.1543	4.6	4.4	7.4
M07	306401.6697	4770866.8638	434.7696	4.3	5.5	9.1
M09	306620.7661	4770966.9122	476.3611	3.9	4.2	7.2
M25	306868.6252	4770892.4293	528.1978	3.9	4.1	9.0
2008						
M01	306225.7591	4770790.4341	419.9191	4.5	4.7	8.1
M04	306465.7459	4770615.2551	404.1607	4.3	4.6	8.6
M07	306401.6712	4770866.8462	434.7506	3.6	3.9	5.5
M09	306620.7435	4770966.8994	476.3784	5.1	5.2	8.3
M25	306868.6273	4770892.4269	528.1923	4.3	4.7	8.4
2009						
M01	306225.7669	4770790.4343	419.9262	2.3	2.2	2.9
M04	306465.7447	4770615.2633	404.1579	2.2	2.1	2.9
M07	306401.6667	4770866.8529	434.7557	2.2	2.2	3.3
M09	306620.7514	4770966.8872	476.3681	2.1	2.1	3.1
M25	306868.6240	4770892.4214	528.1951	2.1	2.1	3.2
Spring 2010						
M01	306225.7598	4770790.4277	419.9291	1.9	2.0	2.7
M04	306465.7371	4770615.2478	404.1673	2.4	2.1	3.8
M07	306401.6605	4770866.8328	434.7657	2.0	2.0	2.8
M25	306868.6140	4770892.4125	528.2023	2.2	2.1	3.0
Autumn 2010						
M01	306225.7535	4770790.4435	419.9239	2.1	2.3	3.3
M04	306465.7400	4770615.2751	404.1668	1.9	2.2	3.0
M07	306401.6315	4770866.8484	434.7586	1.9	2.2	3.1
M25	306868.6231	4770892.4244	528.1986	2.0	2.2	3.1

Table 2.4: GPS point estimated coordinates E,N,h with relative standard deviation.

2.3.4 Covariance matrix calibration

In deformation monitoring the amplitude of the analysed phenomena is often comparable with observation errors. In the GPS case, as it is well known, the coordinates variance-covariance matrices of the observed points are under estimated; this is due to errors both in the stochastic and in the deterministic model of the least square adjustment (Teunissen [1996]). Therefore, if we want to verify whether the coordinates of a point are significantly varying in time, as it is in this validation study, we need to determine more realistic covariances. Adopting proper surveying schemes, it is possible to calibrate the covariance matrices by assuming that their shape is mainly due to the network configuration while the scale, namely the $\hat{\sigma}_0^2$, is by far too optimistic. In other words, it can be assumed that modelling errors result in an underestimation of a multiplicative factor proportional to the trace of the variance-covariance matrix itself

$$Tr(C) = \sigma_X^2 + \sigma_Y^2 + \sigma_Z^2. \tag{2.1}$$

So, the procedure consists in an "a posteriori" (based on the estimated coordinates) trace estimation to calibrate the covariance matrix C of each single GPS point obtained from the least squares adjustment; it is:

$$C_{cal} = \frac{\sigma_{X^2_{aposteriori}} + \sigma^2_{Y_{aposteriori}} + \sigma_{Z^2_{aposteriori}}}{\sigma_X^2 + \sigma_Y^2 + \sigma_Z^2} C = \frac{Trace_{aposteriori}}{Trace_C} C. \tag{2.2}$$

Obviously, to apply this procedure we need redundant estimations of the coordinates of the same point; the estimate of the calibration coefficient, in fact, becomes more robust when the number of samples used to determine it increases (Sansò [1996]). A posteriori variances of the coordinates were computed from the 2010 campaign for the 1, 2 or 3 hour sessions covariance matrix calibration. During this campaign each rover point was surveyed with two sessions of 3 hours for a total duration of 6 hours of acquisition for each point. Acquisitions were divided further on in 6 sessions of 1 hour duration each, and in 3 of 2 hours. For each point three different variances were computed considering six estimates of 1 hour, three estimates of 2 hours and then two estimates of 3 hours. The mean of the variances of 1 hour session for all the points, that of the variances of 2 hours and that at the variances of 3 hours was used to estimate the a posteriori trace of the corresponding session of 1, 2 or 3 hours duration. It is important to notice that this choice is conservative with respect to validation. In fact, an analysis of the variances before and after the calibration shows that they don't change too much from a point to another. Since it was necessary to use these variances to test

		σ^2_X [mm^2]	σ^2_Y [mm^2]	σ^2_Z [mm^2]	σ_{XY} [mm^2]	σ_{XZ} [mm^2]	σ_{YZ} [mm^2]
M01	before cal.	0.07	0.04	0.06	0.00	0.03	0.00
	after cal.	32.45	17.99	29.64	-0.52	13.38	0.75
M04	before cal.	0.08	0.04	0.06	-0.01	0.03	0.00
	after cal.	37.07	18.00	28.92	-3.19	14.02	-0.46
M07	before cal.	0.12	0.04	0.07	-0.01	0.05	-0.01
	after cal.	55.55	18.09	34.15	-4.15	24.43	-2.70
M09	before cal.	0.08	0.05	0.08	0.01	0.03	-0.01
	after cal.	35.57	20.93	36.61	2.69	13.60	-2.86
M25	before cal.	0.12	0.04	0.16	0.01	0.09	0.02
	after cal.	54.75	19.17	75.15	6.46	43.03	8.41

Table 2.5: 2006 campaign: covariance matrices of GPS estimated coordinates before and after the calibration.

the difference on coordinates estimated in two different sessions, it has been chosen to use a stable, representative and uniform value. This approach is certainly more well-grounded then the usual practise of multiplying the coordinate standard deviation for a factor 10.
Table 2.5 shows an example of the variance-covariance matrix calibration of the estimated coordinates for the year 2006.

2.3.5 Deformation projection along LOS

The displacement components in different years can be computed as the difference between the coordinates of the current year and those of a reference epoch, in this case the day 143 of 2006; covariances should be propagated correctly. Displacements are then to be projected along SAR line of sight (LOS) to compare them with corresponding DInSAR deformations; also in this case covariances should be correctly propagated. This projection is done considering the radar acquisition geometry; for example, in case of descending orbit the formula to apply is:

$$def_{LOS} = -def_E \sin(\alpha)\cos(\beta) + def_N \sin(\alpha)\sin(\beta) - def_h \cos(\alpha) \qquad (2.3)$$

where:

$$\begin{aligned} def_E &= E(t_1) - E(t_2); \\ def_N &= N(t_1) - N(t_2); \\ def_h &= h(t_1) - h(t_2). \end{aligned} \qquad (2.4)$$

with $t_1 < t_2$, α the SAR looking angle and β the angle between ground range direction and East, as shown in Figure 2.21. In this case α is 23° and β is 11.5°. It can be useful to underline that negative displacements mean that the distance SAR sensor-point (slant-range distance) is increasing, that is to say that the point on the surface is sliding down. Considering these angular values and Equation 2.3, it can be said that deformation along LOS is given by the algebraic sum of 92% of the vertical displacement, 40% of the displacement component along East and 8% of the displacement component along the North direction.

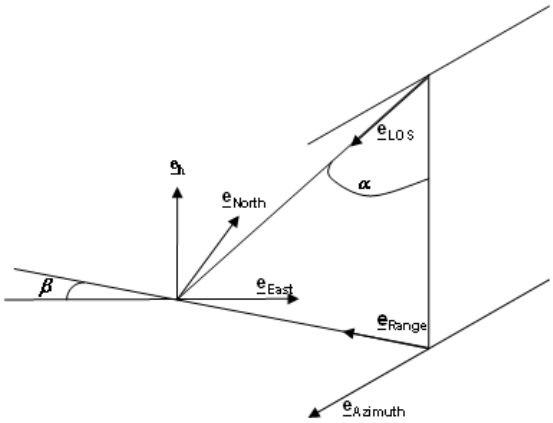

Figure 2.21: Descending imaging geometry.

An equivalent way to compute the displacement along LOS is to use cosine directors that express the LOS direction with respect to GPS global cartesian coordinate system. It can be written as:

$$def_{LOS} = def_X \, cosX + def_Y \, cosY + def_Z \, cosZ \tag{2.5}$$

where:

$$\begin{aligned} def_X &= X(t_2) - X(t_1); \\ def_X &= Y(t_2) - Y(t_1); \\ def_Z &= Z(t_2) - Z(t_1). \end{aligned} \tag{2.6}$$

with $t_1 < t_2$ and $cosX = 0.63$, $cosY = 0.52$ and $cosZ = 0.57$.
LOS deformations in different years of the points selected for the validation, with relative standard deviations (std), are reported in Table 2.6. The estimated deformation velocities of GPS points are reported in Table 2.7. Point M09 has been neglected because it was not surveyed during the campaigns held in April and October 2010 (it was inaccessible because located in a building site) and a robust estimation of the deformation velocity was not possible: its time series was not long enough.

GPS	2006		2007		2008		2009		Spring 2010		Autumn 2010	
POINT	def	$\sigma_{\mathbf{def}}$	def	$\sigma_{\mathbf{def}}$	def	$\sigma_{\mathbf{def}}$	def	$\sigma_{\mathbf{def}}$	def	$\sigma_{\mathbf{def}}$	def	$\sigma_{\mathbf{def}}$
M01	0.00	0.86	-0.41	0.92	-2.33	0.98	-1.38	0.67	-1.33	0.66	-2.18	0.70
M04	0.00	0.86	-2.18	0.91	-1.76	1.01	-2.13	0.66	-1.44	0.69	-1.58	0.67
M07	0.00	1.01	-1.49	1.15	-3.04	0.89	-2.80	0.78	-1.96	0.76	-3.85	0.78
M09	0.00	0.91	-2.10	0.93	-12.7	1.00	-1.82	0.71	-	-	-	-
M25	0.00	1.35	-24.4	1.28	-28.5	1.24	-2.67	1.00	-2.32	0.97	-2.41	1.00

Table 2.6: GPS LOS deformations and relative standard deviations. All quantities are expressed in centimeters.

GPS point	v_{GPS} [cm/y]	$\sigma_{v_{GPS}}$ [cm/y]	Is v_{GPS} significantly different from zero?
M01	-0.34	0.25	no
M04	0.27	0.13	no
M07	-0.32	0.54	no
M25	0.13	0.10	no

Table 2.7: GPS estimated velocities, v_{GPS}, and relative standard deviation $\sigma_{v_{GPS}}$.

2.4 Validation of SBAS and SPINUA deformation time series

In this Section there is a dissertation on the procedure developed to validate deformation series obtained using SBAS and SPINUA algorithms.
As said at the beginning of this Chapter, the work can be divided into two parts: the first one regards the cross-comparison between SPINUA and SBAS deformation series to see if the two algorithms agree with each other, the second one the comparison of SBAS and SPINUA separately with independent deformation series of GPS points located in the landslide area.
The former was performed per areas of supposed uniform deformation behaviour. Since there were a lot of SAR permanent scatterers in the landslide area (see Figure 2.22), the comparison was done making a test on the average deformation velocities seen by SBAS and SPINUA (taking into account all the available deformation series, 39 observations on a time span of about 7 years (Table 2.1)) and considering a uniform deformation zone at a time.
Areas of uniform deformation behaviour were selected as those areas in which most of SAR permenent scatterers, belonging to both SPINUA and SBAS datasets, observe the same land movement. It is not a rigorous and clean way to make the comparison, but in absence of other source of information, such as geological and geotechnical reports, it was not possible to select a-priori the areas with a uniform behaviour. Regarding the comparison with GPS, it was decided to compare the deformation velocity of each GPS point with the ones of the three nearest neighbours SAR permanent scatterers because the lower the distance between SAR and GPS, the higher is the probability that the observations refer to the same movement. There can be discontinuities not detectable by satellite observations only. The comparison with GPS was performed selecting a time span covered by both the observation techniques. It has to be taken into account that the irregularity of the deformation field

makes the spatial-temporal prediction error, estimated using stochastic predictors, so high to affect the results of the validation itself.
It can be underlined till now that the accuracy of GPS deformation was too low for validation purposes.

2.4.1 Comparison between SBAS and SPINUA

This section reports the work done to compare EO-SAR SBAS and SPINUA deformation time series. It was performed on a set of data obtained by the elaboration of the same number of ENVISAT descending images (Table 2.1 reports the dates of the used images as year-day-month, yyyy-dd-mm).
An horizontal rigid translation was present between deformation maps created using the two different interferometric chains related to a different reference master image (this offset is generally of the order of few meters or at maximum of few tens of meters and it has to be removed before comparing the soil displacement velocities evaluated using the two algorithms). In this particular case, the estimated translations along East and North, calculated by the Politecnico of Bari, were -34.24m E and 31.20m N to be added to SPINUA planimetric coordinates.
Figure 2.22 illustrates the location of SAR SBAS and SPINUA after this translation.
Another aspect that must be considered is that DInSAR techniques permit to obtain deformations with respect to a reference point that, for the difference in the elaboration applied, is different in the SBAS and in the SPINUA algorithm. The difference in the hooking point in general creates a constant offset between velocities and should be properly considered. In this particular situation, this offset was negligible.
The first step of the comparison procedure was the identification of the areas supposed to have an homogeneous deformation behaviour. It was decided to look for these sub-areas of deformation behaviour in areas of 100m radius around 6 GPS points (M01, M04, M07, M09, M14 and M25) plus two areas outside the landslide body, more precisely around the SBAS points 7152 and 8055 (shown in Figure 2.22).
In absence of independent information, the behaviour of each sub-area was considered homogeneous if the majority of SAR deformation velocities evaluated using the two different algorithms were similar just at a first glance.

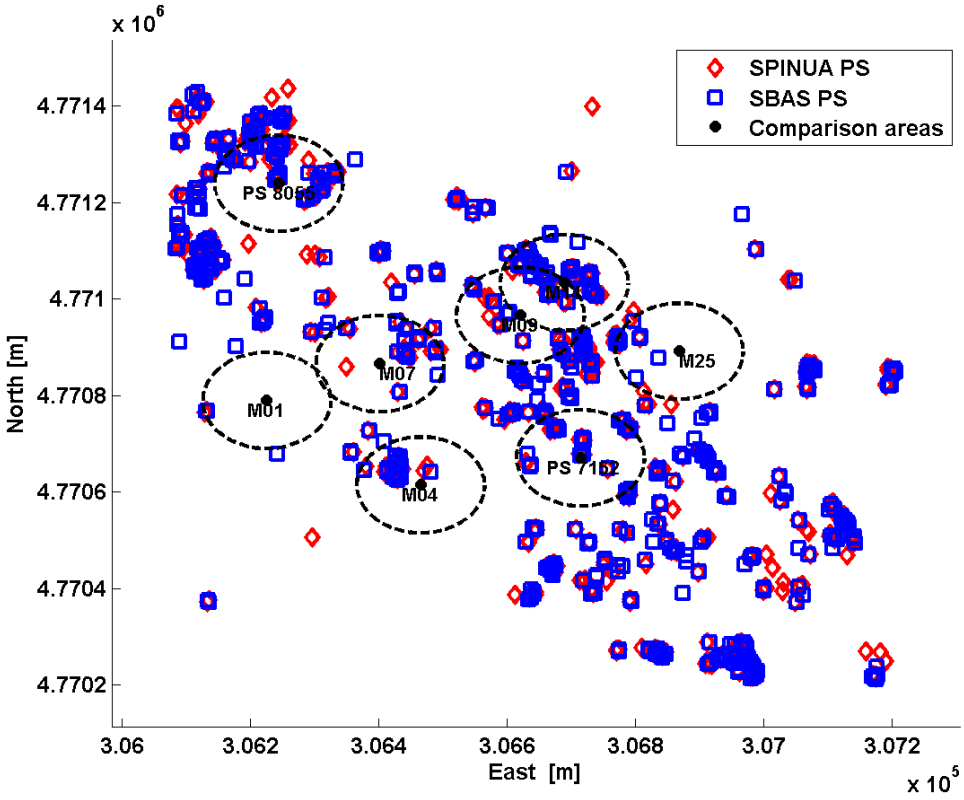

Figure 2.22: Location of SBAS and SPINUA permanent scatterers.

The following steps were:

- for each sub-area, estimate of the velocity of each single point by linearly interpolating the corresponding deformation time series. It should be noted that the assumption of linear motion, reasonable in this case by looking to the data, was an approximation that could affect the result of validation;

- evaluation of the significance associated to each estimated velocity through a standard t of Student test to verify the presence of movement. Estimated velocity was considered significant if the value t_{oss} was higher that the value t_{lim};

- for each sub-area, evaluation of the mean deformation velocities of SPINUA derived velocities and of SBAS derived velocities and corresponding standard deviations;

- evaluation of the significance of the computed mean deformation velocities;

- for each sub-area, application of a standard t of Student test (under the hypothesis of normal samples) to compare SBAS and SPINUA mean deformation velocities. More precisely, the t test was performed only after that the statistical equality of estimated velocity standard deviations was verified via a Fisher test.

As example, it is here reported the case of some areas of deformation behaviour near GPS point M07 (for more details see the report of the MORFEO project (ASI [2011])). Figure 2.23 shows the location of the areas of uniform deformation behaviour while Tables 2.8-2.11 show the estimated velocities, velocity standard deviations, empirical values $t_{oss} = \frac{\hat{v}}{\hat{\sigma}_{\hat{v}}^2}$ and theoretical values, t_{lim}, relative to a significance level of 2.5% and 38 degrees of freedom adopted to verify the significance of the estimated velocity of the selected permanent scatterers.

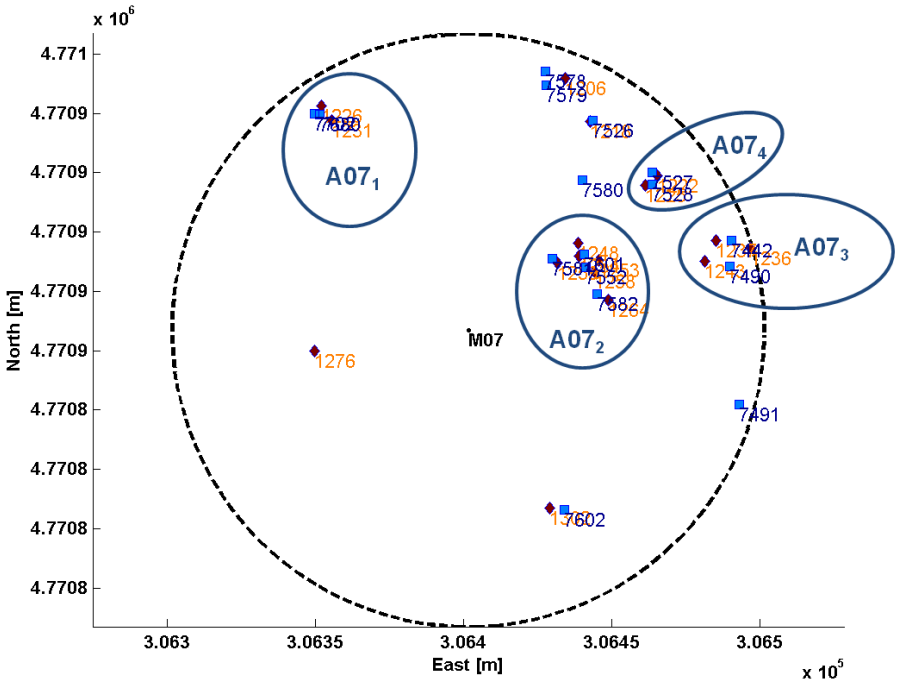

Figure 2.23: Area A07.

	SAR PS	Velocity [cm/y]	Std [cm/y]	t_{oss}	t_{lim}	Is the velocity significant?
SPINUA	1226	-0.10	0.02	-4.68	2.34	yes
	1231	-0.02	0.02	-1.28	2.34	no
SBAS	7680	-0.08	0.03	-3.23	2.34	yes
	7702	-0.10	0.04	-2.53	2.34	yes

Table 2.8: $A07_1$: t test on velocities.

	SAR PS	Velocity [cm/y]	Std [cm/y]	t_{oss}	t_{lim}	Is the velocity significant?
SPINUA	1248	-0.39	0.03	-15.08	2.34	yes
	1253	-0.38	0.02	-15.63	2.34	yes
	1254	-0.43	0.02	-17.88	2.34	yes
	1258	-0.39	0.03	-15.48	2.34	yes
	1259	-0.27	0.02	-11.91	2.34	yes
	1264	-0.39	0.02	-17.04	2.34	yes
SBAS	7552	-0.40	0.03	-11.82	2.34	yes
	7581	-0.39	0.04	-10.13	2.34	yes
	7582	-0.42	0.04	-11.69	2.34	yes
	7601	-0.43	0.04	-10.54	2.34	yes

Table 2.9: $A07_2$: t test on velocities.

	SAR PS	Velocity [cm/y]	Std [cm/y]	t_{oss}	t_{lim}	Is the velocity significant?
SPINUA	1236	-0.37	0.03	-12.83	2.34	yes
	1237	-0.39	0.03	-15.12	2.34	yes
	1243	-0.40	0.02	-19.14	2.34	yes
SBAS	7442	-0.40	0.03	-13.93	2.34	yes
	7490	-0.46	0.03	-15.23	2.34	yes

Table 2.10: $A07_3$: t test on velocities.

	SAR PS	Velocity [cm/y]	Std [cm/y]	t_{oss}	t_{lim}	Is the velocity significant?
SPINUA	1222	-0.51	0.02	-23.14	2.34	yes
	1225	-0.52	0.02	-22.65	2.34	yes
SBAS	7527	-0.54	0.03	-18.10	2.34	yes
	7528	-0.51	0.03	-17.03	2.34	yes

Table 2.11: $A07_4$: t test on velocities.

The test results are summarized in Table 2.12 and Table 2.13. For each area of homogeneous deformation behaviour, mean velocity of SBAS PSs and SPINUA PSs and their standard deviations are reported in column 2 and 3 respectively; then in column 4 is reported the result of Fisher test for the comparison of the standard deviation of the mean velocity estimated on SBAS and SPINUA points ("yes" means that they are statistically equal), column 5 contains the result of the t test for mean velocities comparison. All the test were performed with a significance value equal to 5%. In grey the areas with a movement significantly different from zero.
Tables 2.12 and 2.13 show that in all considered cases the two systems observe the same deformation velocity, both in the case it was significantly different from zero or not; more precisely, velocities become significantly different from zero when higher than 1 mm/year. Moving areas are the ones located in the center of landslide body, around GPS points M04, M07, M09, M14.

2.4.2 Validation of SAR deformation series using GPS

This validation procedure takes into account the proximity between the SAR permanent scatterers and the GPS monitoring points. The deformation field irregularity, in fact, makes the spatial-temporal prediction error too high and this can affect the result of the validation itself. On the other hand, it has to be said that, dealing with deformation fields, the proximity of points is not always synonymous of same deformation behaviour: there can be discontinuities not detectable using just satellite observations (and here the necessity of integration with external source of information regarding the landslide movement). In addition, a georeferencing error between SAR and GPS can be present.

	Dataset	$\hat{\bar{v}}$ [cm/y]	$\hat{\sigma}_{\bar{v}}$ [cm/y]	$\hat{\sigma}_{\bar{v}_{SBAS}} = \hat{\sigma}_{\bar{v}_{SPINUA}}$?	$\hat{\bar{v}}_{SBAS} = \hat{\bar{v}}_{SPINUA}$?
$A01_1$	SBAS	-0.02	0.03	yes	yes
	SPINUA	-0.02	0.03		
$A04_1$	SBAS	0.00	0.04	yes	yes
	SPINUA	-0.01	0.03		
$A04_2$	SBAS	-0.01	0.03	yes	yes
	SPINUA	-0.04	0.03		
$A07_1$	SBAS	-0.06	0.06	yes	yes
	SPINUA	-0.09	0.01		
$A07_2$	SBAS	-0.37	0.05	yes	yes
	SPINUA	-0.41	0.02		
$A07_3$	SBAS	-0.39	0.02	yes	yes
	SPINUA	-0.43	0.04		
$A07_4$	SBAS	-0.52	0.01	yes	yes
	SPINUA	-0.53	0.02		
$A09_1$	SBAS	-0.51	0.12	yes	yes
	SPINUA	-0.48	0.02		
$A09_2$	SBAS	-0.61	0.02	yes	yes
	SPINUA	-0.65	0.03		
$A09_3$	SBAS	-0.15	0.05	yes	yes
	SPINUA	-0.12	0.04		
$A14_1$	SBAS	-0.77	0.04	yes	yes
	SPINUA	-0.77	0.06		
$A14_2$	SBAS	-0.56	0.04	yes	yes
	SPINUA	-0.60	0.04		
$A14_3$	SBAS	-0.58	0.00	yes	yes
	SPINUA	-0.63	0.04		
$A14_4$	SBAS	-0.61	0.02	yes	yes
	SPINUA	-0.65	0.03		
$A14_5$	SBAS	-0.68	0.01	yes	yes
	SPINUA	-0.81	0.06		
$A25_1$	SBAS	-0.01	0.03	yes	yes
	SPINUA	-0.03	0.01		
$A25_2$	SBAS	0.00	0.00	yes	yes
	SPINUA	-0.03	0.03		

Table 2.12: Results of cross-comparison between SPINUA and SAR dataset (Table A).

	Dataset	$\hat{\bar{\mathbf{v}}}$ [cm/y]	$\hat{\sigma}_{\bar{\mathbf{v}}}$ [cm/y]	$\hat{\sigma}_{\bar{\mathbf{v}}_{\mathbf{SBAS}}} = \hat{\sigma}_{\bar{\mathbf{v}}_{\mathbf{SPINUA}}}$?	$\hat{\bar{\mathbf{v}}}_{\mathbf{SBAS}} = \hat{\bar{\mathbf{v}}}_{\mathbf{SPINUA}}$?
A7152$_1$	SBAS SPINUA	0.03 0.02	0.00 0.01	yes	yes
A7152$_2$	SBAS SPINUA	-0.05 -0.04	0.01 0.01	yes	yes
A7152$_3$	SBAS SPINUA	-0.07 -0.08	0.05 0.04	yes	yes
A7152$_4$	SBAS SPINUA	0.03 0.01	0.04 0.03	yes	yes
A7152$_5$	SBAS SPINUA	-0.01 -0.04	0.03 0.03	yes	yes
A8055$_1$	SBAS SPINUA	0.02 -0.07	0.06 0.06	yes	yes
A8055$_2$	SBAS SPINUA	0.03 0.00	0.04 0.02	yes	yes
A8055$_3$	SBAS SPINUA	-0.02 -0.04	0.04 0.03	yes	yes
A8055$_4$	SBAS SPINUA	0.00 -0.04	0.04 0.01	yes	yes

Table 2.13: Results of cross-comparison between SPINUA and SAR dataset (Table B).

The validation was performed comparing deformation velocities that:

- were computed considering deformations in an equivalent time period. To be precise, regarding SAR data, displacement velocities were estimated considering just the LOS deformations between 2007 and 2010 (a total of 19 observations), that is the period covered by the GPS observations too. All deformation were expressed with respect to an ENVISAT image acquired in the date nearest to GPS campaign held in May 2006;

- were estimated through a linear interpolation of deformation time series via least squares; in absence of a stochastic model for the deformations to be interpolated, they were considered independent of one another and with the same variance.

Practically, the validation consisted in a comparison test between deformation time series velocities; in particular, between the deformation velocities of 4 GPS points: M01, M04, M07 and M25 and that of the 3 corresponding nearest SAR points (in total 12 comparison between GPS and SBAS deformation velocities and 12 between GPS and SPINUA).
Once computed, the estimated velocities, v, and relative standard deviation, σ_v, were used to evaluate if the estimated velocities were significantly different from zero. It was done through Student tests setting the significance level $\alpha = 5\%$. Velocities, corresponding standard deviations and the results of the the comparison test between SBAS-GPS and SPINUA-GPS are reported in Table 2.14-2.17. Finally, Figures 2.24-2.27 show the deformation observed by SAR and GPS.
From the results obtained by cross-comparison (Section 2.4.1), on the basis of statistical tests on mean velocities of points located in sub-areas assumed to have an homogeneous deformation behaviour (selected, from time to time, within an area of 100 m radius around GPS point), it can be said that the areas around GPS points M01, M04 and M25 are not moving in a significant way. From the same cross-comparison, it is that 3 over 4 areas around point M07 are moving with a velocity significantly different from zero of about 0.4 and 0.5 cm/year. Considering deformation time series of those SAR points located nearest to GPS points, there are some inconsistencies with respect to the mean result. It has to be clarified that the results obtained in GPS-SAR comparison refer to different points with respect to the data used for cross-comparison (see Section 2.4.1): firstly, points belonging to the same area of 100 m radius can have a different deformation behaviour and secondly, SAR deformation velocities for GPS comparison were evaluated on a shorter time series.

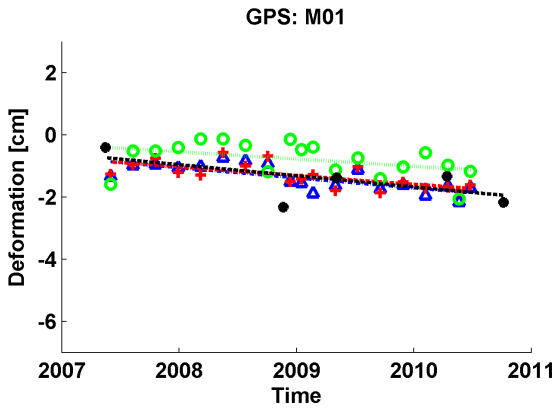

(a) SBAS

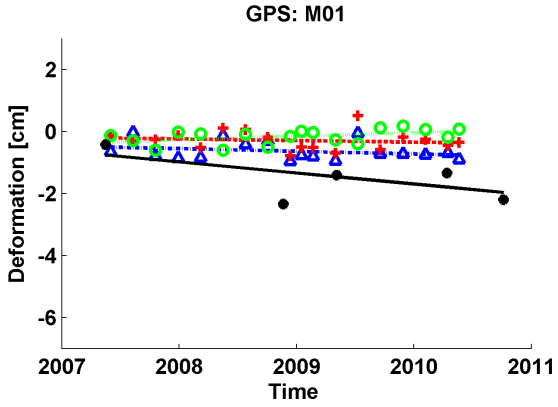

(b) SPINUA

Figure 2.24: Deformation observed by SAR PSs nearest to point M01.

SBAS PS	γ	**Dist [m]**	$\mathbf{v_{SAR}}$ **[cm/y]**	$\sigma_{\mathbf{v_{SAR}}}$ **[cm/y]**	$\mathbf{v_{SAR} \neq 0}$ **?**	$\mathbf{v_{SAR} = v_{GPS}}$ **?**
8022	0.72	95.07	-0.33	0.07	yes	yes
8045	0.72	96.18	-0.28	0.07	yes	yes
7927	0.69	112.54	-0.23	0.12	yes	yes
SPINUA PS	γ	**Dist [m]**	$\mathbf{v_{SAR}}$ **[cm/y]**	$\sigma_{\mathbf{v_{SAR}}}$ **[cm/y]**	$\mathbf{v_{SAR} \neq 0}$ **?**	$\mathbf{v_{SAR} = v_{GPS}}$ **?**
1387	0.76	97.09	-0.09	0.08	no	yes
1390	0.80	100.38	-0.05	0.08	no	yes
1276	0.82	142.27	0.12	0.06	yes	no

Table 2.14: Velocities of SBAS PSs nearest to GPS point M01.

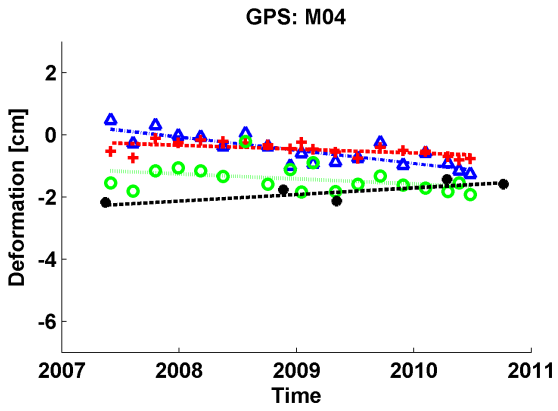

(a) SBAS

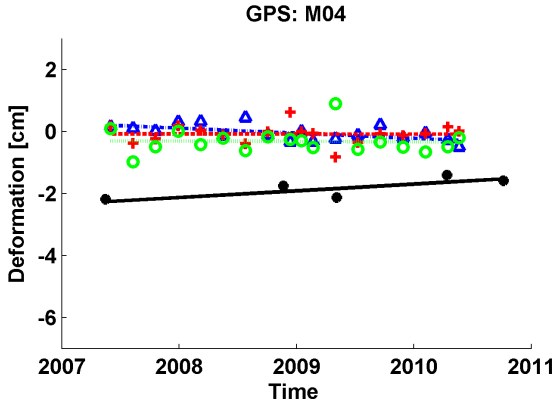

(b) SPINUA

Figure 2.25: Deformation observed by SAR PSs nearest to point M04.

SBAS PS	γ	**Dist [m]**	$\mathbf{v_{SAR}}$ **[cm/y]**	$\sigma_{\mathbf{v_{SAR}}}$ **[cm/y]**	$\mathbf{v_{SAR} \neq 0}$ **?**	$\mathbf{v_{SAR} = v_{GPS}}$ **?**
7553	0.74	29.96	-0.43	0.07	yes	no
7638	0.76	34.93	-0.13	0.05	yes	no
7639	0.72	36.80	-0.16	0.10	yes	no
SPINUA PS	γ	**Dist [m]**	$\mathbf{v_{SAR}}$ **[cm/y]**	$\sigma_{\mathbf{v_{SAR}}}$ **[cm/y]**	$\mathbf{v_{SAR} \neq 0}$ **?**	$\mathbf{v_{SAR} = v_{GPS}}$ **?**
1419	0.86	28.22	-0.16	0.06	yes	no
1434	0.81	35.59	-0.00	0.08	no	no
1438	0.81	37.97	-0.01	0.11	no	yes

Table 2.15: Velocities of SBAS PSs nearest to GPS point M04.

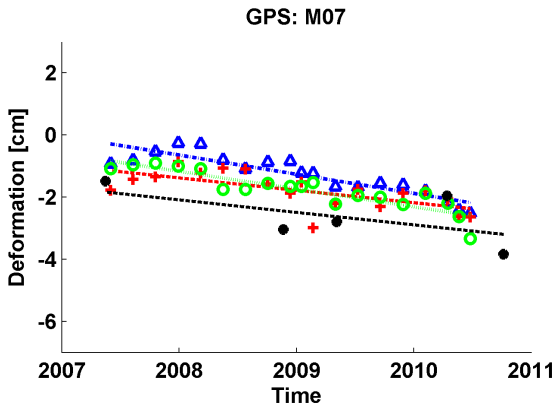

(a) SBAS

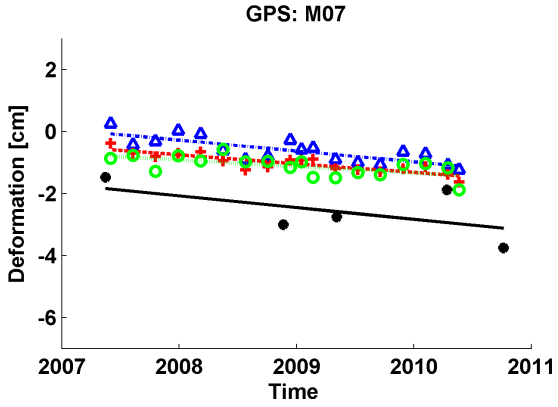

(b) SPINUA

Figure 2.26: Deformation observed by SAR PSs nearest to point M07.

SBAS PS	γ	**Dist [m]**	$\mathbf{v_{SAR}}$ **[cm/y]**	$\sigma_{\mathbf{v_{SAR}}}$ **[cm/y]**	$\mathbf{v_{SAR} \neq 0}$ **?**	$\mathbf{v_{SAR} = v_{GPS}}$ **?**
7581	0.68	37.14	-0.62	0.07	yes	yes
7552	0.74	44.91	-0.40	0.11	yes	yes
7582	0.68	45.01	-0.57	0.07	yes	yes
SPINUA PS	γ	**Dist [m]**	$\mathbf{v_{SAR}}$ **[cm/y]**	$\sigma_{\mathbf{v_{SAR}}}$ **[cm/y]**	$\mathbf{v_{SAR} \neq 0}$ **?**	$\mathbf{v_{SAR} = v_{GPS}}$ **?**
1259	0.81	37.68	-0.34	0.07	yes	yes
1254	0.83	45.12	-0.29	0.04	yes	yes
1258	0.80	47.02	-0.21	0.07	yes	yes

Table 2.16: Velocities of SBAS PSs nearest to GPS point M07.

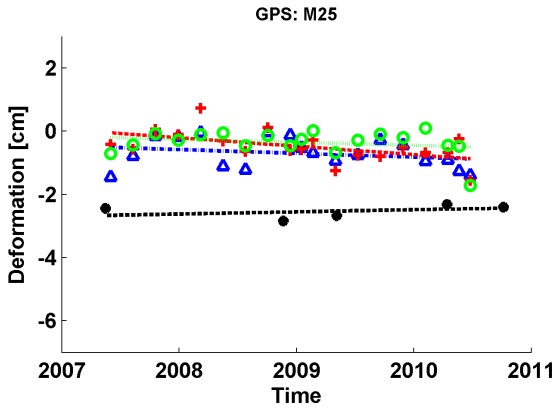

(a) SBAS

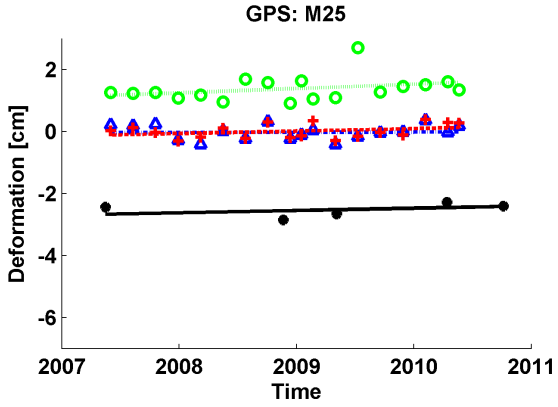

(b) SPINUA

Figure 2.27: Deformation observed by SAR PSs nearest to point M25.

SBAS PS	γ	**Dist [m]**	$\mathbf{v_{SAR}}$ **[cm/y]**	$\sigma_{\mathbf{v_{SAR}}}$ **[cm/y]**	$\mathbf{v_{SAR} \neq 0}$ **?**	$\mathbf{v_{SAR} = v_{GPS}}$ **?**
6702	0.72	35.01	-0.12	0.12	no	yes
6725	0.77	67.39	-0.27	0.11	no	no
6750	0.71	67.86	-0.10	0.10	no	yes
SPINUA PS	γ	**Dist [m]**	$\mathbf{v_{SAR}}$ **[cm/y]**	$\sigma_{\mathbf{v_{SAR}}}$ **[cm/y]**	$\mathbf{v_{SAR} \neq 0}$ **?**	$\mathbf{v_{SAR} = v_{GPS}}$ **?**
1106	0.88	67.00	0.01	0.06	no	yes
1098	0.89	68.38	0.08	0.06	no	yes
1142	0.76	94.49	0.14	0.10	no	yes

Table 2.17: Velocities of SBAS PSs nearest to GPS point M25.

As a matter of fact,for the comparison it is important that the considered SAR points are those nearest to GPS point and it is reasonable to estimate SAR deformation velocity on the same time step covered by GPS measurements. Obviously, in this way, the accuracy of deformation velocity evaluated using SAR diminishes (it is based on 19 values instead of 39) and this can transform significant velocities, estimated using smaller velocities standard deviations, in not significant velocities. Excepting point M07, that was seen in motion both from the 3 SBAS points and 3 SPINUA nearest PSs, in the other cases the results are:

- point M01: 1 velocity over 3 was significantly different for SPINUA and 2 over 3 for SBAS;
- point M04: 1 velocity over 3 was significantly different for SPINUA and 2 over 3 for SBAS;
- point M25: no point is in motion for SPINUA and 1 velocity over 3 is significant for SBAS.

These results high-lightened an intrinsic limit of the validation procedure when applied to points that don't have the same spatial position, where the deformation values change point by point on a not well determinable way. A procedure that consists in a comparison, area by area, between SAR mean deformation velocity and GPS point-wise deformation velocity would be in fact more robust if both the datasets would be located in an area with known uniform deformation behaviour. Unfortunately, in the case in exam, it was not possible to verify this condition.
Another problem found in the point-wise comparison between SAR and GPS was that the GPS deformation series were too short for validation purposes; in fact GPS deformation velocities were estimated on a limited deformation series, 5 values against 19 for SAR, and the velocity accuracy resulted to be too low.
In the present study, all 4 GPS points had a velocity not significantly different from zero (see Table 2.7). Nevertheless, the high estimated velocity variability made that, in a lot of cases, the comparison tests said that SAR and GPS see the same deformation pattern. Statistics for SPINUA reported that 9 tests over 12 are positive while for SBAS 8 tests over 12. Considering the single GPS points, for point M01 and M25 the test was positive for 5 over 6 PSs both for SPINUA and SBAS. For point M07, all PSs, both for SPINUA and SBAS, verified the equality hypothesis between SAR and GPS. Finally, for point M04, the test was overcome for 1 over 3 points for SPINUA and for none for SBAS.

Another important consideration can be done on the absolute value of the deformations seen by SAR and GPS. Even when, from the statistical point of view, SAR and GPS seemed to observe the same deformation pattern, the absolute value could be very different. Nevertheless the limited accuracy of GPS dataset made the validation procedure ineffective.

2.5 Remarks

The purpose of the comparison was to establish if terrain deformations obtained using the SBAS and the SPINUA elaboration chains were in agreement between themselves and with those got through GPS measurement surveys, done with annual frequency on a network of points, materialized on the ground, designed to monitor the landslide movement but not for validation purposes.
Regarding SPINUA and SBAS cross-comparison, statistical tests for the comparison of mean velocities in areas with homogeneous behaviour permitted to conclude that the two algorithms, when applied to the same images dataset and after the correction of the planimetric bias between points for which the movement velocity is determined, see a statistically equal deformation movement. It has to be underlined that the choice of different reference points for the two methodologies, that brings to a constant bias to velocity estimation is, in this case, not significantly different from zero.
Regarding the validation of SAR deformation series, the main result consists in the focusing of the main general limits of this comparison, such as the impossibility of making the validation due to the non sufficient accuracy of GPS measurements. Even if GPS and SAR would have the same accuracy level, it would be important that they would be near in the landslide body. This is because, since the deformation field can be very irregular (and this is frequent considering landslides, particularly when the displacement area is a strong urbanized area as Ivancich), the prediction error becomes too big and it compromises the result of the validation itself.
In these situations, a solution can be the identification of areas with homogeneous behaviour (with the help of external information sources) in which there are observations of both techniques (this is not always true but for the case of a proper location of corner-reflectors near the GPS receivers) that can be compared in term of mean velocity.
The use of velocity as the comparison term introduces the hypothesis of linear displacement and this can also be false.
Assuming that the displacement is linear with respect to time, and in the case of Assisi landslide it seems reasonable, it is important that the velocity

estimation is based on very accurate time series. In this particular case, the high variability of GPS deformations with respect to SAR ones, as the limited number of GPS points, makes the velocity estimation always significantly equal to zero and not useful for the validation.
Therefore, the MORFEO validation project revealed to be not applicable for the poor quality of GPS observations and for the GPS network disposal with respect to the SAR permanent scatterers distribution, not suitable considering the spatial coherence of the phenomena to monitor. On the other hand, the necessity to have long historical deformation series, demanded to survey the already monitored GPS network that were not designed for validation purposes.
On the base of the acquired knowledge, it can be said that to make the SAR deformation series validation using GPS, it would be necessary to:

- select GPS stations in areas with high density of permanent scatterers and recognized to be zones of homogeneous deformation behaviour; GPS permanent stations would be preferable
- where possible, locate SAR corner reflectors near GPS stations;
- make more measurement campaigns and in between each survey, make measurement sessions longer than 24 hours.

Obviously this approach would require much more time and more resources.

Nevertheless, it should be underlined the importance of validation procedures of EO products. The experience acquired in this study can be a good starting point to plan new and more effective validation procedures for future works.

Part II

Height fields

Chapter 3

Height fields and DEMs

The second part of this thesis is about the COSMO-SkyMed project activities: validation and fusion of DEMs which present different characteristics in terms of accuracy, resolution and type of information included.
In this case surface models are produced from different observations of the same height field. The validation aims at establishing if the validating model represents the same surface of a reference one, within a given range of accuracy. The fusion, when sensible, produces a unique model of the height field. Briefly, the problem is how to build a model for the Earth surface representation starting from "observations" of its height with respect to a surface chosen as reference. The kind of observations and the way to estimate a model from them result in models characterized mainly by resolution and accuracy.
All these concepts will be clarified in the present Chapter. We begin by introducing the concept of digital terrain modelling (Section 3.1) to give the background necessary to understand the work. Subsequently, in Section 3.2 the techniques used to acquire height samples are described. Since COSMO-SkyMed data products are generated from SAR data, more emphasis is given to SAR systems and interferometric/radargrammetric techniques. After that, Section 3.3 describes how to build the model from observations. Section 3.4 introduces the parameters used to describe how these models are able to represent the real surface. Finally, Section 3.5 contains a short description of DEMs available in the area of Como and used for the validation and fusion work illustrated in Chapter 4 and Chapter 5 respectively.

3.1 DEM definition

The term *Digital Terrain Model* (DTM) was defined by two engineers of the Massachusetts Institute of Technology (Miller and Laflamme [1958]) that in

the late 1950s defined a DTM as follows:
"*a DTM is simply a statistical representation of the continuous surface of the ground by a large number of selected points with known X, Y, Z coordinates in an arbitrary coordinate field*".
Since the 1960s, several other terms like Digital Elevation Model (DEM), Digital Height Model (DHM) and Digital Ground Model (DGM) have been introduced. These terms (DTM, DEM, DHM, and DTEM) are often assumed to be synonyms but sometimes they really refer to different products also in relation to the various definitions attributed to words like height, elevation and terrain. More information in El-Sheimy et al. [2005].
Generally the word DTM assumes a wider meaning, containing four groups of information:

1. landforms such as elevation, slope and other more complex geomorphological quantities;
2. terrain features, such as hydrographic features, transportation networks, etc.;
3. natural resources and environment;
4. socioeconomical data, such as population distribution, capital income, etc..

The definition of DTM may be generalized in this way (Li et al. [2005]): "*it is an ordered set of sampled data points that represent the spatial distribution of various type of information on the terrain*".
A mathematical expression to describe the model is:

$$[K_P] = [f(u_p, v_p)] \quad [K] = 1, 2, 3, ..., m \quad P = 1, 2, 3, \ldots, n \tag{3.1}$$

where K_P is one attribute value of the k-th type of terrain feature at the location of point P, (u_P, v_P) is the 2D coordinates pair of point P, m is the total number of terrain information types and n is the total number of sampled points. When m is equal to 1 and the terrain information is the height, the result is the mathematical expression of DEM which is a subset of a DTM.
In this thesis a DEM is considered as an altimetric model that consists in a set of data that allows to calculate, using an interpolating method, the height of a point of the ground with a given precision. We will consider the orthometric height of a point P, namely the length of the plumb line from P to the geoid, or the ellipsoidal height of P that is the length of the normal to a reference ellipsoid through P, from P to the ellipsoid.

An important distinction is between the terms DTM (Digital Terrain model) and DSM (Digital Surface Model). The former refers to the altitude of the bare ground while the latter includes roofs, vegetation and other manufactures as shown in Figure 3.1 [1].

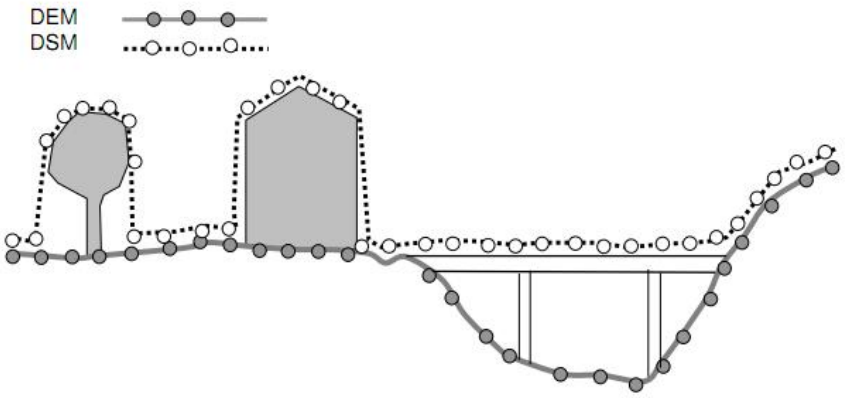

Figure 3.1: DSM vs DTM.

Altimetric models represent an alternative to the traditional use of contour lines in describing the terrain altimetry. While contour lines can overlap planimetric maps giving a very efficient representation of terrain morphology, altimetric models provide a visual description of terrain morphology only if the grid that they represent is drawn according to an axonometric projection. Therefore contour lines are used for terrain visualization while data of an altimetric model give the height information in a format uniquely suitable for numeric elaboration with a computer (Cilloccu et al. [2007]).
In fact, the most common methods to represent surface in digital forms are three:

- contour lines;
- triangulated irregular network (TIN);
- grids (Lattice or elevation matrix).

In this dissertation just DEMs in grid form are considered.
DEMs are used for different purposes ranging from basin characterization, which requires the investigation of large areas, to the evaluation of water

[1] This figure is taken from Cilloccu et al. [2007].

pounding capacity at the clod level, which requires very accurate height estimates.

The generation of a DEM can be subdivided into two steps: terrain data capture and model construction. The former regards the acquisition of terrain observations and can be done using different techniques (see Section 3.2). The latter refers to the formation of a set of relations among the different observations to build the model itself. This is created defining an interpolation method that permits to reconstruct from a dataset of sampled points a continuous model of the Earth surface (Section 3.3).

3.2 DEM generating techniques

Various techniques are used to acquire samples of the Earth surface for DEM generation, such as:

- cartographic digitization by using existing topographic maps and digitizers;
- field surveying by using total station theodolite and GPS;
- airborne laser scanning (LiDAR);
- photogrammetry by using stereo pairs of aerial and satellite images;
- radargrammetry and SAR interferometry.

Sample data accuracy depends strongly on the type of measurement performed; the technique, the instrument and the modality (static or dynamic) adopted to acquire data determine their quality.
Table 3.1 summarizes pro and cons of the different DEM acquisition methods. In terms of measurement accuracy, a millimetric level can be reached by ground survey, centimeter-level by photogrammetry and meter-level by digitization from maps. The accuracy of photogrammetric data depends on the images used. For DEM data acquisition using InSAR the accuracy is about 5 meters. In the following just the techniques adopted to generate the digital models used in this study are shortly described (for field surveying tecniques see Keim et al. [1999] and Biagi [2006]). More details are given on SAR systems and the techniques, interferometry and radargrammetry, used to generate DEMs from SAR data since they represent the way COSMO-SkyMed products are generated.

Acquisition Method	Accuracy of data	Speed	Cost	Application domain
Traditional survey	high (cm-m)	very slow	very high	small areas
GPS survey	relatively high (cm-m)	slow	relatively high	small areas
Photogrammetry	medium to high (cm-m)	fast	relatively low	medium to large areas
Space photogrammetry	low to medium (m)	very fast	low	large areas
InSAR	low (m)	very fast	low	large areas
Radargrammetry	very low (10 m)	very fast	low	large areas
LiDAR	high (cm)	fast	high	medium to large areas
Map digitization	relatively low (m)	slow	high	any area size
Map scanning	relatively low (m)	fast	low	any area size

Table 3.1: Comparison between different acquisition methods.

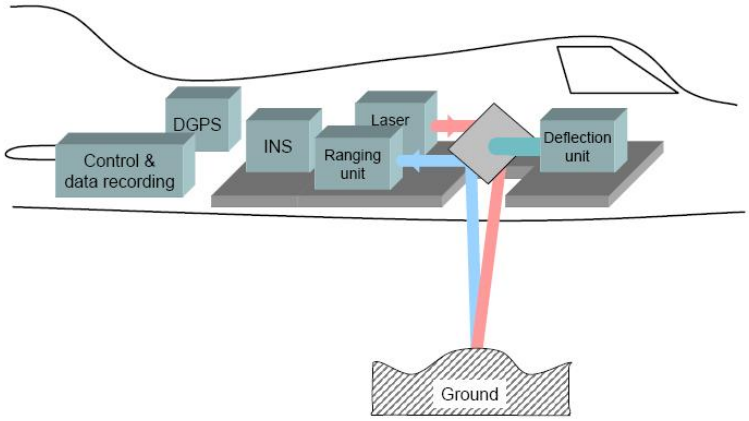

Figure 3.2: Basic components of an ALS systems.

3.2.1 Airborne laser scanning

Airborne Laser Scanner (ALS), usually called airborne LiDAR (Light Detection And Ranging) in the commercial sector, is an active remote sensor that sends off electromagnetic energy, with wavelengths ranging from 1040 to 1060 nm, and records the energy scattered back from the terrain surface and the objects on it; the recorded signal is immediately converted to a digital representation and stored directly onto a computer. The type of surface hit by the pulses determines the intensity of returned signals.
It is a complex system as shown in Figure 3.2[2] that consists of three technologies: LASER, inertial navigation system (INS) and GPS.
Details on laser scanning can be found in Wehr and Lohr [1999]; here it is shown the basic relations of airborne laser scanner and the factors influencing the accuracy of the 3D coordinates of the point measured with it (Baltsavias [1999]).
For a pulse laser, the range (R) and the range resolution (ΔR) can be defined as:

$$\begin{aligned} R &= \frac{c \cdot t}{2} \\ \Delta R &= \frac{c \cdot \Delta t}{2} \end{aligned} \tag{3.2}$$

where t is the time interval between sending and receiving a pulse, c is the speed of light ($\approx 300,000\ km/s$) and Δt is the resolution of time measurement.
For a continuous wave (CW) laser, instead, they can be evaluated as:

[2]This figure has been taken from Brenner [2006].

$$R = \frac{1}{4\pi}\frac{c}{f}\varphi$$
$$\Delta R = \frac{1}{4\pi}\frac{c}{f}\Delta\varphi \tag{3.3}$$

where f is the frequency (Hz); φ is the phase (rad); and $\Delta\varphi$ is the phase resolution (rad).
The accuracy of laser ranging is defined as

$$\sigma_R \sim \frac{1}{\sqrt{S/N}} \tag{3.4}$$

where σ_R is the ranging precision (m) and S/N is the signal to noise ratio.

The error sources in the derived coordinates can be listed as:

- errors in the direct georeferencing parameters detection provided by GPS-IMU units;
- errors in the measured laser range;
- errors in the spatial rotational offsets between the various reference systems;
- errors in the measured orientation angles relating laser beam and laser-unit coordinate system.

The ALS system produces data that can be characterized as sub-randomly distributed 3D points cloud whose distribution depends on the scanning pattern of the laser scanner system.
Since the results are usually given in WGS84, the final results also depend on the accuracy of the transformation from WGS84 to the local coordinate system, including correction for the geoid undulations, which can be significant with respect to the potential accuracy of ALS.
Furthermore, a data processing is needed both to remove outliers and to model data of a given specific model (e.g., a DTM) as a subset of a measured digital surface model (DSM). This processing consists in filtering, classification and modelling. Filtering refers to the separation of those measurements which derive from ground surface reflection from those which derive from vegetation and buildings. Classification means to find a specific geometry or statistic structure of the data. Modelling refers to the identification of the Earth surface data and manufactures like buildings. It is important to highlight that the quality of DTMs or DSMs is very dependent, besides the overall measurements density and the accuracy of the laser scanner system, on

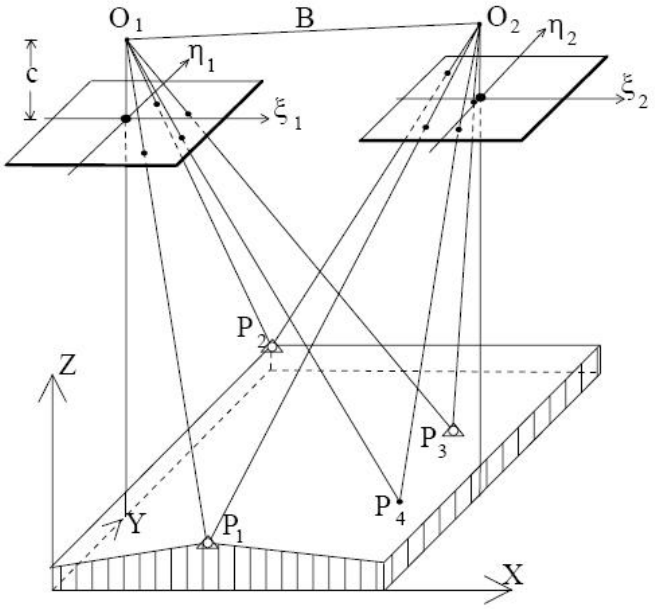

Figure 3.3: Stereo model.

the post-processing software used to implement filtering and interpolation algorithms. As a rule of thumb, being the flying height of most existing ALS systems in the range of 20 to 6000 m (typically 200 to 300 m), the height accuracy can be considered in the range of 10 to 60 cm (typically 15 to 20 cm) while planimetric accuracy between 0.1 and 3 m (typically 0.3 to 1 m).

3.2.2 Photogrammetry

Photogrammetry makes use of a pair of stereo images to reconstruct the original shape of 3D objects, that is, to form the stereo-model (Figure 3.3). The problem consists in determining the coordinates of a point in a ground reference system, measuring the coordinates of the same point in the image reference system of each photograph.
The relation between an image point coordinates, the corresponding ground point and the projection center (camera) coordinates is given by the collinearity equations which assume these three points standing on a straight line.
If the orientation parameters of each photograph (3 rotations and 3 translations) are known and the image coordinates of P in the two images have been measured, by means of the collinearity equations, it is possible to calculate the ground coordinates X_P, Y_P, Z_P of the point P.

The images of the same point P in two photos are called homologous points. In analytical photogrammetry, the search of homologous points is carried out by an operator, while in digital photogrammetry this search is done automatically by a procedure called *image matching*. Photogrammetric techniques can be applied both on aerial and space images. Error sources in derived object points from photogrammetric techniques include:

- errors in the internal characteristics of the implemented imaging system as principal distance, principal point coordinates, etc.;
- errors in the external characteristics of implemented imaging system; they are errors in the estimation of the position and the orientation of the imaging system that can be done directly with a GPS-IMU instrument or indirectly using the collinearity equations on points of known coordinates, called control points;
- errors associated with the image coordinate measurements of conjugate points in overlapping stereo-images;
- errors in the utilized mathematical model to link image coordinates and ground coordinates.

Much more information can be found in Kraus [1992].

A sensor used to acquire satellite images to use as stereo-pairs is ASTER and it is described a little bit in detail in Section 3.5.3.

3.2.3 Radargrammetry and SAR interferometry

Radargrammetry and SAR interferometry are two techniques that allow to produce DEMs from SAR images: the former through the measurement of parallax while the latter through the determination of phase shifts between two echoes. Before describing these techniques, the SAR system is introduced.

SAR

SAR stands for Synthetic Aperture Radar; it is an active system that works with microwaves. It is not dependent on sunlight and allows continuous day/night operation.
Figure 3.4 shows the geometry of the radar imaging.
The radar is on-board a flying platform that can be an air-plane or a satellite. It transmits a cone-shaped microwave beam (1 to 1000 GHz) to the ground with a side-looking angle θ_0 in the direction perpendicular to the flying track.

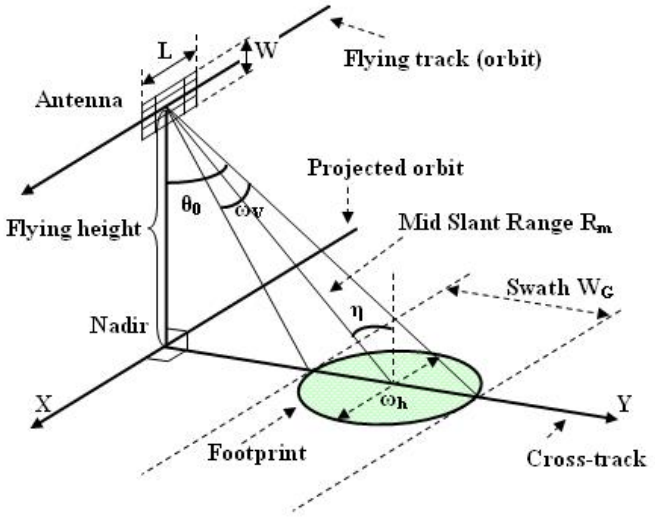

Figure 3.4: Radar imaging geometry.

Each time, the energy sent by imaging radar forms a radar footprint on the ground. This area may be regarded as consisting of many small cells. The echo backscattered from each ground cell within the footprint is received and recorded as a pixel in the image plane according to the slant range between the antenna and the ground cell.
The raw direction of a SAR image, called azimuth, is defined by the trajectory of the platform that carries the antenna, while the column direction, named slant range, is defined by the radar beam direction, usually perpendicular to the platform trajectory. The echo time-delay is:

$$t = \frac{2R}{c} \tag{3.5}$$

where R is the radar-target distance.
The echo amplitude is related to the terrain backscattering properties which depend on several physical parameters of the terrain such as the dielectric constant (permittivity), the surface roughness and the local slope. Each echo contains also a phase information that is related to the average propagation time of the radar wave, on the nature of the elementary scatterers contained in the pixel footprint and on their geometric distribution.
After a quite complex processing, each pixel of a SAR image contains the amplitude of the received wave and the phase value related to the radar slant range (Figure 3.5 shows an example of amplitude image while Figure 3.6 represents a phase image acquired by an hypothetical SAR sensor flying at a

high of 780 Km over the Earth and with a normal baseline of 100 m [3]).

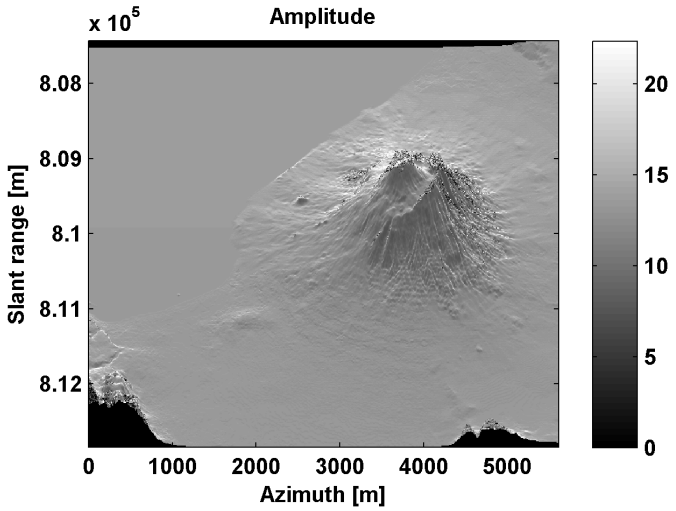

Figure 3.5: Example of amplitude image (Vesuvio volcano, Southern Italy).

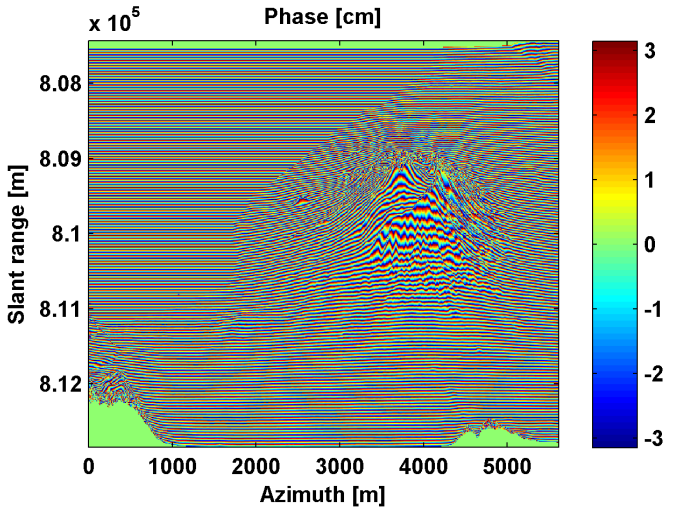

Figure 3.6: Example of phase image (Vesuvio volcano, Southern Italy).

These two components are recordable as a complex number and the SAR image can also be called a radar complex image.

[3]These images have been taken from the "SAR imaging" course held at Politecnico di Milano - Polo Territoriale di Como (Monti Guarnieri [2011]).

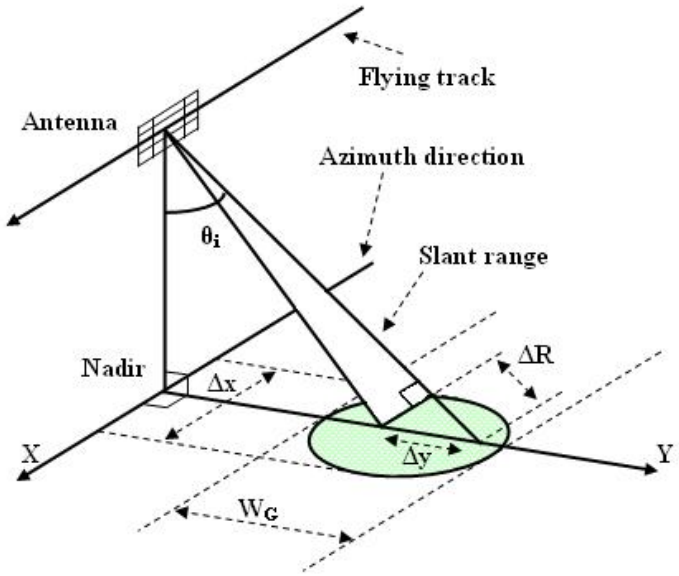

Figure 3.7: Resolution of radar imaging.

The quality of a SAR image is related to its spatial resolution, i.e. to the capability of resolving separate terrain elements on the Earth's surface. It is defined by the azimuth, the slant-range and the ground-range resolution. According to electromagnetic wave theory, the azimuth resolution (Δx) can be computed as:

$$\Delta x = \frac{R\lambda}{L} \tag{3.6}$$

where R is the slant-range, λ is the wavelength of the microwave, L is the length of the aperture of radar antenna and Δx is the width of the footprint as shown in Figure 3.7.
The slant-range resolution (ΔR) is:

$$\Delta R = \frac{c\tau_p}{2} \tag{3.7}$$

while the ground-range resolution (Δy)

$$\Delta y = \frac{\Delta R}{\sin\theta_i} = \frac{c\tau_p}{2\sin\theta_i} \tag{3.8}$$

where c is the speed of light, τ_p the pulse duration and θ_i is the side-looking angle. Equations 3.6 and 3.8 show that slant range resolution depends only on the property of the microwave and on the looking angle while the

azimuth resolution is mainly determined by the position and by the size of the antenna. The longer the antenna length, the better the azimuth resolution. For space-borne systems, the slant range distance being of several hundreds of kilometres, an acceptable resolution (e.g. 10 m) requires an antenna length of many kilometres that is impossible to realise. To overcome this problem the synthetic aperture radar has been invented. It is based on the principle of the Doppler frequency shift caused by the relative movement between the antenna and the target.
In this way the azimuth resolution (Δx) of the SAR is improved to the value:

$$\Delta x = \frac{L}{2}. \tag{3.9}$$

Principle of Radargrammetry

Radargrammetry is similar to photogrammetry (Section 3.2.2). In this case the stereo model is formed by two SAR images acquired from the same side but with different incidence angles; differently from SAR interferometry, which exploits the information given by the phase, radargrammetry uses only the amplitude information of SAR images. It can be implemented using an interactive approach or an automated one.
The radargrammetric approach was first used in the 1950s; then it was less and less used, due to the quite low resolution of radar imagery in amplitude, if compared to their high resolution in phase. In the last decade the availability of very high resolution data has transformed the radargrammetric approach in a valid alternative to generate DSMs from SAR data (Raggam et al. [2010] and Toutin and Chénier [2009]). In particular this method can be used to fill gaps due to the lack of coherence in interferometric DSM in order to obtain the best product (Crosetto and Pérez Aragues [2000]).
The 3D reconstruction relies on the following issues:

1. determining the sensor-object stereo model;

2. searching for homologous pixels using image matching techniques;

3. determining 3D coordinates by solving an intersection problem.

In order to establish the correspondence between the image and the object space, a rigorous SAR image formation model (SIFM) must be defined.
It is based on two basic SAR mapping equations, namely the range and the Doppler equations:

$$R_S = \left| \left(\overrightarrow{P} - \overrightarrow{S} \right) \right| = SP \tag{3.10}$$

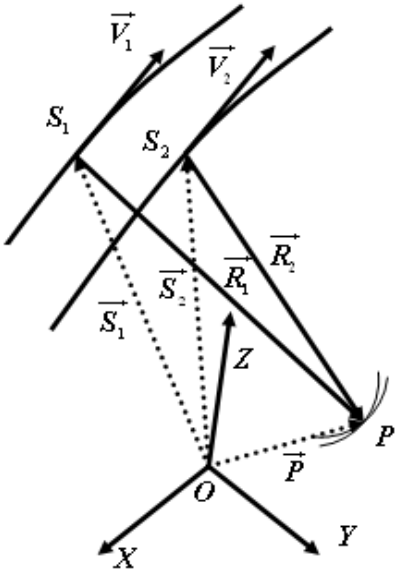

Figure 3.8: Stereo configuration of radargrammetry.

$$f_D = -\frac{2 \cdot \overrightarrow{SP} \cdot \overrightarrow{V}_S}{\lambda \cdot SP} \tag{3.11}$$

where $\overrightarrow{P} = (X_P, Y_P, Z_P)$ is the location of the target point on the ground, $\overrightarrow{S} = (X_S, Y_S, Z_S)$ the satellite position, $\overrightarrow{V_S}$ the satellite velocity vector, R_S the slant range distance, f_D the Doppler centroid frequency and λ the radar wavelength. The SIFM includes different groups of parameters: orbital parameters, sensor parameters and SAR processing parameter. Furthermore, the model parameters are often known with inadequate accuracy and should be refined using a calibration procedure based on the measurements of tie points and ground control points. For more details see Crosetto and Pérez Aragues [2000].

Figure 3.8 shows the general stereo configuration of radargrammetry, in which two SAR images are acquired with different radar look angles along two different flight paths.

There is a plane formed by the two-sensor positions $(\overrightarrow{S_1}, \overrightarrow{S_2})$ and the object position $(\overrightarrow{P})$. This implies that the object position is determined by the intersection of two radar rays with different look angles, leading to a complanarity

condition expressed as follows:

$$\overrightarrow{S_1} + \overrightarrow{R_1} - \overrightarrow{S_2} - \overrightarrow{R_2} = 0 \tag{3.12}$$

where $\overrightarrow{S_1}$ and $\overrightarrow{S_2}$ denote the 3D position vectors of sensors 1 and 2, respectively, while $\overrightarrow{R_1}$ and $\overrightarrow{R_2}$ denote the sensor-object vectors of two radar rays. The complanarity condition can be interpreted as the intersection of range spheres and Doppler cones and thus two range equations and two Doppler equations. In the general case of zero-Doppler geometry, meaning that the target is acquired on a heading that is perpendicular to the flying direction of satellite, they can be written as:

$$\begin{array}{l} |\overrightarrow{P} - \overrightarrow{S_1}| = |\overrightarrow{R_1}| = R_1 \\ |\overrightarrow{P} - \overrightarrow{S_2}| = |\overrightarrow{R_2}| = R_2 \end{array} \tag{3.13}$$

$$\begin{array}{l} \overrightarrow{V_1} \cdot (\overrightarrow{P} - \overrightarrow{S_1}) = 0 \\ \overrightarrow{V_2} \cdot (\overrightarrow{P} - \overrightarrow{S_2}) = 0 \end{array} \tag{3.14}$$

where $\vec{V_1}$ and $\vec{V_2}$ denote the 3D velocity vectors of sensors 1 and 2, respectively. In essence, Equations 3.13 and 3.14 represent the stereo model of radargrammetry. The accuracy of DEM by radargrammetry is affected by:

- terrain features such as topographic slopes;
- geographical conditions and geometric distortions in relation to radar looking angles;
- intersection angle.

Toutin (Toutin [2002]) has found that the DEM accuracy is almost linearly correlated with the terrain slopes with the larger errors in the steepest slopes. He also found that for the aspect the best and the worst results generally occur in the foreslopes and backslopes and that the more pronounced the relief, the higher the correlation between the elevation accuracy and the aspect.

Principles of Interferometric SAR

SAR interferometry, also called InSAR (Interferometric SAR), is the technique that from a pair of SAR images of the same area taken at slightly different positions, the master and the slave image, allows to compute an interferogram and to use the phase differences recorded in it to derive a topographic map of the Earth's surface. The interferogram is calculated multiplying one image by the complex conjugate of the other one. The interferogram is a complex

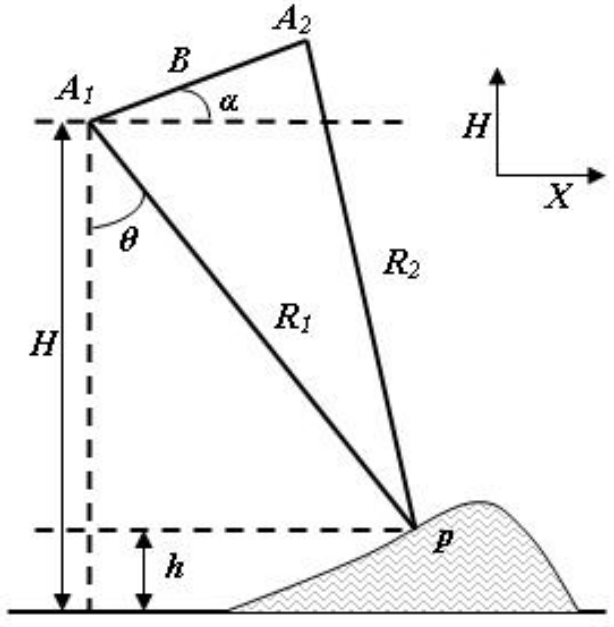

Figure 3.9: Geometry of SAR imaging for heighting.

image too and its phase equals the phase difference between the two images. According to wave propagation theory, the phase delay measured by the antenna, proportional to the slant-range R between the antenna and the target point, is:

$$\Phi = \frac{4\pi R}{\lambda} \tag{3.15}$$

Assume $\hat{S}_1$ be the complex image taken at position A_1 with its phase component Φ_1 and $\hat{S}_2$ the complex image taken at position A_2 with its phase component Φ_2 as shown in Figure 3.9.
Then the interferogram phase is equal to:

$$\phi = \Delta\Phi = \Phi_2 - \Phi_1 = \frac{4 \cdot \pi \cdot \delta R}{\lambda} \tag{3.16}$$

The interferometric SAR phase depends on the change in the nature and geometric distribution of the scatterers occurred between the acquisitions of the two images and on the propagation time difference of the radar wave between the two-way paths, master-footprint and slave-footprint. Quantitatively, temporal as well as spatial decorrelation can be measured by their reduction of coherence γ which is the correlation coefficient of two complex SAR images $u_1[i,k]$, $u_2[i,k]$ defined as:

$$\gamma[\cdot] = \frac{|E\{u_1[\cdot]\, u_2^*[\cdot]\}|}{\sqrt{E\{|u_1[\cdot]|\}\, E\{|u_2[\cdot]|\}}} \tag{3.17}$$

where $E\{\cdot\}$ represents a two-dimensional local average in the image plane. From Equation 3.16, the slant range difference (δR) between R_1 (the distance from a target point P to A_1) and R_2 (the distance from a target point P to A_2) can be calculated by the following formula:

$$\delta R = R_1 - R_2 = \frac{\lambda}{4 \cdot \pi}\phi \tag{3.18}$$

where λ is the wavelength. When $B << R_1$ the difference between two slant ranges can be approximated by the baseline component in the slant direction (i.e., the so-called parallel baseline, see Figure 3.10) as in Equation 3.19:

$$\delta R \approx B_{\parallel} = B\sin(\theta - \alpha) \tag{3.19}$$

where θ is the side-looking angle. Then the following relation holds:

$$\sin(\theta - \alpha) = \frac{R_1^2 + B^2 - R_2^2}{2BR_1} = \frac{R_1^2 + B - (R_1 + \delta R)^2}{2BR_1} \tag{3.20}$$

and since:

$$\theta = \sin^{-1}\left(\frac{\lambda \cdot \phi}{4\pi \cdot B}\right) + \alpha \tag{3.21}$$

the heigth of the point P (from P to the same reference datum) can be derived from the following equation:

$$h = H - R_1 \cdot \cos\theta \tag{3.22}$$

where α is the angle of the baseline with respect to the horizontal line and H is the flying height. From Equation 3.22 it can be seen that to compute the height a precise estimate of the baseline and a precise computation of the phase difference are necessary.
Assuming that the baseline can be determined by a GPS instrument on board, the discussion focuses on the determination of the phase difference ϕ. First of all, an operation of co-registration between the master and the slave image is required since the two images may have different orientations due to different antenna attitudes at different times. The processing consists in a transformation of the two images in the same reference system and in a resampling, usually using bilinear interpolation, into pixels with the same size in terms of ground distance so that they could match each other. The transformation is usually modelled by a polynomial function whose

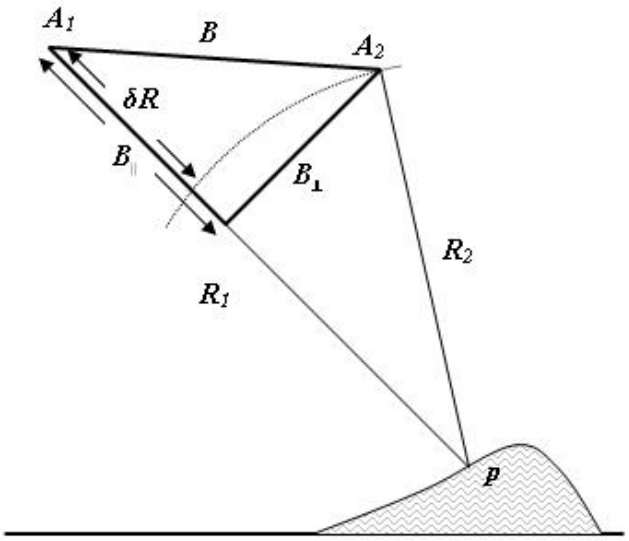

Figure 3.10: Across - track InSAR configuration.

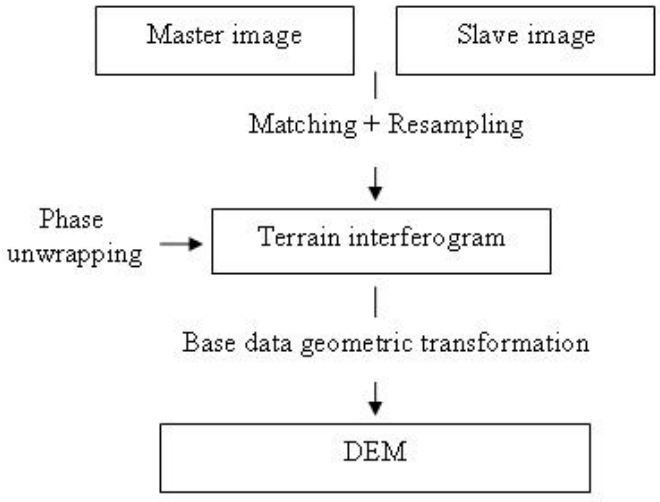

Figure 3.11: The process of DEM data acquisition by InSAR.

coefficients are estimated using some points, considered as control points, of known coordinates. Image-matching techniques are used to find for each point of the master image the corresponding point in the slave image. Once the images are co-registered, the interferometric phase can be computed but only in principal value (from -ϕ to ϕ) since the integral number of microwave cycle is unknown. A data processing, called phase unwrapping, based on the information of neighbouring pixels, has been developed to solve this problem and find the full value of the interferogram phase. Figure 3.11 shows an example of interferometric phase.

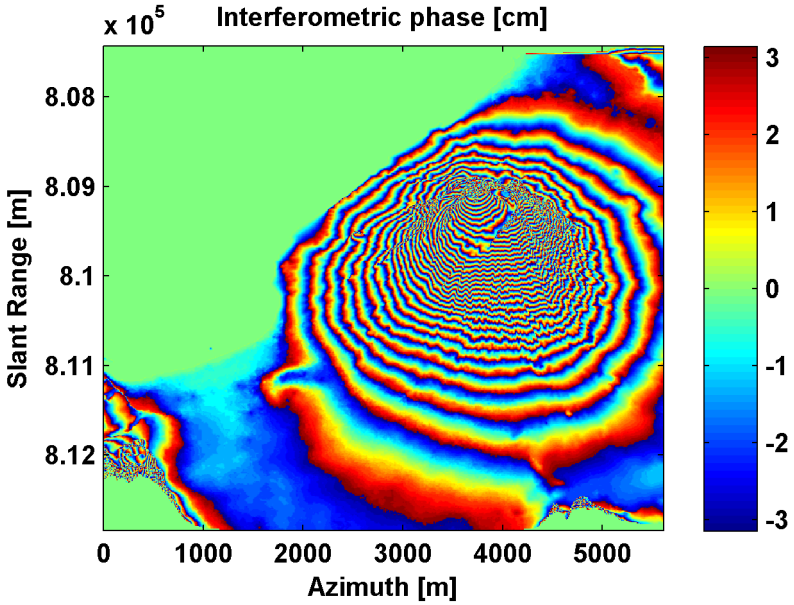

Figure 3.12: Example of interferogram, after flattening (Vesuvio volcano, Southern Italy).

Differential SAR Interferometry

A short parenthesis can be opened to illustrate differential SAR interferometry (DInSAR) which is the technique that allows to measure directly the movement of a point along the LOS direction (the SPINUA and SBAS algorithms illustrated in Section 2.2 apply this technique). In fact, if the two SAR images are acquired from the same position (i.e. the baseline has a zero length), the interferogram measures directly the displacement undergone by the terrain in the antenna-target direction. DInSAR exploits this potentiality eliminating from classical interferograms (i.e. generated with the ordinary baseline configurations) the effects of terrain topography. This is done using

at least three images or two SAR images and a pre-existing DEM of the imaged scene.
The former case can be explained as follows. Consider 3 passes M, S and S' of the same satellite over a given area (Figure 3.13).

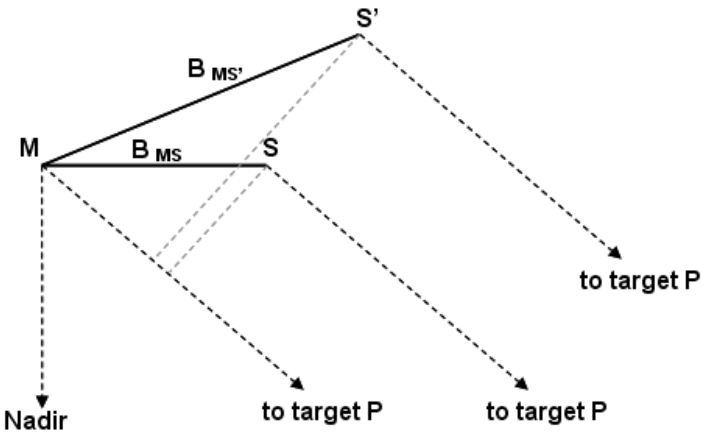

Figure 3.13: Differential InSAR geometry.

The interferometric phase differences due to the different antenna-footprint travel paths are:

$$\phi_{MS} = \frac{4 \cdot \pi}{\lambda} \delta R_{MS} = \frac{4 \cdot \pi}{\lambda} B_{MS_{\parallel}} \tag{3.23}$$

$$\phi_{MS'} = \frac{4 \cdot \pi}{\lambda} \delta R_{MS'} = \frac{4 \cdot \pi}{\lambda} B_{MS'_{\parallel}} \tag{3.24}$$

where $B_{\parallel}$ is the component of the baseline parallel to slant range direction (Eq. 3.19). The ratio between the phase differences

$$\frac{\phi_{MS}}{\phi_{MS'}} = \frac{B_{MS_{\parallel}}}{B_{MS'_{\parallel}}} \tag{3.25}$$

equals the ratio between the parallel components of the baselines B_{MS} and $B_{MS'}$ and hence is totally independent of terrain topography. Let us assume a terrain deformation between the S and S' satellite passages which originates a displacement of several pixel footprints that does not affect the correlation of the SAR images acquired before and after the displacement. In this case, a new phase term, corresponding to the component $\Delta\rho$ of the displacement along the slant range direction (LOS), is added to the term dependent of the

topography:

$$\phi_{MS'} = \frac{4 \cdot \pi}{\lambda} \cdot \left(B_{MS'_{\parallel}} + \Delta\rho \right) \tag{3.26}$$

The phase contains both the information about the terrain topography and the one about the terrain displacement. Usually phase variations due to movements can not be distinguished from ones generated by the topography and this the reason why it is not possible to measure terrain displacements using only one interferogram. A second interferogram has to be employed; firstly, it has to be unwrapped and then multiplied by the ratio of the parallel baseline component. Subtracting the two interferograms, the topography term can be removed:

$$\phi_{MS'} - \frac{B_{MS'_{\parallel}}}{B_{MS_{\parallel}}} \phi_{MS} = \frac{4 \cdot \pi}{\lambda} \Delta\rho. \tag{3.27}$$

The left term of the equation is known from the interferometric phases and the orbit geometry. Hence the displacement component $\Delta\rho$ along the slant range direction can be measured for each pixel of the double difference interferogram. The other way to recover the displacement field from a single interferometric image pair is, as said before, to use a DEM of the imaged scene. The effect of the topography in fact can be removed simulating a synthetic interferogram with the DEM and the orbital parameters of the two SAR images; then it can be subtracted from the real one, leaving the phase related to terrain movement (Crosetto [1998]).
To have a detailed review of SAR interferometry, see, e.g. Bamler and Hartl (Bamler and Hartl [1998]).

3.3 DEM construction

The architecture of a DEM derives from the model used to represent it. At the end of data acquisition process, a relatively unordered set of data elements is available. It can be used to construct a usable DEM only if the topological relations between data as well as an interpolation model that approximates the surface behaviour are defined. It is important to remember that an optimal surface model should:

- represent accurately the surface;
- be suitable for efficient data collection;
- minimize data storage requirements;

- maximize data handling efficiency;
- be suitable for surface analysis.

Interpolation can be defined as the process of estimating the value of attributes at a certain site from measurements made at surrounding point locations, which are denoted as *sample-reference points*. Interpolation methods can be classified according to different criteria:

- exact or inexact interpolation methods;
- global or local interpolation methods;
- stochastic or deterministic interpolation methods.

Exact interpolation generates a surface that passes through the reference points. If this is not the case, the interpolation method is defined as a inexact interpolator and the differences between the given and interpolated elevations are used to define the quality of the interpolator itself.
A global interpolation uses all the available samples to estimate the elevation at the interpolation points, while a local interpolation estimates the unknown elevations using the elevations associated with the nearest sample points.
In deterministic interpolation the assumptions on the Earth surface regularity are implicitly made by representing this surface as a combination of given functions. Stochastic methods derive this information from the sampled data, by computing statistics such as the empirical covariance function or the empirical variogram.
It can be underlined that the interpolation is applied twice: an interpolation method permits to go from the set of acquired height data to the model. For example from a set of sparse points a model of ASCII grid format is construct giving a series of coordinates on a set of equally distributed points. Once the model is built, the user has to define an interpolation method to compute the height of whatever point located in the domain.
The topographic modeller should be very careful in selecting the technique to interpolate the initial sampling data points of altitude because it can affect considerably the DEM quality.
More in Aguilar et al. [2005] and Chaplot et al. [2006].

3.4 Quality of DEMs

Several factors affect the quality of DEMs. An initial source of errors can be attributed to the data collection since the quality of the estimated height

depends on the acquisition technology applied (see Table 3.1). Other sources of error include the spatial structure of altitude and the interpolation technique for DEM generation, in particular the last one can have a great impact on the quality of a DEM.
The accuracy of a DEM is evaluated comparing the DEM data with a set of **check points** measured by using high precision methods. The pairwise comparison (each check-point value is compared by the value given by the model in the same position) allows the calculation of the mean error (ME), the root mean square error (RMSE), the standard deviation and similar statistics. The RMSE is the measure most frequently used both in experimental and in theoretical analysis of DEM accuracy (Li [1988]) and it was used also in this validation/fusion work. It is defined as:

$$RMSE = \sqrt{\frac{\sum DH_i^2}{N}} \tag{3.28}$$

where DH_i represents at each i-th check point the difference between the model and the real surface and N the number of DH. Figure 3.14 can be helpful to understand what this value represents: T is the terrain surface while M the surface modelled by the DEM.

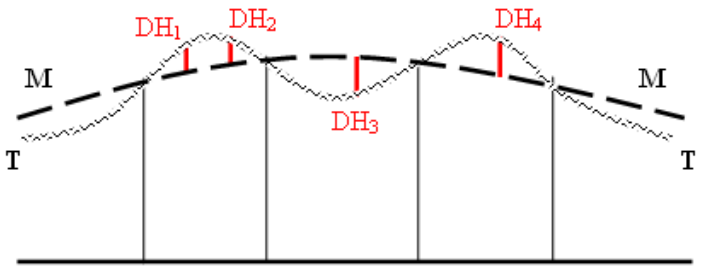

Figure 3.14: The terrain surface, DEM surface and check points.

These points must be very accurate and enough to guarantee error control reliability. The evaluation of a DEM accuracy depends on the kind of check points used, on their number and on their distribution. Cuartero et al. [2005] reported that common sources of check points are topographic contour maps, whose accuracy is not well known and that the error control is frequently performed with a number of points that is insufficient to guarantee the test reliability. The number of check points is an important factor in reliability influencing the range of stochastic variations of the SD values. The estimate of errors in a DEM is usually made by following the U.S. Geological Survey

recommendation of a minimum of 28 check points but it has been showed that many more points are needed to achieve a reliability closer to what is accepted in more statistical tests.
The expression that relates reliability to the number of check points is:

$$R(e) = \frac{1}{\sqrt{2(n-1)}} \times 100\% \tag{3.29}$$

where R(e) represents the confidence value in percentage, and n is the number of check points used in the accuracy test. So 100 check points are needed to obtain a SD value of 5%; with 28 check points the confidence value reached is equal to 20%.
Another way to evaluate the accuracy of a DEM is considering the height difference (DH) between the DEM surface and the terrain surface as a random variable. The *extreme values* of the set of values assumed by the variable DH, DH_{min} and DH_{max}, indicate the general location of all the other values and the *range* R, defined as:

$$R = DH_{max} - DH_{min} \tag{3.30}$$

can be taken as a measure of the dispersion of the random variable. The use of the range may be considered a poor measure of the accuracy of a DEM since it depends only on two values and it ignores the probability distribution of the variable DH.
Other powerful measures are the *mathematical expectation* and *standard deviation* of the variable. Considering DH as a random variable, then the set $DH_1, DH_2, ..., DH_n$ represents a sample from this variable with a frequency of 1/N if N check points are used. By definition, the sample mean of $DH(\overline{DH})$ and the standard deviation ($SD(DH)$) may be computed as follows:

$$\overline{DH} = \frac{\sum_i DH_i}{N} \tag{3.31}$$

$$SD(DH) = \sqrt{\frac{\sum_i (DH_i - \overline{DH})^2}{N}} \tag{3.32}$$

Consequently a combination of the mathematical expectation and standard deviation can be used as a measure of the DEM accuracy as follows:

$$Ac = \overline{DH} + SD(DH). \tag{3.33}$$

3.5 DEM available on the area of Como

The DEMs available in the area of Como and used for this study are:

- a LiDAR DSM;
- a DSM from photogrammetry;
- the ASTER DSM;
- the SRTM DSM.

These models are described in the following sections with a level of detail that depends on the available information. Particular attention is dedicated to ASTER and SRTM DSMs since they were used as test fields during the fusion studies when COSMO-SkyMed data were not yet available (Chapter 5).

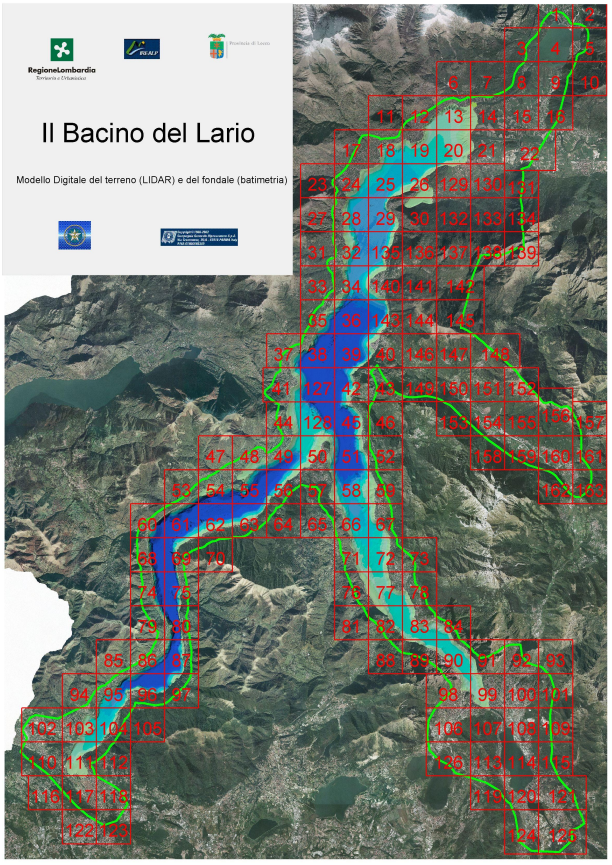

Figure 3.15: LiDAR data distribution.

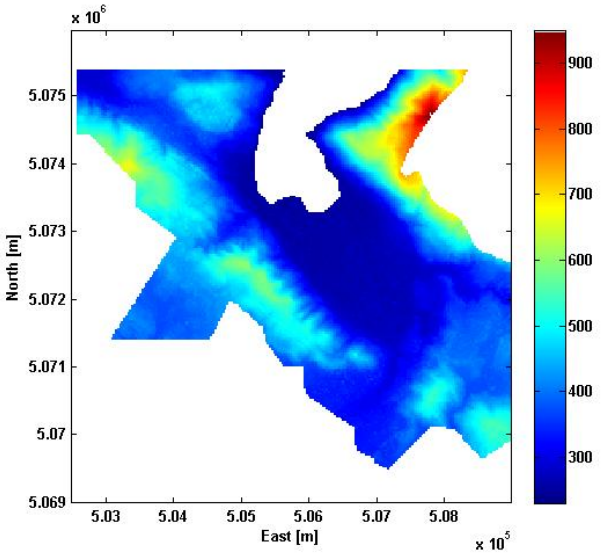

Figure 3.16: LiDAR DSM.

3.5.1 LiDAR DSM

Regione Lombardia made a LiDAR campaign on the area covered by the lake of Como (northern Italy) in 2003. The dataset is composed by 126 tiles but for this work just the tiles covering the city of Como were considered; they are tiles 110, 116, 117, 118, 122, 123 in Figure 3.15. For these tiles, Regione Lombardia delivered to the Laboratory of Geomatica of Como the raw data of this LiDAR survey, in particular the data referring to first and last pulses. Data refers to ellipsoidal heights in ETRF89, projected in UTM32. Filtering techniques have been applied to create a DSM with a resolution of 2m x 2m and an accuracy of about 50cm. The calculation was done using some routines developed in GRASS (Brovelli and Lucca [2009], Lucca [2012]). This DSM is extended 8km in East and 6km in North. It is in ASCII-grid format and it is shown in Figure 3.16.

3.5.2 DSM from photogrammetry

This DSM was cut off from a DSM delivered by Regione Lombardia, created using images acquired after 2007. The product came from a unique acquisition process done using a digital photocamera and an GPS-IMU instrumentation for direct georeferencing of images. It is in ASCII-grid format and its characteristics are reported in Table 3.2. Its extension is visible in Figure

3.17.

Resolution	2m
Extension	Lombardy
Accuracy	1.5m in height
Height	Orthometric
Reference system	Version # 1: Roma 40 Version # 2: WGS84-IGM95 (ETRF89)
Reference coordinate	Version # 1: Gauss-Boaga west fuse Version # 2: UTM fuse 32

Table 3.2: Characteristics of DSM from photogrammetry.

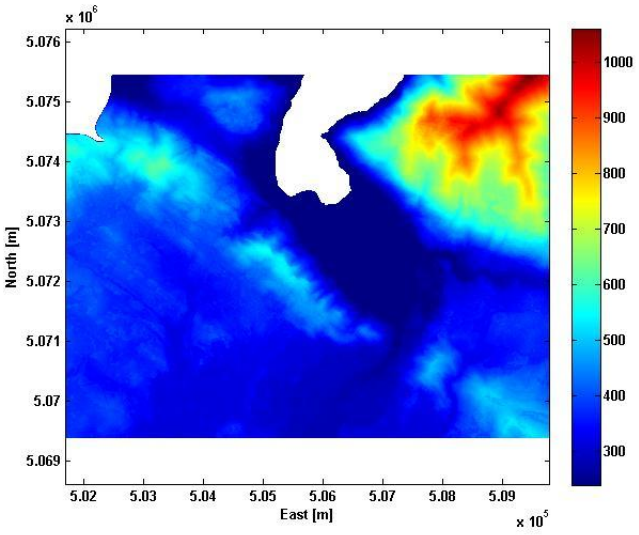

Figure 3.17: DSM from photogrammetry.

3.5.3 ASTER DSM

ASTER (Advanced Spaceborne Thermal Emission and Reflection Radiometer) is a high-resolution multispectral sensor built by METI (Ministry of Economy, Trade and Industry of Japan) on board the National Aeronautics and Space Administration's (NASA's) Terra satellite that was launched in December 1999. Figure 3.18 shows the satellite Terra and the ASTER sensors mounted

on it [4]. Table 3.3 summarizes the characteristics of Terra ASTER that has been acquiring data in operational mode since March 2000.
Images are acquired in 14 spectral bands using three separate telescopes and sensor systems.

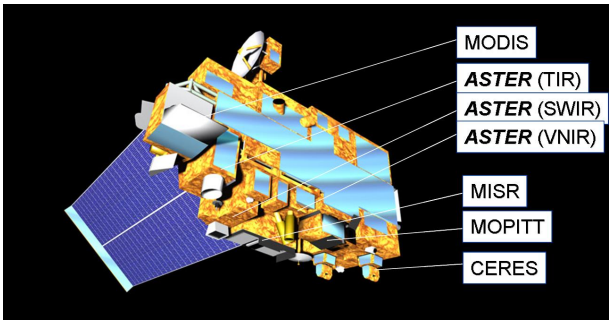

Figure 3.18: The satellite Terra and the ASTER sensors.

Technical specifications Terra ASTER stereo	
Bands in visible/near-infrared	3
Bands in short wavelength infrared	5
Bands in thermal infrared	6
Stereo capability	Yes Bands 3N and 3B (nadir and aft-looking telescopes) 0.78-0.86 μm
Stereo imaging geometry	Along-track
Base-to-height(B/H) ratio	0.6
Pixel size	15 m
Scene coverage	60 Km x 60 Km
Orbital path	Near-polar sun-synchronous
Orbital altitude	705 Km
Orbital inclination	98.2°
Repeat cycle	16 days

Table 3.3: Technical specifications of ASTER sensor and Terra satellite orbital parameters.

[4]This figure has been taken from a presentation on ASTER given in August the 2^{nd}, 2005 at JPL by Mike Abrams (http://asterweb.jpl.nasa.gov/bibliography.asp).

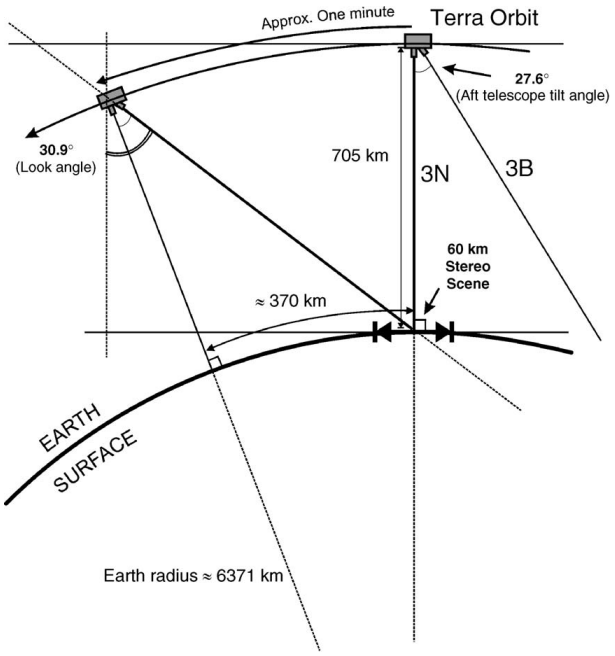

Figure 3.19: Simplified diagram of the ASTER along-track stereo imaging geometry.

These include three visible and near-infrared (VNIR) bands with a spatial resolution of 15m, six short-wave-infrared (SWIR) bands with spatial resolution of 30m and five thermal infrared (TIR) bands that have spatial resolution of 90m. VNIR Band3 is also acquired using a backward looking telescope, thus providing along track stereo coverage, at a base-to-height (B/H) ratio of 0.6, from which high quality digital elevation model are generated. Figure 3.19 [5] shows the ASTER along-track stereo imaging geometry.

ASTER provides different standard data products whose characteristics are reported in Table 3.4 (from Jet Propulsion Laboratory).

ASTER DEM standard data are produced with 30m postings, and have Z accuracies generally between 10m and 25m as RMSE. A DEM can be created as a Relative DEM (no ground control) or an Absolute DEM (with ground control, which must be supplied by the user). These high spatial resolution DEMs (up to 7m absolute horizontal and vertical accuracy with appropriate ground control, and up to 10m relative accuracy without ground control) can be used to derive absolute slope and aspect good to 5 degrees

[5] from Hirano et al. [2003]

Level	Product	Description
1A	Radiance at sensor	Image data plus radiometric and geometric coefficients. Data are separated by telescope
1B	Registered radiance at sensor	1A data with radiometric and geometric coefficients applied
1AE	Radiance at sensor	Expedited L1AE data product created from ASTER Expedited Level-0. Image data plus radiometric and geometric coefficients. Data are separated by telescope
1BE	Registered radiance at sensor	Expedited L1BE data product created from ASTER Expedited Level-1AE. 1AE data with radiometric and geometric coefficients applied
2	AST09 Surface radiance-VNIR,SWIR	Radiance corrected for atmospheric effects
2	AST09T Surface radiance-TIR	Radiance corrected for atmospheric effects
2	AST09XT Surface radiance-VNIR,SWIR Crosstalk Corrected & Radiance corrected for atmospheric effects - VNIR	Crosstalk Corrected SWIR
2	AST07 Surface reflectance-VNIR,SWIR	Derived from surface radiance with topographic corrections
2	AST07XT Surface reflectance-VNIR,SWIR Crosstalk Corrected	Derived from surface radiance with topographic corrections - VNIR & Crosstalk Corrected SWIR
2	AST08 Surface kinetic temperature	Temperature-emissivity separation algorithm applied to atmospherically corrected surface radiance data
2	AST05 Surface emissivity	Temperature-emissivity separation algorithm applied to atmospherically corrected surface radiance data
3	ASTER GDEM	Global Digital Elevation Model (GDEM), 1 x 1 degree tiles, 30m postings, GeoTIFF format
3	AST14 Digital elevation model	DEM produced by stereo correlation of nadir and aft Band 3 data
	AST14OTH Orthorectified AST14DMO Orthorectified + DEM	15 orthorectified L1B radiance images, in GeoTiff 15 orthorectified L1B images + DEM

Table 3.4: Definition/specifications for ASTER DEM data products.

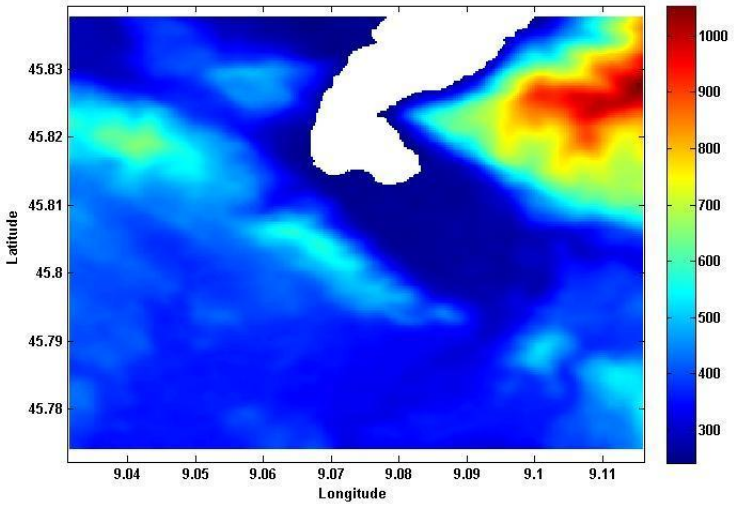

Figure 3.20: ASTER DSM.

over horizontal distances of more than 100m. ASTER DEMs should meet $1:50,000$ to $1:250,000$ map accuracy standards (Abrams et al. [2002]).
An ASTER Global Digital Elevation Model (GDEM) was released to the public on June 29^th 2009. It was created processing automatically 1.5 million scenes to produce approximately 1.3 million single-scene ASTER DEMs.
ASTER GDEM is in geotiff format with geographic (latitude, longitude) coordinates and a 1 arc-second (30m) resolution; it covers land surfaces between latitude 83°N and 83°S.
The ASTER GDEM validation report (Team [2009]) indicates a RMSE of about 10m for United States but it is said that this value can be extrapolated with confidence to other parts of the world and that the overall accuracy of the ASTER GDEM, on a global basis, can be taken approximately 20m at 95% confidence for vertical data.
The ASTER DSM used is this work is part of this ASTER Global Digital Elevation Model and it is represented in Figure 3.20.

3.5.4 SRTM DSM

The Shuttle Radar Topography Mission (SRTM) was jointly performed by NASA, the German Aerospace Center (DLR) and the Italian Space Agency (ASI).
Between February 11^{st} and 22^{nd} 2000, two antenna pairs operating in C and X bands were simultaneously illuminating and recording radar signals on

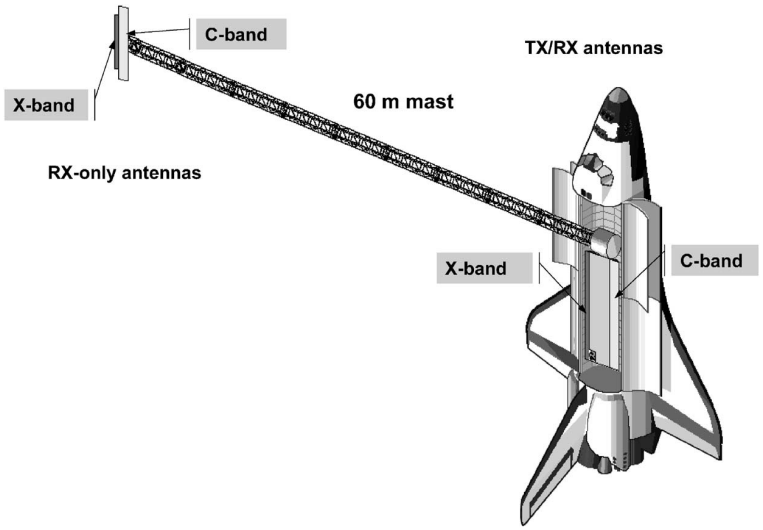

Figure 3.21: SRTM space segment.

board the Shuttle Endeavour. It was the first single-pass interferometer in space. Two single-pass interferometers were built and operated in parallel: the master channels (to transmit and receive) of both interferometers used the original components in the shuttle cargo bay, the secondary (receive-only) antennas were mounted at the tip of a 60m long lightweight mast as shown in Figure 3.21.
Two different products can be generated from the radar data provided by the in and on board antennas: the interferometric DEM (generated as explained in Section 3.2.3) and image products derived from data recorded by the inboard antenna. The mission had provided the first global high-quality DEM at a resolution level of 1 arc sec (not available) and 3 arc sec, characteristics of which are summarized in Table 3.5. It is important to underline that data at 1 arc sec resolution are available just for North America while for the rest of the world just the 3 arc sec resolution DSM, obtained as a mean of the DSM at 1 arc sec resolution, is published. For this reason the SRTM DSM was considered as a mean DSM during the validation/fusion work. For more details about the mission see Rabus et al. [2003].

SRTM DSM was validated using a globally distributed set of ground control points acquired using Kinematic Global Positioning System. Table 3.6 reports the result of this validation (see Rodriguez et al. [2006] for more details).

Figure 3.22 shows the SRTM DSM for the area of Como.

Resolution	3 arc sec
Extension	from 57°S to 60°N latitude
Realization year	2000
Accuracy	±16 m as absolute vertical accuracy ±6 m as relative vertical accuracy [1]
Height	Orthometric
Reference system	WGS84

[1] The relative accuracy describes the error in a local 200 km scale while the absolute value stands for the error budget throughout the entire mission. The precision shall be valid for 90% of the data, i.e. the error represents about 1.6 SD.

Table 3.5: Characteristics of SRTM GDSM.

	Africa	**Australia**	**Eurasia**	**Islands**	**N. America**	**S. America**
Absolute Geolocation Error	11.9	7.2	8.8	9.0	12.6	9.0
Absolute Height Error	5.6	6.0	6.2	8.0	9.0	6.2
Relative Height Error	9.8	4.7	8.7	6.2	7.0	5.5

Table 3.6: SRTM validation results. All quantities represent 90 percent errors in meters.

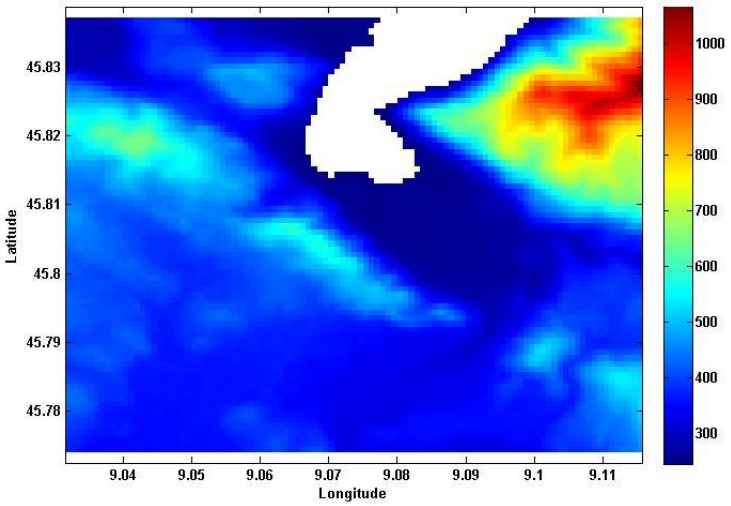

Figure 3.22: SRTM DSM.

Chapter 4

DEMs validation within the COSMO-SkyMed project

This Chapter reports a DEM validation procedure. It was developed in view of the COSMO-SkyMed products validation, but before those data were made available to the project. We studied and applied it to the validation of two different DSMs, used as test fields: the ASTER point-wise DSM (Section 3.5.3) and the SRTM average DSM (Section 3.5.4). The validation was performed in two ways.
The first one consists in comparing the information of each node of a grid with the one brought by the points laying in its neighbourhood; since this validation does not require additional information but the DEM itself, it is called "internal validation" and is reported in Section 4.1.
The second one consists in comparing the validating DEM with another model characterized by higher accuracy and resolution; in this case the LiDAR DSM was considered as the reference model. Since it requires an external source of information it is called "external validation" and it is explained in depth in Section 4.2.

4.1 Internal Validation

This validation procedure was implemented within GRASS by Triglione during his master thesis (Triglione [1999]). The purpose of internal validation is to find outliers in a dataset of gridded points distributed on a bidimensional surface. This is done on one point at a time making an estimate of its height and dispersion coefficient at a local level. This estimated value is then compared with the observed one by a proper statistical test procedure; the observation is considered an outlier if significantly different from the

prediction from its neighbours.
The prediction is made by assuming the interpolating surface to be a polynomial function (from a constant plane to a bicubic surface) whose parameters are estimated via least squares. Robust predictions are used as well.
Since a DEM is a matrix of big dimensions, the interpolation of all the data with a unique model of very high degree is completely meaningless because it requires enormous memory availability and very long calculation times to obtain disappointing results in term of precision. Therefore outlier identification is done considering local functional models: iteratively the attention is focused on each DEM element and on the points in its neighbourhood. For this purpose a window of odd dimension centred in point $P(x_0, y_0)$ scrolls the grid as a mask and gives the appropriate importance to the information of the nearest points.
With this generic approach it is possible to study the behaviour of the data illuminated by the window, making linear (and not linear) filtering and statistical inference to understand on the base of the behaviour of the other points, with a given significant level, if the generic point $P(x_0, y_0)$ is reliable or not. A basic assumption is that the argument values associated to the mask are affected by white noise which represents the difference between the measurements and the correct model. Interpolating surface choice influences the value of the residual between estimated and measured values and determines the judgement on the observed central value $P(x_0, y_0)$. The software gives the possibility to chose between different type of interpolating surface:

1. mean horizontal plane
$$h_{ms}(x, y) = a_0 \tag{4.1}$$
(with just 1 parameter a_0, in the case of least square estimate it corresponds to the sampled mean);

2. linear surface
$$h_{lin}(x, y) = a_0 + a_1 x + a_2 y \tag{4.2}$$
(with 3 parameters: a_0, a_1, a_2);

3. bilinear surface
$$h_{bil}(x, y) = a_0 + a_1 x + a_2 y + a_3 xy \tag{4.3}$$
(with 4 parameters: a_0, a_1, a_2, a_3);

4. quadratic surface
$$h_{quad}(x, y) = a_0 + a_1 x + a_2 y + a_3 xy + a_4 x^2 + a_5 y^2 \tag{4.4}$$
(with 6 parameters: $a_0, a_1, a_2, a_3, a_4, a_5$);

5. biquadratic surface

$$h_{biq}(x,y) = a_0 + a_1x + a_2y + a_3xy + a_4x^2 + \\ + a_5y^2 + a_6x^2y + a_7xy^2 + a_8x^2y^2 \tag{4.5}$$

(with 9 parameters: $a_0, ..., a_8$);

6. bicubic surface

$$h_{bic}(x,y) = a_0 + a_1x + a_2y + a_3xy + a_4x^2 + a_5y^2 + \\ + a_6x^2y + a_7xy^2 + a_8x^2y^2 + a_9x^3 + a_{10}y^3 + \\ + a_{11}xy^3 + a_{12}x^3y + a_{13}x^2y^3 + a_{14}x^3y^2 + a_{15}x^3y^3 \tag{4.6}$$

(16 parameters: $a_0, ..., a_{15}$).

Whatever is the chosen surface $h(x, y)$, data model is described by the following observation equation:

$$h_{oss,i} = h\,(x,y) + \nu_i, \quad i = 1, 2, ..., m \tag{4.7}$$

where $\nu_i \sim \mathbf{N}\,[\mathbf{0}, \sigma_0^2\,\mathbf{I}]$.
The reliability of the mask central value $h_{oss,0} = h_{oss}\,(0,0)$ can be infered from the gap between $h_{oss}\,(0,0)$ itself and its estimate $\hat{h}_0$ evaluated from neighbouring observations in accordance with the assumed model.
The hypothesis to test is:

$$H_0 : \Delta h = |h_{oss,0} - \hat{h}_0| = 0 \tag{4.8}$$

with a statistic $S\,(\mathbf{h}, \Delta h)$ that grows in modulus when Δh grows and descreaseas as much as the deterministic model (the interpolator) is adequate to explain the observation. Therefore $h_{oss,0}$ is suspected to be an outlier if the empirical value of the statistic overcomes a costant estabilished on the base of theoretical considerations. Once defined the metodology to make the test, interpolation model, mobile window size and significant level α should be set. A command called *r.outldetopt* helps the user in choosing the optimal method of interpolation and the moving window size on the base of the specific dataset under analysis (for more details on how this program works see Triglione [1999]). Table 4.1 reports the interpolation method and the moving window size used for the validation of ASTER and SRTM DSMs.
The statistics $S\,(\mathbf{h}, \Delta h)$ of known distribution when the hypothesis

$$H_0 : \Delta h = 0 \tag{4.9}$$

DEM	Interpolation method	Window size
ASTER	bilinear	5x5
SRTM	bilinear	5x5

Table 4.1: Interpolation method and window size used in validation.

is true is distributed as a t of Student with $N_k - m$ degrees of freedom, where N_k is the number of data contained in the moving window (the central value is not counted) and m represents the number of parameters of the interpolating model.

$$S = \sqrt{\frac{N_k}{N_k+1}}\frac{\Delta h}{\hat{\sigma}_0} = \sqrt{\frac{N_k}{N_k+1}}\frac{\Delta h}{\sigma_0}\frac{\sigma_0}{\hat{\sigma}_0} \sim \frac{Z}{\sqrt{\frac{\chi^2_{N_k-m}}{N_k-m}}} = t_{(N_k-m)} \tag{4.10}$$

For example, if the interpolating method is bilinear and the window side dimension is 5, the statistics has degree of freedom equal to $N_k - m = 24 - 4 = 20$. Once the statistic has been defined, the distinction between what is an outlier and what not depends on the value of significance α used in the test on the normalized residuals. The value of α used to make the test is fixed in an adaptive way to avoid to consider as outliers too many points (when α is too high) or too few (when α is too low). More precisely, the significance level α is established on the base of the effective nature of the data: a threshold beyond which is reasonable to consider the observations as "unlikely" can be deduced comparing the distribution curve of the normalized absolute residuals (empirical values of the t of Student distribution) with the homologous theoretical distribution curve. The chosen alpha is the one that corresponds to the intersection between these two curves; for more details see the reference Triglione [1999].

4.1.1 Internal Validation of ASTER DSM

In Table 4.2 the absolute and the relative frequencies of the empirical t for the ASTER DSM are reported while Table 4.3 shows the theoretical probability. In Figure 4.1 empirical and theorical cumulative distribution for ASTER are represented. The optimum value for α is 0.0108. There are 136 outliers over 70380 points (0.19%); their position is displayed in Figure 4.2.

Interval	Absolute Frequency F	Relative Frequency f=F/N
[0-1.5)	19810	0.603062
[1.5-3)	13025	0.396511
[3-4)	12	0.000365
[4-inf)	2	0.000061

Table 4.2: Frequencies of $|t_{emp}|$ for ASTER.

Interval	Probability per number of data	Probability
[0-1.5)	27947	0.850764
[1.5-3)	4670	0.142160
[3-4)	209	0.006372
[4-inf)	23	0.000704

Table 4.3: Probability of $|t_{theo}|$ for ASTER.

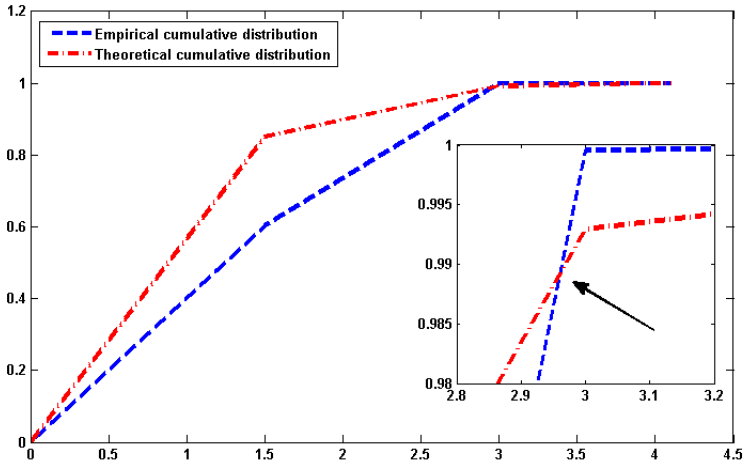

Figure 4.1: Empirical and cumulative distribution function of the statistic for ASTER.

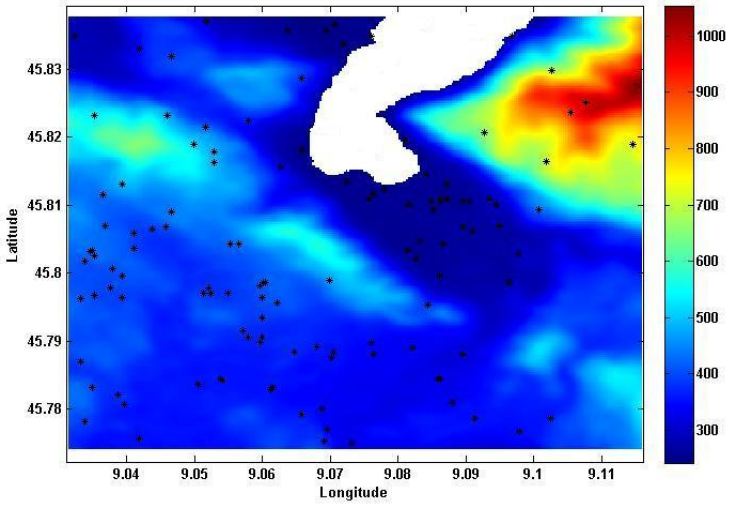

Figure 4.2: Outlier location for ASTER DSM.

4.1.2 Internal Validation of SRTM DSM

Tables 4.4 and 4.5 the empirical frequencies and the theoretical probability of the t distribution for the SRTM DSM are reported and in Figure 4.3 represented. The optimum alpha to make the outlier rejection is the one that corresponds to the intersection of this two lines: in this case the optimum value is $\alpha = 0.0112$. There are 59 outliers over 7676 points (0.77%) and their position is displayed in Figure 4.4.

Interval	**Absolute Frequency F**	**Relative Frequency f=F/N**
[0-1.5)	4921	0.754061
[1.5-3)	1586	0.243028
[3-4)	17	0.002605
[4-inf)	2	0.000307

Table 4.4: Frequencies of $|t_{emp}|$ for SRTM.

Interval	Probability per number of data	Probability
[0-1.5)	5552	0.850764
[1.5-3)	928	0.142160
[3-4)	42	0.006372
[4-inf)	5	0.000704

Table 4.5: Probability of $|t_{theo}|$ for SRTM.

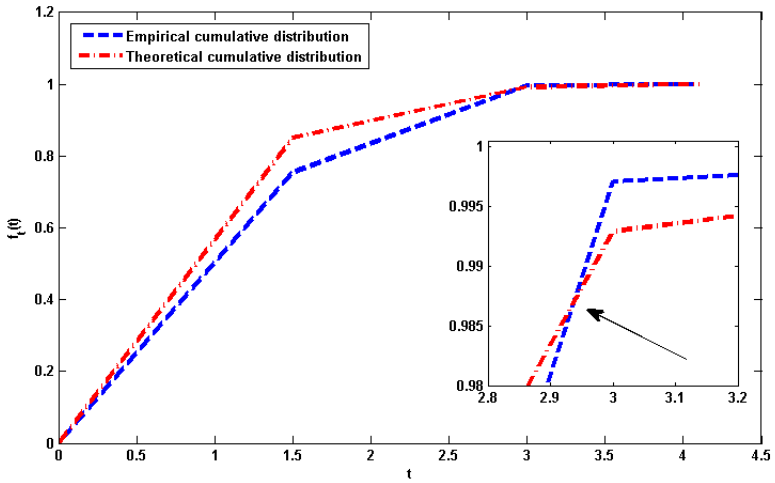

Figure 4.3: Empirical and cumulative distribution for SRTM.

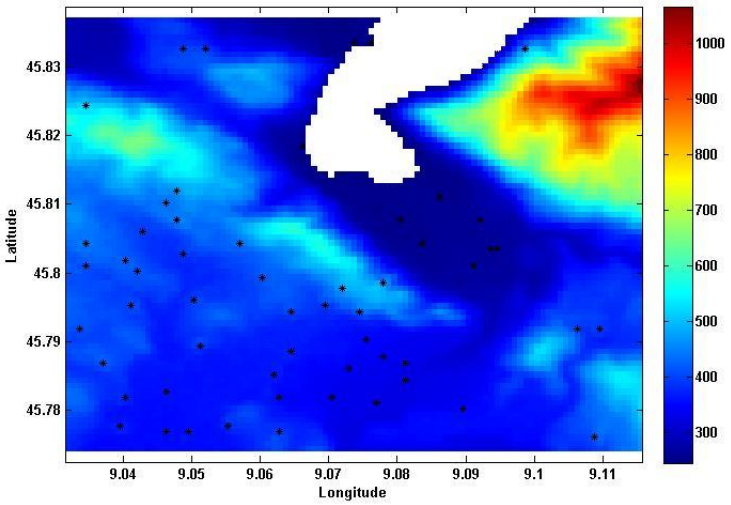

Figure 4.4: Outlier location for SRTM DSM.

4.2 External Validation

As explained at the beginning of this Chapter, the external validation of a DEM is done comparing it with a model that is more accurate an more resolute. In this case the SRTM and ASTER DEMs validation was performed against the LiDAR DSM, which is the most accurate and resolute DSM available in the test area. Notice that the SRTM DSM is an average DSM. The low resolution (3 arc second) free model used was derived making the mean of a more resolute one (1 arc second resolution). A data-preprocessing was necessary before entering the DSM comparison, it is described in the following Section 4.2.1.

4.2.1 Data pre-processing

First of all, LiDAR heights were ellipsoidal while SRTM and ASTER heights were orthometric (H); so the ellipsoidal height for ASTER and SRTM were computed following the formula:

$$h = H + N \tag{4.11}$$

where N is the geoid ondulation, in this case evaluated using the global geoid model EGM96 (Lemoine et al. [1998]). Following Eq. 4.11, the set of ASTER and SRTM geographic coordinates (ϕ, λ, H) were transformed in (ϕ, λ, h). Then, a reference system transformation was performed to transform ASTER and SRTM DEMs from geographic coordinates (ϕ, λ, h in WGS84) to cartographic coordinates (E, N, h in WGS84-UTM). The transformation was implemented because this was the reference system in which the coordinates of LiDAR points were delivered. Due to this transformation data were not anymore distributed as a grid and a gridding was necessary. This operation was done using a bilinear interpolation; many different grids were produced, different for size and position, at the end choosing the solution that best approached the LiDAR DSM. But how to make this choice? Which is the parameter that represents this "similarity" with the truth? The answer is also the principle on which the external validation was based on and it is explained in Section 4.2.2.

4.2.2 Validation

To validate something a comparison with a reference model should be done. This comparison requires that the value of the heights to be compared refers to the same position in space. At each point position, a difference between two values coming from different datasets can be calculated as:

$$\delta h_i = h1_i - h2_i \tag{4.12}$$

Here a distinction has to be done if an average DEM, as SRTM, or a point wise DEM, as ASTER, is considered.
In case of DEMs which represent a mean surface, the comparison involved mean values; put $h1_i$ be the value given by the average DEM to be validated, for example the SRTM DSM, then $h2_1$ has to be a mean value of the model used as reference, for example the LiDAR DSM. Practically, around each grid node i of coordinates E_i, N_i, h_i of the average DEM, a square area A of the dimension of the grid side, centred in $h1_i$ is created and all reference data (h_{ref}) falling in A selected (see Figure 4.5). The average of all these values h_{ref_j} represents $h2_i$:

$$h2_i = \frac{\sum_{j \in A} h_{ref_j}}{N} \tag{4.13}$$

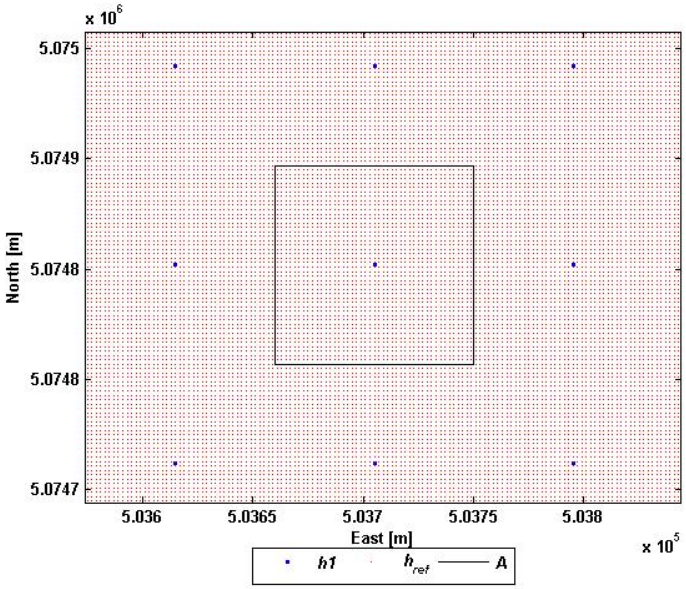

Figure 4.5: Validation of a mean DEM.

where N is the number of reference points in the area A.
In case of point-wise DEM, as ASTER, the value of δh is computed following Equation 4.12 again, but for the fact that the value $h2_i$ is the height of the LiDAR point that is nearest to the point of coordinates E_i, N_i, h_i described

by each node of the DEM under validation. Figure 4.6 helps to understand this concept.

$$h2_i = h_{ref_{NN}} \tag{4.14}$$

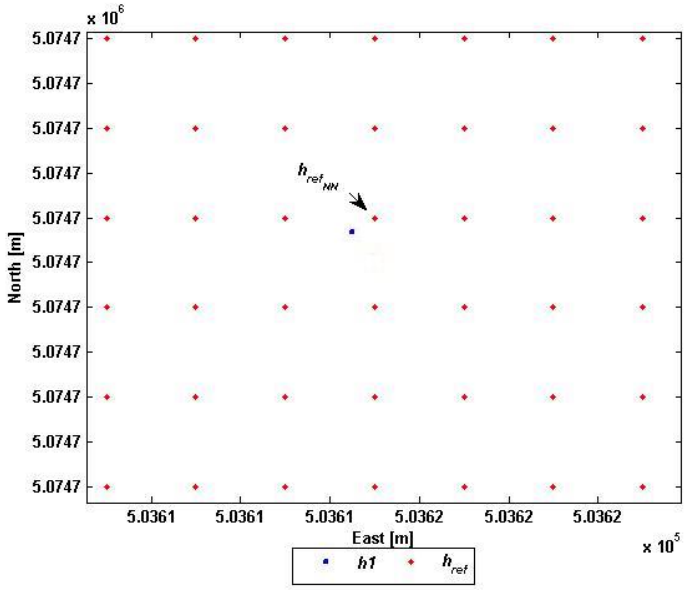

Figure 4.6: Validation of a point-wise DEM.

Basically for each node i of the ASTER grid, δh is the difference between the height of this node and the height of the reference dataset associated to that node using a nearest neighbour interpolation.
Once for each grid node of the DEM to be validated a value of δh_i is found, the mean of these delta squared, Eq. 4.15, is the sought similarity indicator:

$$\sigma^2 = \sum_i \frac{\delta h_i^2}{N} \tag{4.15}$$

where N is the number of grid node compared.
The accuracy σ of the model is given by the square of this value σ^2 and describes how the model is close to the reference DEM (this reference DEM is considered to be free of errors). A DEM is validated if this value σ^2 is less then the nominal variance given by DEMs producers. The nominal accuracy of SRTM is 16m. The value obtained comparing SRTM with LiDAR DSM is 13.20m; then the model is validated. For ASTER instead the nominal

accuracy is given in a range between 10m and 25m (Section 3.5.3) and since the one evaluated from the comparison with LiDAR in the area of Como is 12.32m, the ASTER DSM over Como can be considered validated. It can be useful to clarify a point: the position (E, N) of the points of the grid where interpolate ASTER and SRTM sparse data was chosen as the one that allows to obtain a minimum σ^2 in the comparison between the model to validate, the ASTER or the SRTM ones, and the reference LiDAR DEM. Nevertheless a sensitivity study shown that the gridding didn't influence the validation results since all the values of σ^2 found were less than the nominal accuracy of the DSMs to validate.
Another analysis was done to see if the value of σ^2 depends on surface morphological parameters such as the slope and the aspect values; it is reported in the following Section.

4.2.3 Validation based on slope and aspect classification

Before entering the validation problems, a brief introduction on the meaning of slope and aspect parameters is necessary.

Slope and aspect definition

Slope is usually measured in degrees or percentage and it is defined as the rate of change in elevation Δz over a change in lateral extent. The rate of change of elevation in both the x and y direction can be used to identify the direction and the magnitude of the steepest gradient. These two parameters can be found by taking the partial derivatives of the elevation z with respect to x and y. Therefore, slope (magnitude) can be found combining the two component partial derivatives

$$Slope = \sqrt{\left(\frac{\delta z}{\delta x}\right)^2 + \left(\frac{\delta z}{\delta y}\right)^2} \tag{4.16}$$

Elevation will change in both x and y directions, and hence the slope resulting from a change in lateral extent is the vector sum of the slope in the x direction and the slope in the y direction.
Figure 4.7 illustrates these concepts.

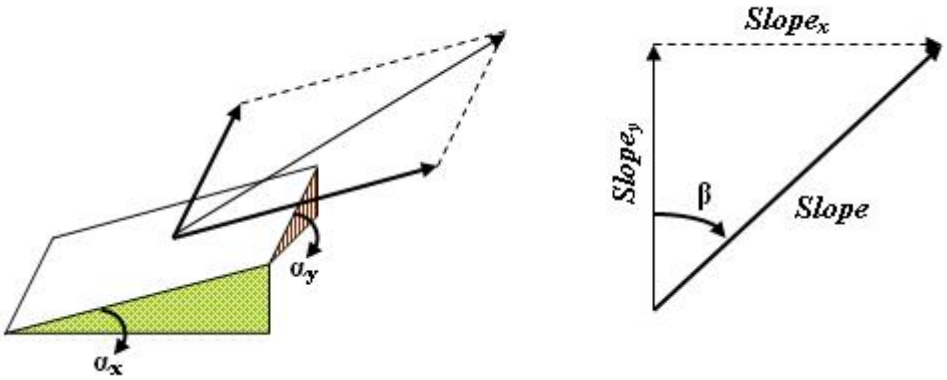

Figure 4.7: Definition of slope and aspect.

where:

- Slope in $x = \alpha_x$;
- Slope in $y = \alpha_y$.

The aspect value assigned to each cell in an aspect map represents the direction (north, south, and so forth) to which that cell is oriented. Equation 4.17 describes how that direction is computed, where β (Figure 4.7) is computed as the angle clockwise from north.

$$\tan\beta = \frac{\delta z}{\delta x} / \frac{\delta z}{\delta y} \tag{4.17}$$

Note that

$$Slope = \sqrt{\left(\frac{\delta z}{\delta x}\right)^2 + \left(\frac{\delta z}{\delta y}\right)^2} = \sqrt{\left(\frac{\Delta z_x}{\Delta x}\right)^2 + \left(\frac{\Delta z_y}{\Delta y}\right)^2} \tag{4.18}$$

and the angle of the slope with respect to the horizontal equals the tangent of the slope. With regard to grid data, the resulting slope value assigned to each cell will reflect the overall slope based on the relationship between that cell and its neighbours.

Validation of ASTER DSM

A study was carried out to see if the mean of the square residuals (the value of σ^2 computed as explained in Section 4.2.2) changes significantly according

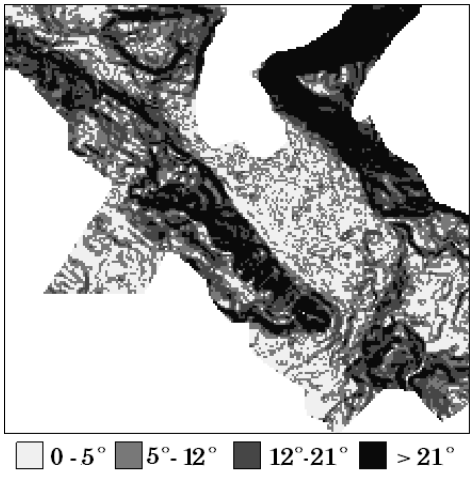

Figure 4.8: Classification based on slope.

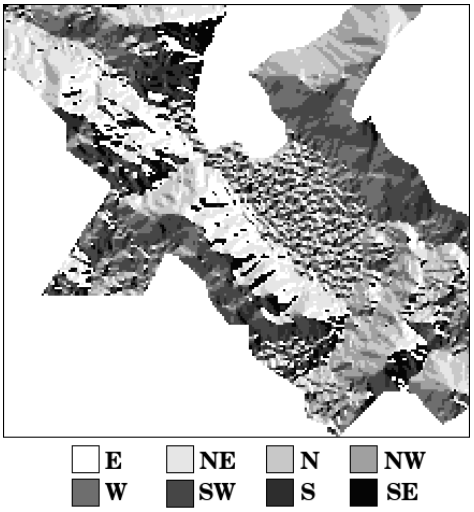

Figure 4.9: Classification based on aspect.

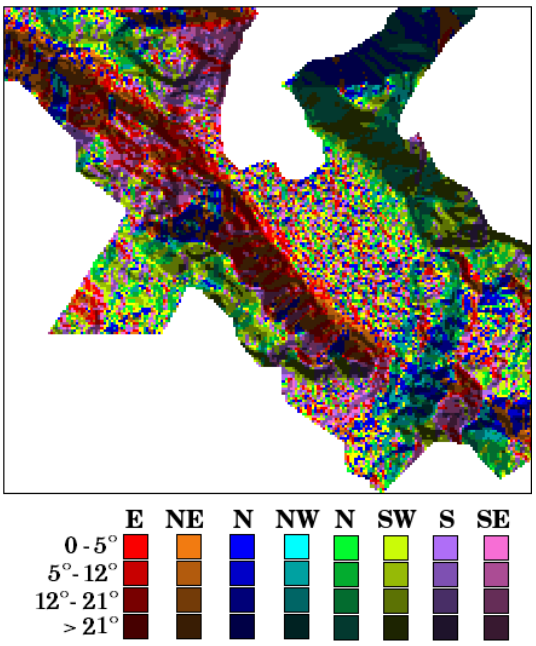

Figure 4.10: ASTER DSM: classification based on slope and aspect.

to the values of slope and aspect of the surface, computed on the model that best approaches the real surface, the LiDAR DSM.
The values of slope and aspect associated to each ASTER node were computed considering the DSM generated with a nearest neighbour interpolation of

LiDAR dataset in the position of ASTER nodes (this is the same grid used for a global validation explained in Section 4.2.2). Practically these calculations were performed using the routine *r.slope.aspect* in GRASS. The data were divided into 4 classes of slope ($0-5°; 5-12°; 12-21°; > 21°$ where $5°, 12°, 21°$ are the values that correspond to $25, 50, 70$ percentile) and 8 classes of aspect (North, North-West, West, South-West, South, South-East, East, North-East) for a total number of 32 classes. Figures 4.8 and 4.9 represent the slope classes and the aspect classes respectively. Figure 4.10 shows the slope and aspect classification map. Class by class the ASTER DSM were compared with the corresponding LiDAR derived DSMs, thus computing a different value of accuracy for each class.

		Aspect							
		N	NW	W	SW	S	SE	E	NE
Slope	$0-5°$	754	732	641	561	657	681	698	764
	$5-12°$	1019	1050	756	659	789	711	705	802
	$12-21°$	833	898	562	597	843	772	634	612
	$> 21°$	796	1022	246	335	722	1033	1018	591

Table 4.6: ASTER: class size.

		Aspect							
		N	NW	W	SW	S	SE	E	NE
Slope	$0-5°$	6.65	7.19	7.18	7.69	7.68	7.95	7.75	7.19
	$5-12°$	8.74	9.10	9.26	10.25	10.55	10.22	10.25	9.46
	$12-21°$	11.39	11.91	12.31	13.28	12.76	11.40	12.40	12.12
	$> 21°$	19.51	20.07	17.60	18.22	16.05	11.76	14.79	16.99

Table 4.7: ASTER: class standard deviation $[m]$.

Parameter	$\mathbf{F_{emp}}$	$\mathbf{F_{theo}}$		**Test results**
		$\alpha = \mathbf{0.01}$	$\alpha = \mathbf{0.05}$	
Slope	172.18	4.87	3.07	Significant dependence
Aspect	4.03	3.64	2.49	Less relevant dependence

Table 4.8: F_{emp} for slope and aspect for ASTER.

The size of each class is reported in Table 4.6 and the slope and aspect dependent accuracies are reported in Table 4.7. The accuracy decreases as the slope increases and changes also with the aspect.
An analysis of variance was done to determine the dependence of σ^2 on slope

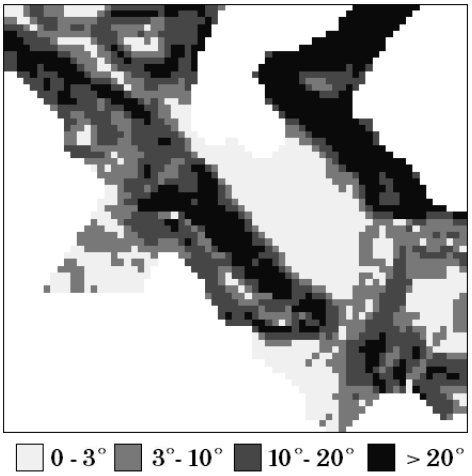

Figure 4.11: Classification based on slope.

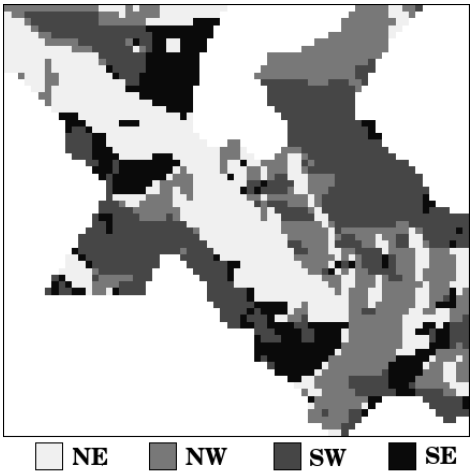

Figure 4.12: Classification based on aspect.

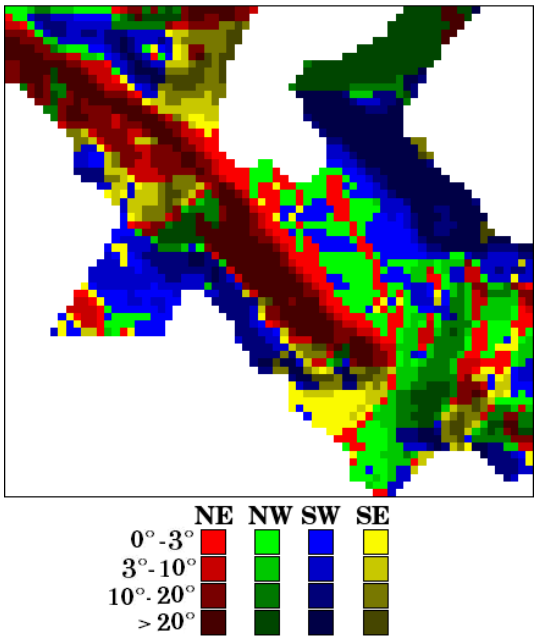

Figure 4.13: SRTM DSM: classification based on slope and aspect.

and aspect values (to have more details on the followed procedure see Sansó [1993] and Lucca [2012]). The test statistic is a Fisher distribution and the hypothesis to test is if the value of sigma doesn't depend on slope/aspect values. Table 4.8 reports the empirical and theoretical values of this statistics. When the empirical value F_{emp} is lower than the theoretical one, the hypothesis is accepted meaning that the value of the variance does not depend on the corresponding parameter. Looking at Table 4.8 it can be observed that there is a significant dependency on slope and a less relevant dependency on aspect.

Validation of SRTM DSM

For SRTM the value of slope and aspect of each node corresponds to the values of slope and aspect calculated for a grid in which each node is the mean value of LiDAR points falling in the cell (as explained in Section 4.2.2). For SRTM 4 classes of slope $(0-3°, 3-10°, 10-20°, > 20°)$ and 4 classes of aspect (North, West, South, East) were consider for a total number of 16 classes. Figure 4.11 and 4.12 represent the classification of SRTM DSM according to slope and aspect respectively. Figure 4.13 shows the slope-aspect classification. In this case, the aspect classes considered were just 4 instead of 8 as for the ASTER case because otherwise the absolute frequencies of each category was too small. The size and accuracy of each class are reported in Table 4.9 and 4.10 respectively. An analysis of variance was done also in this case and Table 4.11 reports the empirical and theoretical values of the statistic, both for the slope and aspect values, for SRTM and ASTER respectively. The results show that with a significance level equal to 0.01 (but also with $alpha = 0.05\%$), the accuracy of the SRTM DSM depends on the surface slope and less on the aspect.

		Aspect			
		N	W	S	E
Slope	$0-3°$	224	176	99	174
	$3-10°$	120	216	99	137
	$10-20°$	121	183	109	199
	$> 20°$	171	218	53	225

Table 4.9: SRTM: class size.

		Aspect			
		N	W	S	E
Slope	$0-3°$	3.06	3.73	4.28	3.00
	$3-10°$	6.93	9.59	6.48	7.52
	$10-20°$	9.72	15.68	8.93	11.51
	$>20°$	14.38	28.63	12.10	19.04

Table 4.10: SRTM: class standard deviation $[m]$.

Parameter	$\mathbf{F_{emp}}$	$\mathbf{F_{theo}}$		**Test results**
		$\alpha = \mathbf{0.01}$	$\alpha = \mathbf{0.05}$	
Slope	23.01	6.99	3.86	Significant dependence
Aspect	6.42	6.99	3.86	Less relevant dependence

Table 4.11: F_{emp} for slope and aspect for SRTM.

4.3 Remarks

An internal validation procedure is necessary to identify those data that have an anomalous behaviour with respect to the model they belong to. When they can be considered as outliers, at a certain level of probability, they should be removed because they could affect the estimated accuracy of the model once compared with a more accurate one.
It was observed that the percentage of suspected and then removed outliers, both in ASTER and in SRTM DSM, was very low (less then 1%). Regarding the validation of the two models using the LiDAR DSM as reference, it can be said that the estimated accuracies were in agreement with ones given by the corresponding DSM producer.
The variance analysis performed allows to conclude that the way the model is able to describe the real surface, as expected, depends on the slope and aspect values of the surface itself. In other words, it can be said that in both cases, ASTER and SRTM DSMs, this dependency exists even it is not so relevant for the aspect factor. This result was exploited during DSMs merging step. Taking into account different weights for cells belonging to different slope-aspect classes in fact allows to obtain a quite significantly improved model, as shown in the following Chapter.

Chapter 5

DEMs fusion within the COSMO-SkyMed project

This Chapter reports a study on the way two different DEMs can be merged together to obtain an improved model. It was developed in view of COSMO-SkyMed products merging when they were not yet available.
Fusion of overlapping DEMs generated from data captured with different techniques or in different times allows to find inconsistencies, to improve density and accuracy, to eliminate gaps. This is the reason why the fusion of digital surfaces, i.e. their optimal combination into a new single dataset, is a crucial topic in the geomatic sciences (Papasaika et al. [2008], Papasaika et al. [2009], Audenino et al. [2001], Schultz et al. [1999], Knöpfle et al. [1998]).
We focused our attention on two DEMs, used as test fields, that, besides having a different grid, represent two different "functionals" of the Earth surface. The heights of the first (ASTER) are point-wise values while those of the second one (SRTM) are averages. A first study was done to see if the information given by the averaged DEM could be improved using the information given by the point-wise one. The fusion was performed making a weighted mean as explained in Section 5.1. A second study was performed to see if the point-wise DEM could be improved using the information given by the averaged DEM. The fusion in this case was implemented via collocation. This part is developed in Section 5.2.

5.1 Improving an average DEM with a point-wise one

Suppose to have two DEMs, one point-wise and the other average, that refer to two grids of different size and shifted one respect to the other. The value

of the height of each cell of the average DEM is indicated as h_m (m stands for mean) while the height for the point-wise DEM is indicated as h_p (p stands for point-wise). Each point h_p has a value of accuracy σ_p associated to it; this value can be the same for all the points h_p if just a variance is considered (for example a global one) or can be different from point to point (suppose to have an error map). A value h_{m2} equal to the weighted average of h_p standing in the window can be associated (Equation 5.1) to each cell of the average DEM (the weight for each observation is the inverse of its variance as some authors suggest, see Papasaika et al. [2008] and Knöpfle et al. [1998]).

$$h_{m2} = \frac{\sum_i \frac{1}{\sigma_{p_i}^2} h_{p_i}}{\sum_i \frac{1}{\sigma_{p_i}^2}} \tag{5.1}$$

The variance of h_{m2}, σ_{m2}^2, can be computed using the variance propagation law as:

$$\sigma_{m2}^2 = \frac{\sum_i \frac{\sigma_{p_i}^2}{\sigma_{p_i}^4}}{\left(\sum_i \frac{1}{\sigma_{p_i}^2}\right)^2} = \frac{1}{\sum_i \frac{1}{\sigma_{p_i}^2}} \tag{5.2}$$

For each cell of the averaged DEM, a new value can be computed as the weighted mean of the two original values, one from the averaged DEM (h_{m1}) and the other from the point-wise one (h_{m2}) :

$$h_{new} = \frac{\frac{1}{\sigma_{m1}^2} h_{m1} + \frac{1}{\sigma_{m2}^2} h_{m2}}{\frac{1}{\sigma_{m1}^2} + \frac{1}{\sigma_{m2}^2}} \tag{5.3}$$

5.1.1 Improving SRTM using ASTER

Following the procedure explained in Section 5.1 a new DEM on the same grid of SRTM was created. This procedure was implemented in different ways:

- considering the nominal accuracy both for the ASTER (10m) and the SRTM DSM (16m) (Section 3.5.3 and 3.5.4);
- considering the accuracy derived from LiDAR comparison both for the ASTER (12.32m) and the SRTM DSM(13.20m)(see Section 4.2.2);
- considering the accuracy derived from slope and aspect classification both for ASTER and SRTM.

The resulting DEMs were compared with the LiDAR dataset, the accuracies are reported in Table 5.1. As expected, in all the cases an improvement was obtained with respect to the initial accuracy of SRTM DSM. Furthermore, the different weighting strategies proved to be effective.

Models (on SRTM grids)	**Accuracy [m]**
SRTM	13.20
Fusion with constant nominal accuracy	11.52
Fusion with accuracy based on LiDAR comparison	11.48
Fusion with accuracy based on slope and aspect classification	10.75

Table 5.1: Accuracy of new DEM obtained with fusion.

5.2 Improving a point-wise DEM with an averaged one

The height field can be consider as a stochastic scalar field on a 2D plain domain; at each location of coordinates x, y the height is a random variable with a certain distribution. Assume that this field has been observed with different techniques and there are observations which can be considered as point-wise values while others evaluations of the height field represent average values. For instance, observations of the field that come from photogrammetry or GPS measurements associate to a point in the position x, y a value of height that refers exactly to that point. On the contrary, when the 3D coordinates of a point have been evaluated using SAR interferometry, the value of height associated to a point P of coordinates x, y, derives from a particular pixel of the SAR image, this value brings in turn in consideration all the echoes of the scatterers that lie in the pixel footprint (see Section 3.2.3).
A study was done to understand if by a statistical method as collocation it is possible to use all the observations, coming from different field functionals, to predict the height of a generic point P located in this field. In Section 5.2.1 the theory is explained while in Section 5.2.2 a case study is presented.

5.2.1 Predicting theory

Suppose to have a scalar field $u(P, \omega)$: at each point P of coordinate x, y belonging to this field a random variable is associated. Suppose to have

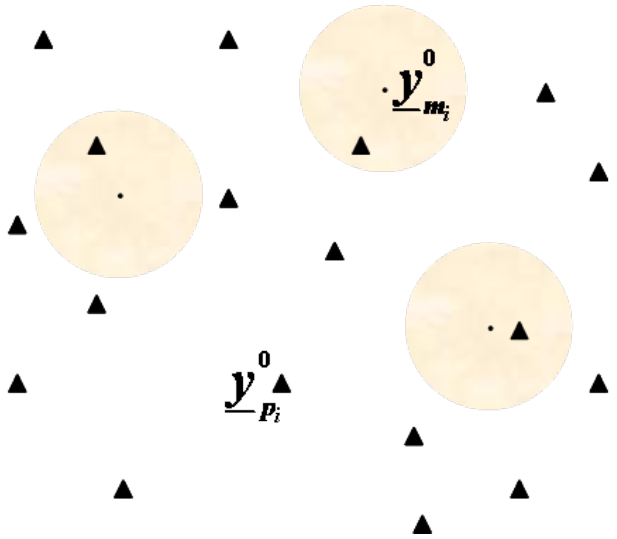

Figure 5.1: Field observations.

different observations of this field coming from different functionals of the field itself. Point-wise observations ($\underline{y}^o_p$) can be considered as the sampled values of the random variables located at different position x, y; they are in the form of a vector of n components:

$$\underline{y}^o_p = \begin{bmatrix} z^o_{p_1} \\ z^o_{p_2} \\ \dots \\ z^o_{p_n} \end{bmatrix} . \tag{5.4}$$

Averaged observations ($\underline{y}^o_m$) can be considered as extractions from the functional that attributes to each point P an average of all the values assumed by the point itself and by its neighbours. It assumes the form of a vector of m rows (m is the number of observations which refers to the average functional of the field and it can be different from the number of point-wise observations).

$$\underline{y}^o_m = \begin{bmatrix} z^o_{m_1} \\ z^o_{m_2} \\ \dots \\ z^o_{m_m} \end{bmatrix} . \tag{5.5}$$

Collocation is applied to compute the coefficients $\underline{\lambda}$ and $\underline{\mu}$ to be used in the linear prediction of the field u in a generic point P

$$\hat{\underline{u}}(P) = \begin{bmatrix} \underline{\lambda}^t & \underline{\mu}^t \end{bmatrix} \begin{bmatrix} \underline{y}^o_p \\ \underline{y}^o_m \end{bmatrix} . \tag{5.6}$$

Each point-wise observation can be considered as the sum of the real value plus an observation noise ν_p:

$$\underline{y}_p^o = \underline{u}\,(z_p) + \underline{\nu}_p. \tag{5.7}$$

Each averaged observation which is the mean of the values of the field in an area A is represented by the integral over the area A of true value of u plus a noise ν_m:

$$\underline{y}_m^o = \frac{1}{A_i} \iint \underline{u}\,(z_i)\; dA_i + \underline{\nu}_m. \tag{5.8}$$

Collocation is a prediction instrument belonging to the Wiener-Kolmogorov estimators and in particular is the predictor that minimizes the mean of square differences between the field u and its linear prediction $\hat{u}$ (see Section 1.4).

$$E\left\{[\underline{u}(P) - \underline{\hat{u}}(P)]^2\right\} = \min_{\underline{\lambda},\underline{\mu}} \tag{5.9}$$

As a first step the square of the difference is evaluated as:

$$\begin{aligned}
&[u\,(P) - \hat{u}\,(P)]^2 = \left[u\,(P) - \underline{\lambda}^t \underline{y}_p^o - \underline{\mu}^t \underline{y}_m^o\right]^2 = \\
&= \left[u\,(P) - \underline{\lambda}^t \left(\underline{u} + \underline{\nu}_p\right) - \underline{\mu}^t \left(\tfrac{1}{A_i} \iint u\,(z_i)\; dA_i + \underline{\nu}_m\right)\right]^2 = \\
&= u\,(P)^2 + \underline{\lambda}^t \underline{u}_p \underline{u}_p^t \underline{\lambda} + \underline{\lambda}^t \underline{\nu}_p \underline{\nu}_p^t \underline{\lambda} + \underline{\mu}^t \underline{\bar{u}}_m \underline{\bar{u}}_m^t \underline{\mu} + \\
&+ \underline{\mu}^t \underline{\nu}_m \underline{\nu}_m^t \underline{\mu} - 2u\,(P)\, \underline{\lambda}^t \underline{u} - 2\underline{u}\,(P)\, \underline{\lambda}^t \underline{\nu}_p + \\
&- 2u\,(P)\, \underline{\mu}^t \underline{\bar{u}}_m - 2u \underline{\mu}^t \underline{\nu}_m + \underline{\lambda}^t \underline{\bar{u}}\,(z_p)\, \underline{\nu}_p + \\
&+ \underline{\lambda}^t \underline{u} \underline{\mu}^t \underline{\bar{u}} + \underline{\lambda}^t \underline{u} \underline{\mu}^t \underline{\nu}_m + \underline{\lambda}^t \underline{\nu}_p \underline{\mu}^t \underline{\bar{u}} + \\
&+ \underline{\lambda}^t \underline{\nu}_p \underline{\mu}^t \underline{\nu}_p + \underline{\mu}^t \underline{\bar{u}} \underline{\mu}^t \underline{\nu}_m
\end{aligned} \tag{5.10}$$

where:

$$\underline{u}_m = \begin{bmatrix} u_m\,(P_1) \\ \vdots \\ u_m\,(P_m) \end{bmatrix} \tag{5.11}$$

with:

$$u_m\,(P_i) = \frac{1}{|A_i|} \iint_{A_i} u\,(x, y)\;\; dx\, dy \tag{5.12}$$

where A_i is the area around P_i where $u(P)$ is averaged and

$$|A_i| = \iint_{A_i} u(x, y)\; dx\, dy \tag{5.13}$$

Before making the mean of function 5.10 some hypothesis should be set; in particular the field is assumed to be homogeneous and isotropic with zero mean (it is a basic hypothesis to apply collocation), the measuring errors ν_p, ν_m are white and uncorrelated with respect to the field u and with respect to each other. In formulas we have:

$$\begin{array}{l} E\left(\underline{u}\right) = 0 \quad \forall P \\ E\left\{\nu_p^2\left(P\right)\right\} = \sigma_{\nu_p}^2 \\ E\left\{\nu_m^2\left(P\right)\right\} = \sigma_{\nu_m}^2 \\ E\left\{\nu_p\left(P\right)\nu_p\left(Q\right)\right\} = 0 \quad \forall P \neq Q \\ E\left\{\nu_m\left(P\right)\nu_m\left(Q\right)\right\} = 0 \quad \forall P \neq Q \\ E\left\{\nu_p\left(P\right)u\left(Q\right)\right\} = 0 \quad \forall P \neq Q \\ E\left\{\nu_m\left(P\right)u\left(Q\right)\right\} = 0 \quad \forall P \neq Q \end{array} \tag{5.14}$$

So the equation $\phi\left(\underline{\lambda}, \underline{\mu}\right)$ that is to minimize becomes:

$$\begin{array}{l} \phi\left(\underline{\lambda}, \underline{\mu}\right) = E\left\{\left[u(P) - \hat{u}(P)\right]^2\right\} = \\ = C_u\left(0\right) + \underline{\lambda}^t C_{pp}\underline{\lambda} + \underline{\lambda}^t C_{\nu_p\nu_p}\underline{\lambda} + \underline{\mu}^t C_{mm}\underline{\mu} + \underline{\mu}^t C_{\nu_m\nu_m}\underline{\mu} + \\ -2\underline{\lambda}^t\underline{C}_p - 2\underline{\mu}^t C_m + 2\underline{\lambda}^t C_{pm}\underline{\mu} \end{array} \tag{5.15}$$

where C_{pm} is

$$C_{pm}\left(P, P'\right) = E\left\{u\left(P\right)u_m\left(P'\right)\right\} \tag{5.16}$$

and C_{mm}

$$\begin{array}{l} C_{mm}\left(P, P'\right) = E\left\{u_m\left(P\right)u_m\left(P'\right)\right\} = \\ E\left\{\frac{1}{|A(P)|}\iint_{A(P)} u\left(Q\right)\ dx_Q\, dy_Q \frac{1}{|A(P')|}\iint_{A(P')} u\left(Q'\right)\ dx_{Q'}\, dy_{Q'}\right\} \end{array} \tag{5.17}$$

To find $\underline{\lambda}$ and $\underline{\mu}$ we compute the differential of the target function with respect to $\underline{\lambda}$ and $\underline{\mu}$, and put it to zero $\forall\underline{\delta\lambda}$ and $\forall\underline{\delta\mu}$:

$$\begin{cases} \frac{\delta\phi\left(\underline{\lambda},\underline{\mu}\right)}{\delta\underline{\lambda}} = 0 \\ \frac{\delta\phi\left(\underline{\lambda},\underline{\mu}\right)}{\delta\underline{\mu}} = 0 \end{cases} \tag{5.18}$$

that is:

$$\begin{cases} 2\underline{\delta\lambda}^t C_{pp}\underline{\lambda} + 2\underline{\delta\lambda}^t C_{\nu_p\nu_p}\underline{\lambda} - 2\underline{\delta\lambda}^t C_p + 2\underline{\delta\lambda}^t C_{pm}\underline{\mu} = 0 \\ 2\underline{\delta\mu}^t C_{mm}\underline{\mu} + 2\underline{\delta\mu}^t C_{\nu_m\nu_m}\underline{\mu} - 2\underline{\delta\mu}^t C_m + 2\underline{\delta\mu}^t C_{pm}\underline{\lambda} = 0 \end{cases} \tag{5.19}$$

from which we have:

$$\begin{cases} C_{pp}\underline{\lambda} + C_{\nu_p\nu_p}\underline{\lambda} - C_p + C_{pm}\underline{\mu} = 0 \\ C_{mm}\underline{\mu} + C_{\nu_m\nu_m}\underline{\mu} - C_m + C_{pm}\underline{\lambda} = 0 \end{cases} \tag{5.20}$$

that written in matrix forms is:

$$\begin{bmatrix} C_{pp} + C_{\nu_p\nu_p} & C_{pm} \\ C_{mp} & C_{mm} + C_{\nu_m\nu_m} \end{bmatrix} \begin{bmatrix} \underline{\lambda} \\ \underline{\mu} \end{bmatrix} = \begin{bmatrix} C_p \\ C_m \end{bmatrix} \tag{5.21}$$

Once the coefficients $\underline{\lambda}$ and $\underline{\mu}$ have been computed by solving the system 5.21, Formula 5.6 can be applied to determine the value of the field ($\hat{u}(P)$) in every prediction points P.
This is the theory behind the prediction of a punctual value using both a point-wise and a average functional. Now the problem is how to implement the calculation of the covariance function between point-wise and average observations (C_{pm}) and between the average observations themselves (C_{mm}). Suppose to know the covariance function of the point-wise field C_{pp} (for example it has been estimated by a certain dataset of point-wise observations). The average observation of the field can be considered as the mean value over an area of radius R of the punctual values of the field. The mean value, theoretically expressed as an integral, can be numerically evaluated for instance as the sum of 24 values around the center of the circular area, each of them multiplied for the proper sector of a circle, divided by the total area A. Obviously the impact of this discretization on the final results of collocation should be studied. This aspect has been not considered in this work but it will be an argument for future developments. Figure 5.2 show the discretization of the area around each averaged observation of the height field.

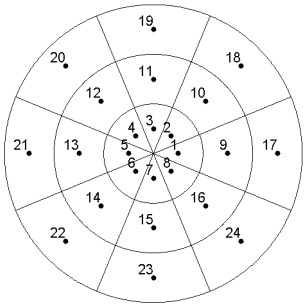

Figure 5.2: Discretization of the area around a mean value.

Considering this discretization of the integral on the area A, the covariance between a punctual observation and a mean observation (C_{pm}) can be considered as:

$$C_{p_i m_j} = \frac{1}{A_j} \sum_{k=1}^{24} A_k C_{p_i p_k} \tag{5.22}$$

and

$$C_{m_i m_j} = \frac{1}{A_i} \frac{1}{A_j} \sum_{k=1}^{24} \sum_{w=1}^{24} A_k A_w C_{p_k p_w}. \tag{5.23}$$

Figure 5.3 and Figure 5.4 can help in understanding the concept expressed by equation 5.22 and 5.23.

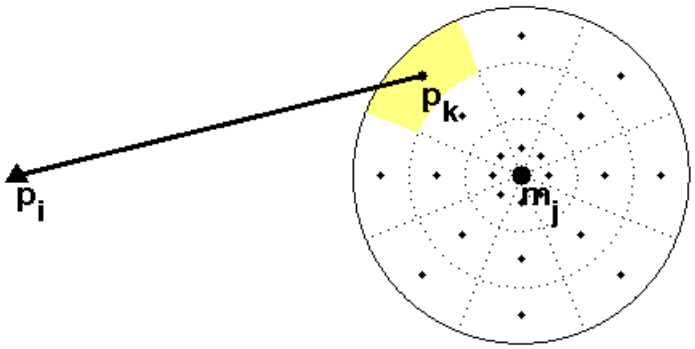

Figure 5.3: $C_{p_i m_j}$.

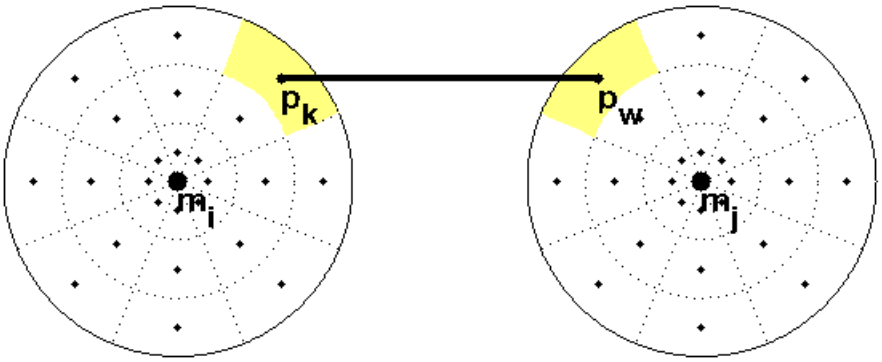

Figure 5.4: $C_{m_i m_j}$.

5.2.2 Case study

Using the method explained in the previous Section 5.2.1, a study was performed to see if SRTM DEM could be improved using ASTER DEM. In order to cover varying terrain characteristics, six study sites with different morphologies were chosen in the area around the lake of Como. The covariance functions of each area were estimated from the ASTER sparse data obtained from preprocessing by using a free software developed by the australian centre for precision agriculture called VESPER (Variogram Estimation and Spatial Prediction plus ERror)(Whelan et al. [2002]). This software allows to analyse relatively quickly large datasets. The program permits to fit the cloud points with different models: spherical, exponential, gaussian, linear with sill, stable, generalised Cauchy, matern, double spherical and double exponential. As a matter of fact we estimated the empirical variogram of the data, thus avoiding the approximated evaluation of their average, interpolated it with a proper model and derived the covariance function, $(C(\tau))$, from the variogram model by exploiting the relation (Eq. 5.24):

$$\gamma_s(\tau) = C_s(0) - C_s(\tau) \tag{5.24}$$

which holds true for homogeneous and isotropic fields. From the covariance function, one can evaluate the correlation length of the height field. This correlation was used to define a window size in order to perform a local collocation prediction. It must be highlighted that the prediction was done using just those observations (both for ASTER and SRTM) that lied in the square window, centred in the prediction point, with side length equal to 2 times the correlation length. More precisely ASTER point-wise observations and SRTM average observations were used to predict both the point-wise value on the position of the ASTER grid and the average value of the field on the position of the SRTM grid. With the prediction a new DEM was obtained and after validated with the LiDAR reference DSM. The procedure was implemented for six different testing sites: two planes, two mountainous areas and two hill areas; their characteristics and the results obtained are illustrated in the following. The study site is an area around the town of Como, Italy, characterized by mountains, hilly regions and flat areas, mainly urban. The method was applied in six different areas with different morphological characteristics since the results can be different according to them (Papasaika et al. [2009]). The six study sites are located as Figure 5.5 shows and the results are reported in the following sections.

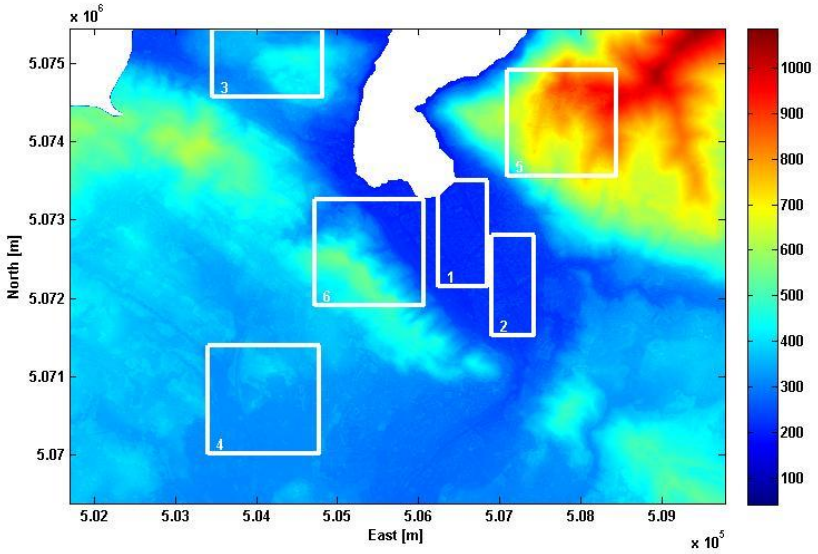

Figure 5.5: Study sites.

Study site # 1

The extension of the area is about 600m along East and 1300m along North. The limit of the region, given in projected coordinates (WGS84, UTM32), are: 506250m W, 506850m E, 5072150m S, 5073500m N. Elevation values ranges between about 245m and 270m as ellipsoidal height.
The empirical variogram is described by an exponential function with equation (Eq. 5.25):

$$y = A\left(1 - e^{-\alpha d}\right) \tag{5.25}$$

and the corresponding covariance function is:

$$y = Ae^{-\alpha d} \tag{5.26}$$

where:

$$\begin{cases} A = 15.75 \\ \alpha = 3.84 \times 10^{-3} \end{cases} \tag{5.27}$$

They are both represented in Figure 5.6.
The RMSE between the points and the interpolated variogram model is equal to 0.8839m^2. The value of the nugget effect, i.e. the variance of the noise can be considered equal to zero ($\sigma^2 = 1 \times 10^{-4}$). To make the prediction, just the observation standing in a window of 2000m centred in the prediction

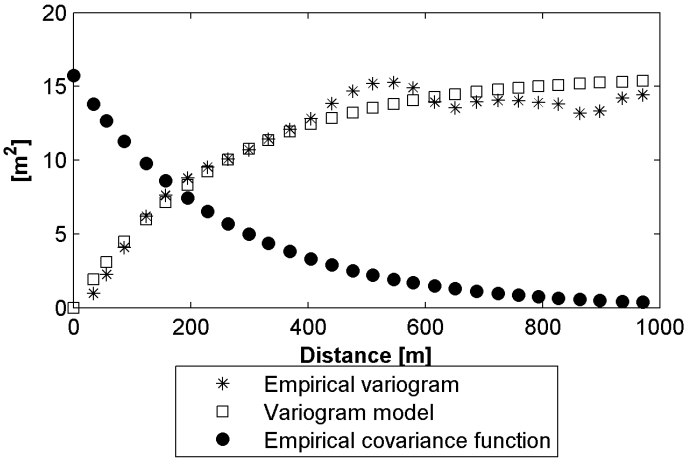

Figure 5.6: Empirical variogram and covariance function in study site # 1.

Number of cells	Interpolation Model	Data used	Accuracy [m]
900	Bilinear	ASTER[1]	7.04
	Collocation	ASTER	9.00
		ASTER & SRTM	6.96

[1] This is the grid obtained as explained in Section 4.2.1

Table 5.2: Accuracy of different DEMs in study site # 1.

point were taken into account.
Figure 5.6 shows the absence of the so called nugget effect; it is reasonable since the nugget represents the variance of the uncorrelated part of the signal. It is linked both to measurements errors and discrepancies in the way the model is reconstructed; since the observations that generate the variogram come from a existing DEM (ASTER DEM in particular), in other words refer to a smoothed surface, it is reasonable that there is no nugget effect since the incoherent part of the signal was already removed.
Table 5.2 summarizes the statistics of the different DEMs with respect to the LiDAR dataset. The RMSE obtained comparing the DEM obtained by bilinear interpolation of ASTER sparse points in this area test and LiDAR DSM is equal to 7.04m^2; this value is lower than 12.32 m calculated for the whole area (see Section 4.2.2) because this area test is mainly flat. Making the gridding using collocation and just ASTER observations, the RSME

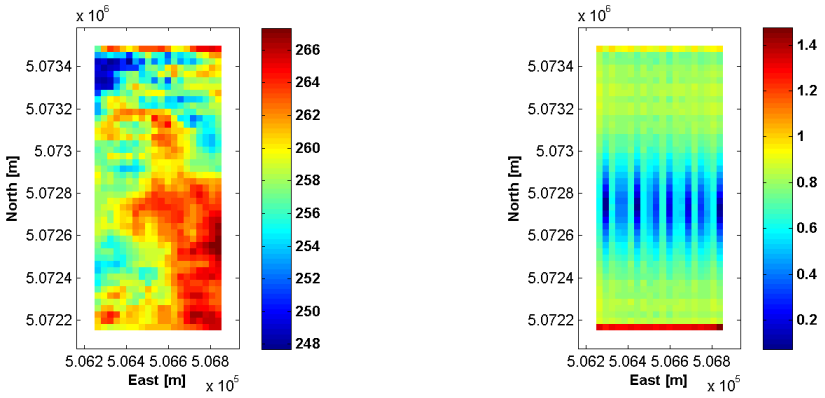

(a) (b)

Figure 5.7: Collocation results in study site # 1 using both ASTER and SRTM observations of the height field. (a) Predicted heights $[m]$; (b) Prediction error variance in $\left[m^2\right]$.

grows a little bit passing from about 7m to 9m; this indicates that in this region bilinear interpolation is preferable to collocation. Nevertheless it can be underlined that when collocation is used to make a gridding on the base of both ASTER and SRTM observation, the resulting DEM has an higher accuracy with respect to the others. This is due to the fact that SRTM has an higher accuracy (2.47m, Table 5.8) with respect to ASTER (see Table 4.7 and 4.10, in particular the first lines regarding lower slopes) and it is able to add information to the model. Figure illustrates 5.7 the new DEM created on the ASTER grid with relative prediction errors applying collocation to ASTER and SRTM observations.

Study site # 2

This area extends about 500 m along East and 1300 m along North. Height values ranges between 260 m and 290 m as ellipsoidal height.
The limit of the region, given in projected coordinates (WGS84, UTM32), are: 506910 m W, 507420 m E, 5071520 m S and 5072810 m N.
The empirical variogram is interpolated by an exponential model of equation (Eq. 5.28):

$$y = A\left(1 - e^{-\alpha d}\right) \tag{5.28}$$

and the corresponding covariance function (eq. 5.29):

$$y = Ae^{-\alpha d} \tag{5.29}$$

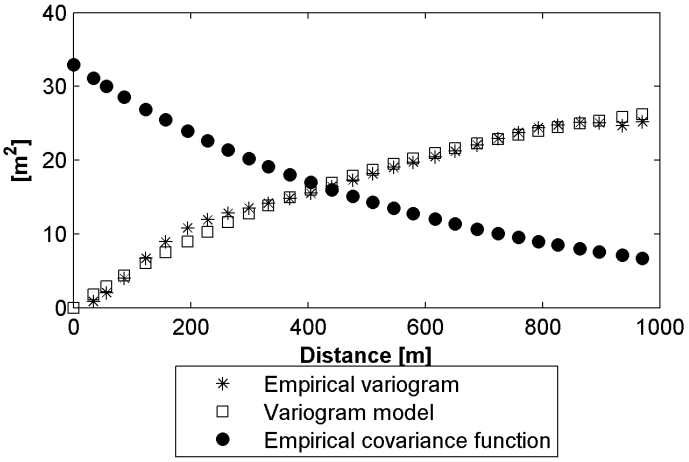

Figure 5.8: Empirical variogram, interpolated variogram model and corresponding covariance function in study site # 2.

Number of cells	**Interpolation Model**	**Data used**	**Accuracy [m]**
731	Bilinear	ASTER	6.77
	Collocation	ASTER	9.99
		ASTER & SRTM	7.35

Table 5.3: Accuracy of different DEMs in study site # 2.

where

$$\begin{cases} A = 32.94 \\ \alpha = 1.6 \times 10^{-3} \end{cases} \tag{5.30}$$

The RMSE between points and interpolated model is equal to 0.8238m^2. The nugget effect is negligible $C_\nu = 1 \times 10^{-4}$. The window size is equal to 2000m. They are both represented in Figure 5.8.

Table 5.3 summarizes the statistics of the different DEMs with respect to the LiDAR dataset. In this case bilinear interpolation allows to create the more accurate DEM; nevertheless the prediction using both ASTER and SRTM observations with collocation permit to obtain a good result (RMSE equal to 7.35 m). Also in this case adding the average observations in the collocation procedure, the accuracy of the final model increases.

In Figure 5.9 the DEM created on the ASTER grid, using collocation from ASTER and SRTM observations, with the relative prediction errors is repre-

sented.

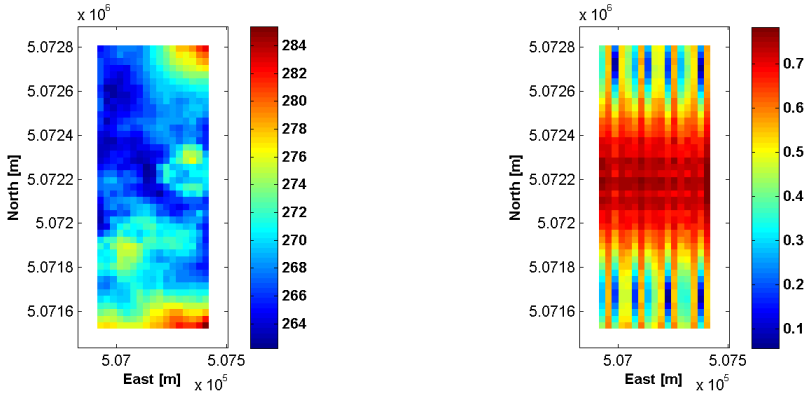

(a) (b)

Figure 5.9: Collocation results in study site # 2 using both ASTER and SRTM observations of the height field. (a) Predicted heights $[m]$; (b) Prediction error variance in $\left[m^2\right]$.

Study site # 3

The area extends about 1300m along East and 1300m along North. The limit of the region, given in projected coordinates (WGS84, UTM32), are: 503460m W, 504810m E, 5074580m S and 5075930m N. Height values ranges between 250m and 500m as ellipsoidal height.

The empirical variogram is interpolated by a gaussian model of equation:

$$y = A(1 - e^{-\alpha d^2}) \tag{5.31}$$

and the corresponding covariance function is:

$$y = Ae^{-\alpha d^2} \tag{5.32}$$

where

$$\begin{cases} A = 4510.5 \\ \alpha = 2.80 \times 10^{-6} \end{cases} \tag{5.33}$$

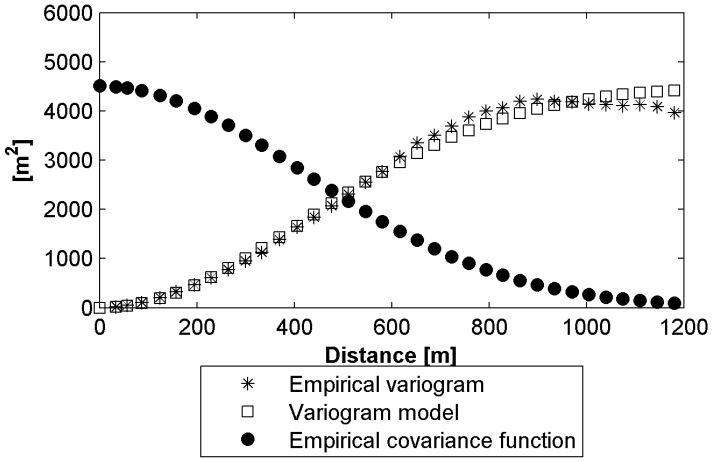

Figure 5.10: Empirical variogram, interpolated variogram model and corresponding covariance model in study site # 3.

Number of cells	**Interpolation Model**	**Data used**	**Accuracy [m]**
2025	Bilinear	ASTER	10.82
	Collocation	ASTER	12.54
		ASTER & SRTM	12.44

Table 5.4: Accuracy of different DEMs in study site # 3.

The RMSE between point and interpolating model is equal to 160.5m^2. The window size is equal to 2400m. The nugget is equal to 3.35 m^2. Empirical variogram, interpolated variogram model and corresponding covariance model are represented in Figure 5.10.

Table 5.4 summarizes the statistics of the different DEMs respect to the LIDAR dataset. The accuracy of DEM obtained from a bilinear interpolation of the ASTER data is higher than in study test #1 and #2; this result is coherent with the classification of ASTER DEM accuracy with respect to slope values (Table 4.7): except for very low slope values, the higher the slope, the lower the accuracy of the ASTER GDEM. Regarding collocation, it can be noted that merging ASTER with SRTM does not permit to increase the accuracy of the generated DEM in a significant way; this is due to the fact that the accuracy of SRTM DSM diminishes when slope increases and the

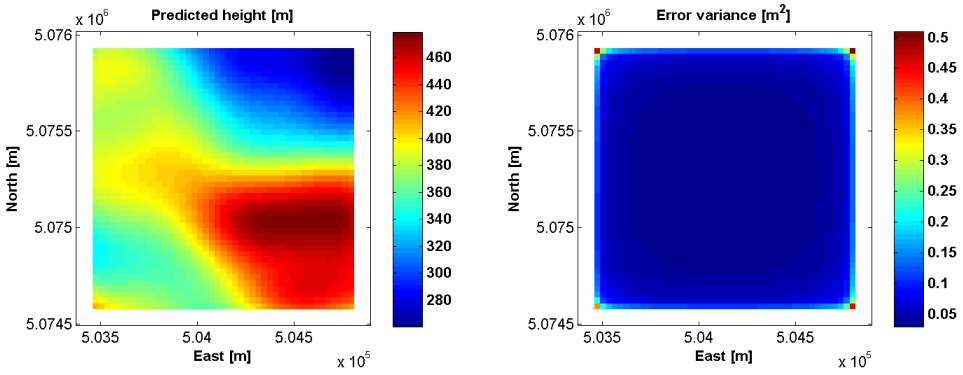

(a) (b)

Figure 5.11: Collocation results in study site # 3 using both ASTER and SRTM observations of the height field. (a) Predicted heights $[m]$; (b) Prediction error variance in $\left[m^2\right]$.

average observations are not able to furnish significant information to the model.
In Figure 5.11 the predicted heights and the errors of prediction in case of collocation using both ASTER and SRTM observations are represented.

Study site # 4

This study site extends about 1350m along North and 1350m along East. The limit of the region, given in projected coordinates (WGS84, UTM32), are: 503400m W, 504780m E, 5070020m S, 5071400m N. Height ranges between 350m and 425m as ellipsoidal height. The empirical variogram is interpolated by a gaussian model of equation

$$y = A(1 - e^{-\alpha d^2}) \tag{5.34}$$

and the corresponding covariance function is

$$y = Ae^{-\alpha d^2} \tag{5.35}$$

where

$$\begin{cases} A = 382.9 \\ \alpha = 2.84 \times 10^{-6} \end{cases} \tag{5.36}$$

as shown in Figure 5.12.

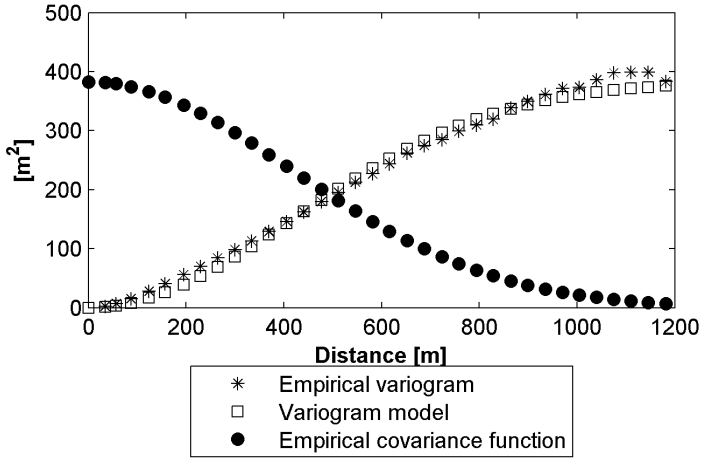

Figure 5.12: Empirical variogram, interpolated variogram model and corresponding covariance model in study site # 4.

Number of cells	**Interpolation Model**	**Data used**	**Accuracy [m]**
2116	Bilinear	ASTER	9.87
	Collocation	ASTER	10.42
		ASTER & SRTM	10.40

Table 5.5: Accuracy of different DEMs in study site # 4.

RMSE between the empirical variogram and the interpolated variogram model is equal to 12.37 m, the nugget effect is equal to 3.888 m^2 and the window size equal to 2400 m.
The comparison here was performed with the DEM from photogrammetry (Section 3.5.2) since LIDAR DSM doesn't cover this area of interest. Table 5.5 reports the accuracy of the generated DEMs. It can be noticed that in this area there is a small difference between the bilinear prediction and collocation. Another element to underline is that there is no significant improvement in merging ASTER and SRTM DSMs; also in this case the averaged observation of the field isn't accurate enough to be able to improve the quality of the resulting DEM.
In Figure 5.13 the predicted heights and the prediction errors using both ASTER and SRTM observations are represented.

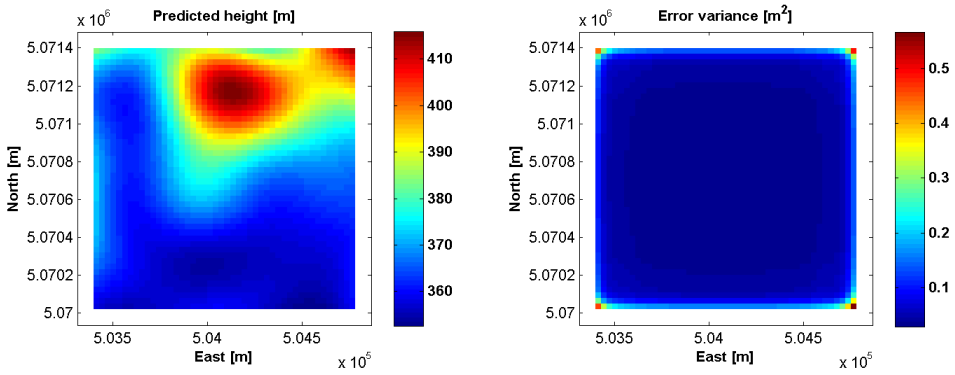

(a) (b)

Figure 5.13: Collocation results in study site # 4 using both ASTER and SRTM observations of the height field. (a) Predicted heights $[m]$; (b) Prediction error variance in $\left[m^2\right]$.

Study site # 5

The area extends about 1300m in East and 1330m along North located as shown in Figure 5.5. The limit of the region, given in projected coordinates (WGS84, UTM32), are: 507090m W, 508440m E, 5073560m S and 5074910m N. Height values ranges between 350m and 1000m as ellipsoidal height.
The empirical variogram in this region was computed using LiDAR data because the empirical variogram of ASTER data were not limited and was not possible to extrapolate the covariance function (Section 1.5.1). The empirical variogram is interpolated by a gaussian model of equation:

$$y = A(1 - e^{-\alpha d^2}) \tag{5.37}$$

and the corresponding covariance function is:

$$y = Ae^{-\alpha d^2} \tag{5.38}$$

where

$$\begin{cases} A = 13537 \\ \alpha = 8.71 \times 10^{-6} \end{cases} \tag{5.39}$$

They are both represented in Figure 5.14.

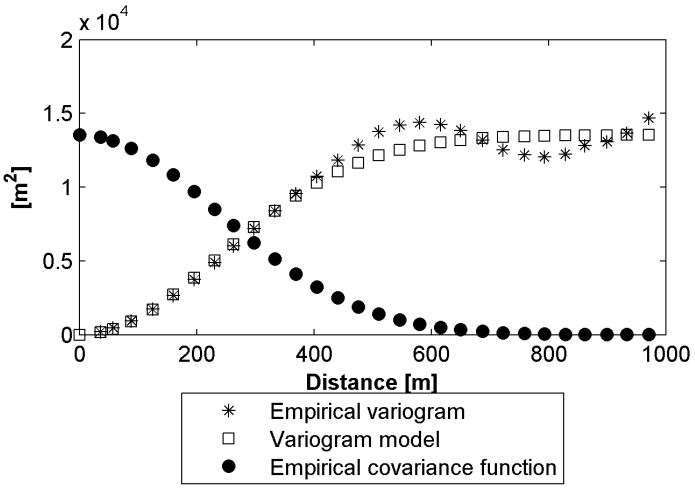

Figure 5.14: Empirical variogram, interpolated variogram model and corresponding covariance model in study site # 5.

Number of cells	**Interpolation Model**	**Data used**	**Accuracy [m]**
2025	Bilinear	ASTER	15.32
	Collocation	ASTER	15.38
		ASTER & SRTM	15.44

Table 5.6: Accuracy of different DEMs in study site # 5.

RMSE between the empirical variogram and the interpolated variogram model is equal to 902.5; the window size is equal to 2000m and the nugget effect is equal to 34.15m^2. Table 5.6 summarizes the statistics of the different DEMs respect to the LIDAR dataset. It can be noticed that in this mountainous area the bilinear interpolation and collocation permit to obtain DEMs with the same level of accuracy. Another result is that, since SRTM DSM describes the Earth surface with a level of accuracy more or less equal to the one of the ASTER DEM, there is no significant difference if collocation is applied only on ASTER observations of the height field or on ASTER and SRTM observations.
In Figure 5.15 the new DEM created on the ASTER grid, using collocation from ASTER and SRTM observations, with the relative prediction errors is represented.

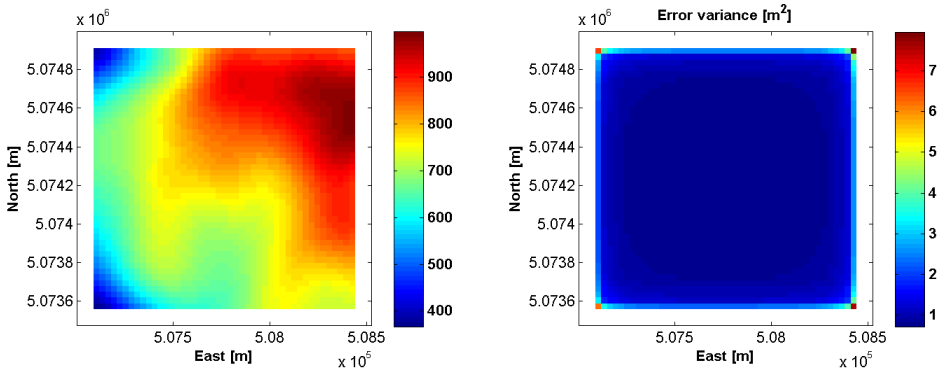

(a) (b)

Figure 5.15: Collocation results in study site # 5 using both ASTER and SRTM observations of the height field. (a) Predicted heights $[m]$; (b) Prediction error variance in $\left[m^2\right]$.

Study site # 6

The area is located as represented in Figure 5.5. The limit of the region, given in projected coordinates (WGS84, UTM32), are: 504720m W, 506070m E, 5071910m S and 5073260m N. It extends about 1330m along North and 1320m along East. Height ranges between 251m and 573m as ellipsoidal heights.
The empirical variogram is interpolated by a gaussian model of equation 5.40

$$y = A(1 - e^{-\alpha d^2}) \tag{5.40}$$

and the corresponding covariance function is:

$$y = Ae^{-\alpha d^2} \tag{5.41}$$

where

$$\begin{cases} A = 20697 \\ \alpha = 1.83 \times 10^{-6} \end{cases} \tag{5.42}$$

as shown in Figure 5.16.

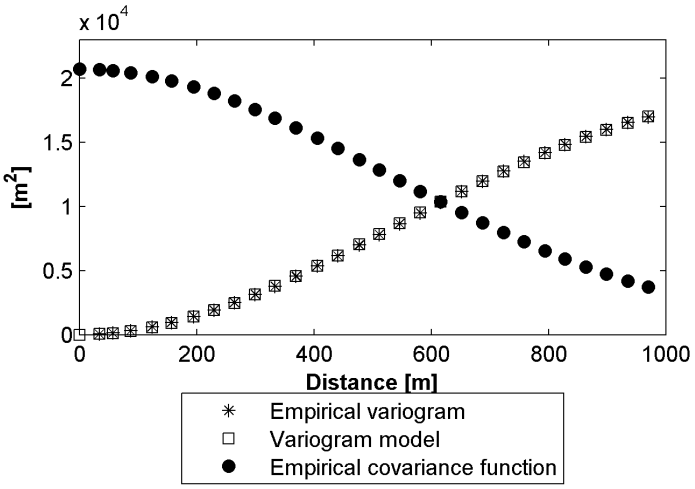

Figure 5.16: Empirical variogram, interpolated variogram model and corresponding covariance function in test site # 6.

Number of cells	Interpolation Model	Data used	Accuracy [m]
2025	Bilinear	ASTER	14.02
	Collocation	ASTER	16.40
		ASTER & SRTM	16.48

Table 5.7: Accuracy of different DEMs in study site # 6.

RMSE between points and the interpolating model is equal to 34.86m^2, the window size equal to 2000 m and the estimated nugget effect equal to 7.55 m^2.
Table 5.7 reports the accuracy of the different DSM on test area # 6. It can be seen that the difference between the collocation prediction considering just ASTER point-wise observations and the one that takes also SRTM observations into account is negligible.
In Figure 5.17 the predicted heights and the errors of prediction in case of collocation using both ASTER and SRTM observations are represented.

5.2.3 Different application of the developed theory

The purpose of the work illustrated in the previous section was to understand if it was possible to improve the accuracy of ASTER DSM through a collocation

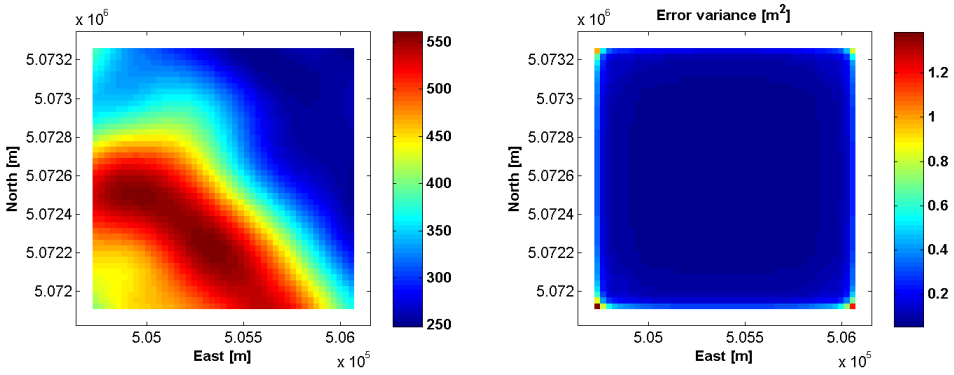

(a) (b)

Figure 5.17: Collocation results in study site # 6 using both ASTER and SRTM observations of the height field. (a) Predicted heights $[m]$; (b) Prediction error variance in $\left[m^2\right]$.

procedure that takes into account also the average observations of the height field. Once this method was developed, it was also applied to understand if it could be used to improve the SRTM DSMs. At the base of this approach there is the same theory explained in Section 5.2.1; the only difference is that in this case the point-wise and the averaged observation of the field are used to predict the average value and not the point-wise value of the height field. Again SRTM observations were considered as the averaged observations of the field while ASTER observations were taken as the point-wise ones.
DEMs obtained merging ASTER and SRTM data on SRTM grids using collocation were compared to the DEMs obtained just using a weighted average of them. The results are reported in Table 5.8. It can be underlined how, for most of the studied cases, the accuracy of these DEMs increases according to the morphology of the terrain. DEMs in plain areas are more accurate than DEM sin hill area which are more accurate than DEMs on mountainous areas; it is coherent with the results found in Section 4.2.3 showing the dependence of ASTER and SRTM DEM accuracy on slope values. It can be seen that for the analysed sites, fusion with collocation permits to reach good results even if the best merging techniques seem to be a fusion just using a weighted average based on slope and aspect classification. Furthermore it is important to say that the collocation method proposed in Section 5.2.1 is very consuming from a computational point of view while

making a weighted average is faster.

	Accuracy [m]					
	Plain		Hill		Mountain	
Model (on the SRTM grid)	**1**	**2**	**3**	**4**	**5**	**6**
SRTM	2.47	2.94	10.42	6.28	19.23	16.30
SRTM prediction using collocation	6.05	5.17	12.20	6.78	18.75	18.98
Fusion by collocation prediction	3.74	3.85	11.34	9.00	13.24	14.49
Weighted average fusion (nominal accuracy)	3.52	2.24	9.20	8.01	11.85	10.15
Weighted average fusion (accuracy from LiDAR)	3.29	2.17	9.07	7.78	11.69	10.06
Weighted average fusion (variable accuracy)	2.10	2.15	8.13	-	10.51	10.08

Table 5.8: Fusion on the SRTM grid.

5.3 Remarks

The generalized collocation procedure here presented needs for sure some refinements.
The weakest point is in the height field empirical function evaluation, due to the assumptions of homogeneity and isotropy which are needed but very often not satisfied.
When this assumption is forced, by not proper interpolations of the estimated empirical values with a given model, this results in high prediction errors. In fact, what the collocation predictor will be able to reconstruct is just the homogeneous and isotropic behaviour of the assumptions. Moreover, this step is always time consuming and quite arbitrary.
Nevertheless, such stochastic predictions are really flexible and allow the merging of average and point-wise models, which becomes a quite challenging issue in this days when SAR avarage DSMs are and will be made available.
Let us disregard for a moment the prediction error introduced by an approximated covariance model, and just compare the results obtained by using the general collocation with the SRTM or ASTER only DSMs predicted with the same technique. We can appreciate in this case the improvement obtained in the final DSMs, either pointwise or average.

A more general remark can be done on the use of stochastic predictors instead of deterministic ones not for DSMs users but for DSMs producers: they seem to us the more suitable for solving problems of optimization involved in DEMs generation especially from different already existent models.
In this respect we would like to investigate further the problem of local predictions based on those techniques, which allow for a more rough definition of the covariance model and a faster and automatic application to DEM generation.

Chapter 6

Validation and fusion of COSMO-SkyMed products

Validation and fusion procedures explained in Chapter 4 and Chapter 5 were thought to be applied to DSMs generated with interferometric techniques. Unfortunately, none of such DSMs were made available to the COSMO-SkyMed project, so that the developed procedures could be applied only partially. The data made available consisted in a set of sparse coordinates computed exploiting radargrammetric principles on COSMO-SkyMed radar stereo-pairs. Our group dealt with the validation of these datasets. As a matter of fact, the importance of the radargrammetric approach is rapidly growing due to the high resolution imagery (up to 1 m Ground Sample Distance GSD) which can be acquired by COSMOSkyMed, TerraSAR-X and RADARSAT-2 sensors in spotlight mode (Capaldo et al. [2011]) and also these new data need to be validated.
Furthermore, a fusion problem was tackled to understand how to merge data coming from ascending and descending stereo-pairs of the same area. This Chapter is organized as follows. Initially there is a short presentation of COSMO-SkyMed mission (Section 6.1). Then, Section 6.2 illustrates the characteristic of the software used to make the elaboration of COSMO-SkyMed images. Section 6.3 describes the characteristics of the available data and Section 6.4 the way they were interpolated. Section 6.5 reports the validation work and Section 6.6 some considerations on the effect of a filtering procedure, based on the coherence values associated to points, to the accuracy of produced DSMs. Section 6.7 analyses the dependence of DSMs accuracy on morphological parameters such as slope and aspect and Section 6.8 is dedicated to the fusion problem.

Orbit type	SSO
Inclination	97.86°
Revolutions/day	14.8125
Orbit Cycle	16 days
Eccentricity	0.00118
Argument of Perigee	90°
Semi Major Axis	7003.52 km
Nominal Height	619.6 km
LTAN	6:00 A.M.
Number of satellites	4
Phasing	90°
Deployment	Progressive

Table 6.1: COSMO Sky-Med orbit charachteristics.

6.1 Cosmo-SkyMed

COSMO-SkyMed (Constellation of small Satellites for Mediterranean basin Observation) is an Earth Observation System commissioned and funded by the Italian space Agency (ASI) and Italian Ministry of Defense (MoD). The system consists of a constellation of four Low Earth Orbit mid-sized satellites, each equipped with a multi-mode high-resolution Synthetic Aperture Radar (SAR) operating at X-band and fitted with particularly flexible and innovative data acquisition and transmission equipment. Some high level performances of this system are:

- large amount of daily acquired images;
- satellite worldwide accessibility;
- all weather and day/night acquisition capabilities;
- very fast interval between the finalization of the user request for the acquisition of a certain geographic area and the release of the remote sensing products;
- very fine image quality (i.e. high spatial and radiometric resolution);
- possibility to chose between wide images with low spatial resolution and more reduced coverage but with sub-meter resolution.

Table 6.1 reports the orbit characteristics of the constellation.
The SAR sensors mounted on-board are multimode sensors operating in:

- spotlight mode, for metric resolutions over small images (10km × 10km);
- two stripmap modes, for metric resolutions (from 3m to 5m) over tenth of km images; one mode is polarimetric with images acquired in two polarizations;
- two ScanSAR for medium to coarse (from 30m to 100m) resolution over large swath (200km).

Figure 6.1 shows the three acquisition modes of the COSMO-SkyMed sensor.

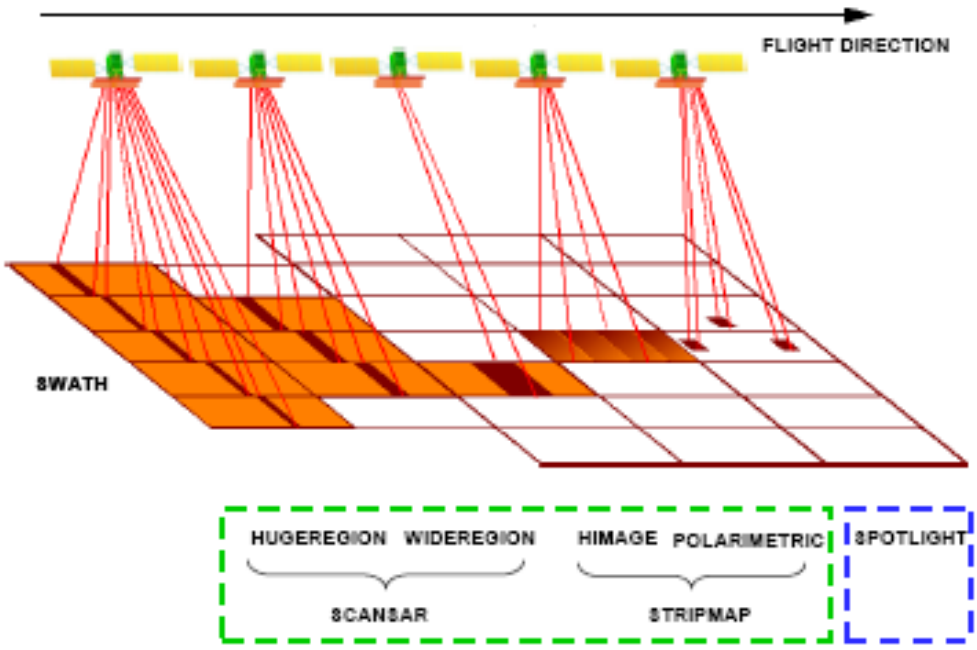

Figure 6.1: The 3 acquisition modes of COSMO-SkyMed sensor.

6.2 Elaboration of raw data

Point coordinates were extracted appling the radargrammetric approach (3.2.3) to COSMO Sky-Med stereo pairs acquired in SpotLight mode. All products used belong to the level 1A SCS category products (Single look, Complex, Slant range) which are focused data in slant range zero Doppler projection (the target is acquired on a heading that is perpendicular to the flying direction of satellite). The software used to elaborate these images is called SISAR (*Software per immagini satellitari ad Alta Risoluzione*) which

is a scientific software developed at the Geodesy and Geomatic Institute of the University of Rome "La Sapienza".
DSM generation using radargrammetric techniques consists of two basic steps: the stereo pair orientation and the image matching. Software SISAR permits the image orientation of SAR stereo pairs in zero-Doppler geometry: this is done using both rigorous (or physically based) model and the Rational Polynomial Functions (RPFs) model. The last one consists of purely analytical functions linking image to terrain coordinates, independently of specific platform, sensor characteristics and acquisition geometry. It performs a 3D orientation based on two range and two zero-Doppler equations allowing for the least squares estimation of some calibration parameters, related to satellite position, satellite velocity and to the range measure using a set of GCP (Ground Control Points). As for the image matching, the critical issue is the definition of a strategy to search the homologous points in the two images; in the SISAR software a matching procedure has been developed based on a coarse-to-fine hierarchical solution with an effective combination of geometrical constraints and an Area Base Matching (ABM) algorithm (Crespi et al. [2010]).

6.3 Data Description

Data to be validated were extracted using two stereopairs (one ascending and the other descending) of COSMO-SkyMed images acquired in SpotLight modality and in zero-Doppler/slant-range geometry. Table 6.2 reports the characteristic of these stereo pairs.

Area	**Acquisition time**	**Coverage [km²]**	**Mean incidence angle (deg)**	**Orbit**	**Look side**	**B/H**
Como	June 24^{th} 2011	10 × 10	27.8	Desc	Right	0.8
	June 28^{th} 2011	10 × 10	55.4	Desc	Right	0.8
	June 17^{th} 2011	10 × 10	50.8	Asc	Right	0.6
	August 7^{th} 2011	10 × 10	28.9	Asc	Right	0.6

Table 6.2: Image acquisition modality description.

Data refer to two different areas located near the city of Como as shown in Figure 6.2.

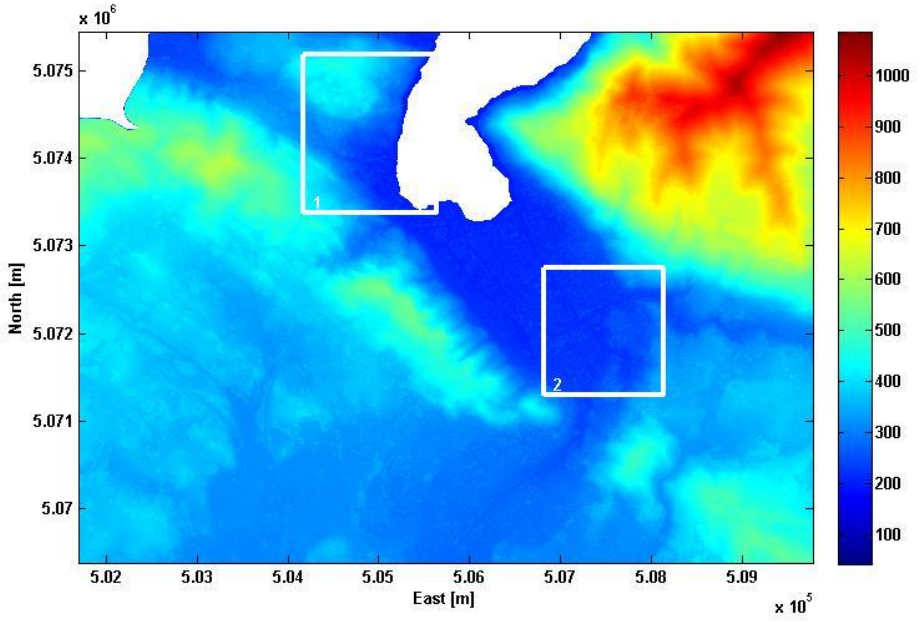

Figure 6.2: Study sites.

Geographic limits of Region 1, given in projected coordinates (UTM32, WGS84), are: 504165m W, 505635m E, 5073375m S and 5075180m N. Geographic limit of region 2, given in projected coordinates (UTM32, WGS84), are: 506825m W, 508145m E, 5071295m S and 5072745m N. For each region there are two datasets of point coordinates, one extracted from the ascending stereopair and one from the descending stereo pair. Figures 6.3 and 6.4 show the distribution of those points while Tables 6.3 and 6.4 report some statistics of the different datasets. Furthermore, to each point is associated a value of coherence that is the cross-correlation between homologous points evaluated during the image-matching phase. Theoretically, the value of coherence ranges from 0 to 1 (maximum correlation) but coordinates are rendered just for those couple of points with a cross-correlation value higher than 0.75. This parameter can be considered as a reliability index of the height information associated to a terrain object obtained from a couple of homologous points.

6.4 Interpolation

Data were interpolated using bilinear splines on a grid of 5 m $\times$ 5 m. This value of resolution was suggested from the research group that elaborated SAR images and it is consistent with the average density of data. Radar points

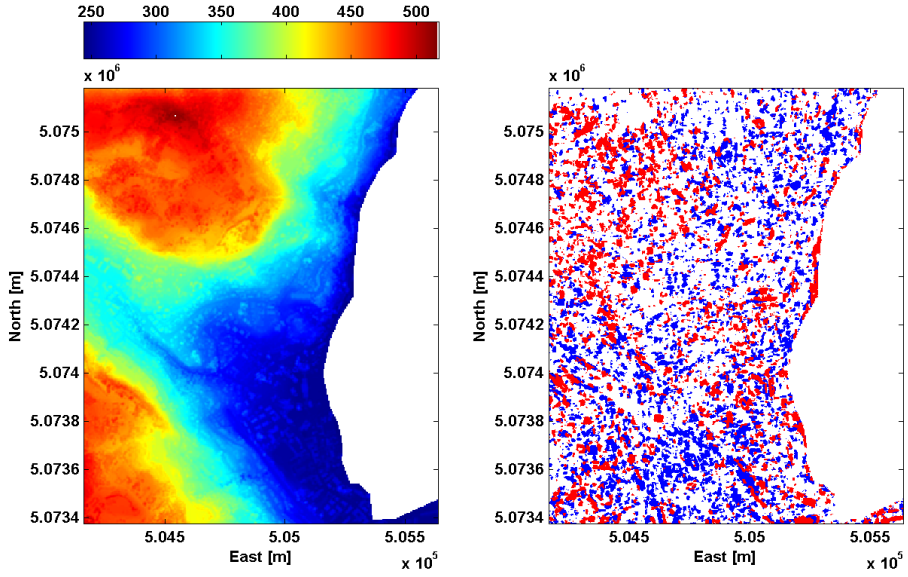

Figure 6.3: Region 1 and distribution of SAR points (in blu the points extracted from the ascending stereo pair).

		East [m]	North [m]	Height [m]
230004 Ascending points	min	504165.00	5073375.00	204.02
	max	505634.86	5075179.99	498.56
	mean	504768.03	5074163.73	360.99
	std	337.37	542.87	74.72
132287 Descending points	min	504165.00	5073375.00	215.77
	max	505634.96	5075179.94	498.54
	mean	504692.53	5074281.47	373.78
	std	361.35	526.22	82.88

Table 6.3: Region 1: Point statistics.

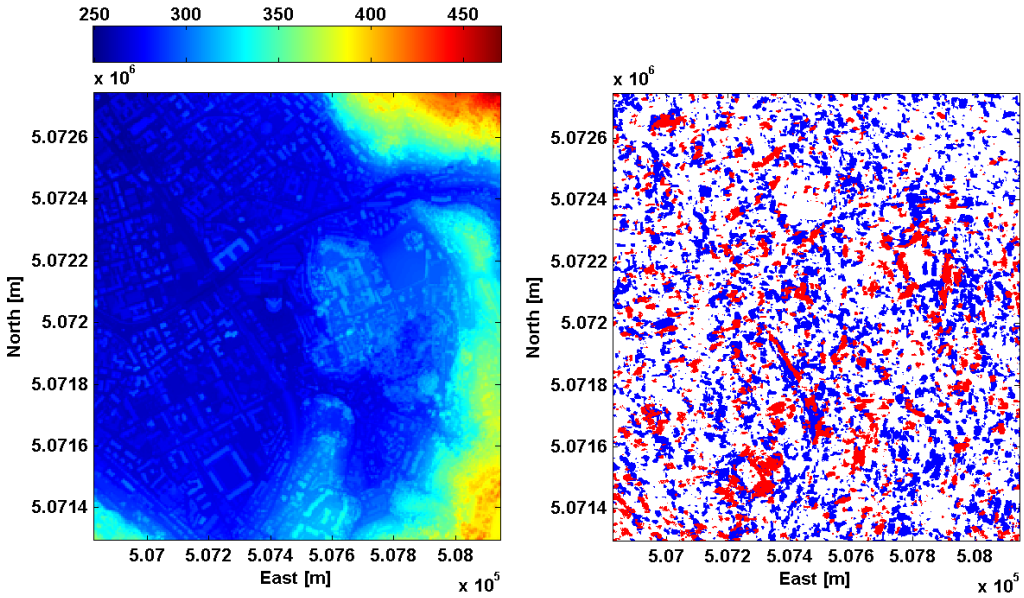

Figure 6.4: Region 2 and distribution of SAR points (in blu the points from ascending orbit).

		East [m]	North [m]	Height [m]
251341 Ascending points	min	506825.00	5071295.01	215.72
	max	508144.99	5072744.99	452.49
	mean	507495.80	5071995.73	291.62
	std	366.99	408.54	40.26
89668 Descending Points	min	506825.00	5071295.06	211.39
	max	508145.00	5072745.00	404.60
	mean	507449.69	5071948.46	288.39
	std	364.33	388.68	26.76

Table 6.4: Region 2: Point statistics.

located on the lake surface were not considered for interpolation because they were related to bugs in the image matching programme.
Figure from 6.5 to 6.6 show the interpolated DSM from ascending (DSM_A), descending (DSM_D) and ascending plus descending (DSM_{AD}) points for Region 1 and Region 2 respectively.

6.5 Validation

Firstly, an internal validation of generated DSMs was performed following the methodology explained in Section 4.1 that allows to identify and remove possible outliers. The parameters set to make this validation were:

- Window size: 3×3 pixels;
- Interpolation method: bilinear;
- Significance level (α): 0.0002.

Tables 6.5 and 6.6 summarize the results obtained considering the following input parameters. It can be noticed that the percentage of outliers is very low; this means that most of the cells give an information on the height field that is statistically coherent with the one given by the neighbouring cells.

Model	**# of cells**	**# of outlier**	**%**
DSM_A	82324	14	0.017
DSM_D	82324	19	0.023
DSM_{AD}	82324	30	0.036

Table 6.5: Region 1. Results of internal validation.

Model	**# of cells**	**# of outlier**	**%**
DSM_A	76560	14	0.031
DSM_D	76560	19	0.013
DSM_{AD}	76560	36	0.047

Table 6.6: Region 2. Results of internal validation.

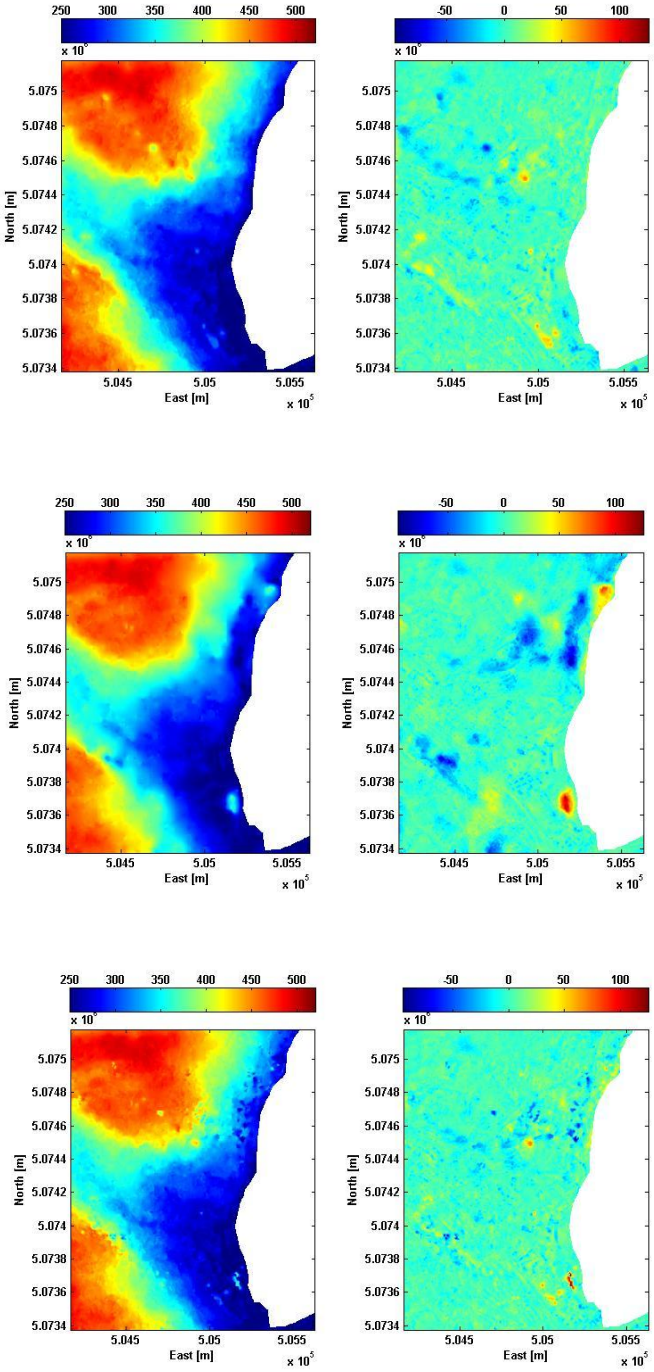

Figure 6.5: Region 1. Top: (left) DSM_A, (right) $DSM_A - DSM_{LiDAR}$; Center: (left) DSM_D, (right) $DSM_D - DSM_{LiDAR}$; Bottom: (left) DSM_{AD}, (right) $DSM_{AD} - DSM_{LiDAR}$.

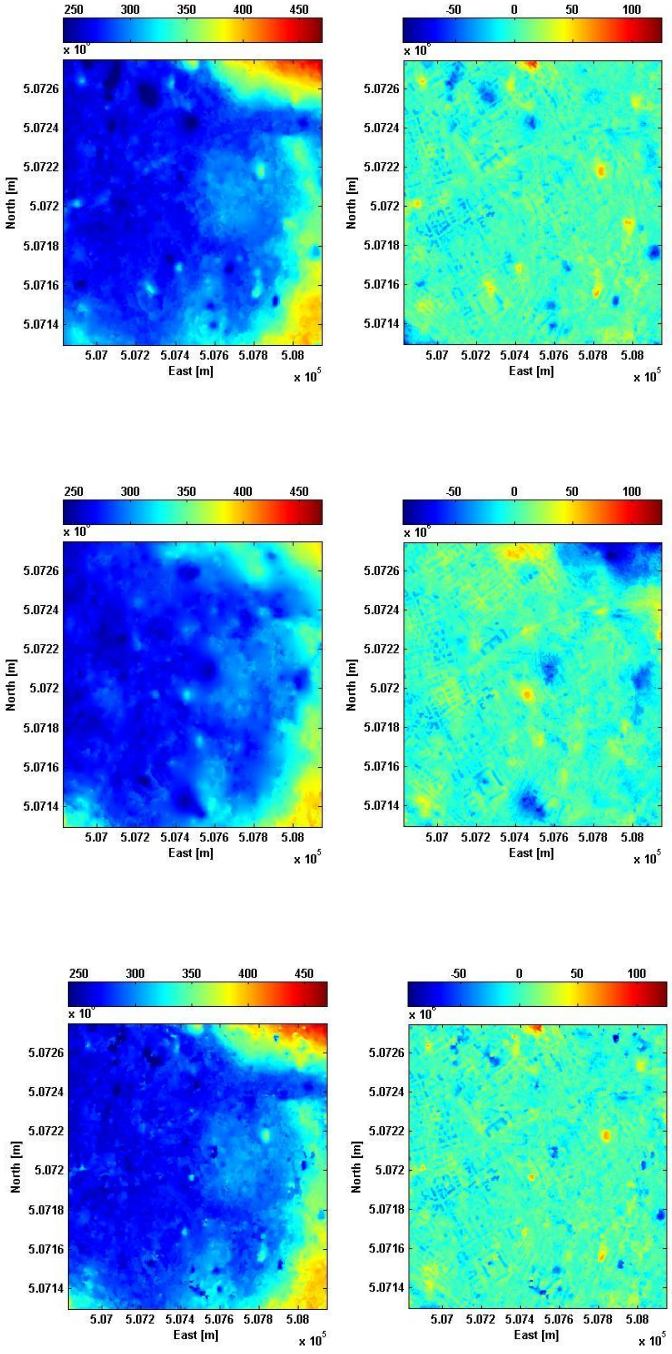

Figure 6.6: Region 2. Top: (left) DSM_A, (right) $DSM_A - DSM_{LiDAR}$; Center: (left) DSM_D, (right) $DSM_D - DSM_{LiDAR}$; Bottom: (left) DSM_{AD}, (right) $DSM_{AD} - DSM_{LiDAR}$.

Subsequently, to find the accuracy of the generated DMSs, they were compared with the LiDAR dataset, more precisely to the LiDAR DSM with resolution equal to 5m, obtained by sub-sampling a LiDAR DSM with resolution equal to 2.5m (in the following indicated as R1LB5 and R2LB5). The LiDAR DSM was the most accurate available DSM and surely with an accuracy of an order of magnitude higher than that of radargrammetric products, which was expected to be in the order of 10m. The global accuracy of the six DSMs produced with the whole dataset (coherence greater that 0.75) is reported in Table 6.7 for Region 1 and in Table 6.8 for Region 2. The statistics were evaluated on the 95% of the whole population; the threshold for the rejection (LE95) is indicated in the last column of Tables 6.7, 6.8.

Model	**Number of cells**	**RMSE [m]**	**sigma [m]**	**bias [m]**	**LE95**
DSM_A	82324	7.56	7.39	-1.61	20.24
DSM_D	82324	9.64	9.61	0.82	30.34
DSM_{AD}	82324	7.24	7.08	-1.51	19.72

Table 6.7: Region 1: Bilinear interpolated DSMs accuracy.

Model	**Number of cells**	**RMSE [m]**	**sigma [m]**	**bias [m]**	**LE95**
DSM_A	76560	8.70	8.58	-1.47	23.88
DSM_D	76560	11.54	11.52	0.68	33.08
DSM_{AD}	76560	8.70	8.60	-1.31	22.76

Table 6.8: Region 2: Bilinear interpolated DSMs accuracy.

Analysing Tables 6.7 and 6.8 some considerations can be done. Estimated accuracies are higher for the DSMs generated using the points obtained from the ascending stereo-pair. This could be due both to the fact that descending images were more affected by problems related to foreshortening and to the fact that the number of points used for the interpolation is lower. The use of both ascending and descending data results in a DSM whose accuracy is not significantly different from that of the ascending one.

6.6 Filtering on coherence value

Some analysis was performed considering also the value of coherence associated to each point; it was conducted to see if the accuracy of the final DSM could depend on the coherence of points used for interpolation. For each region, three DSMs were obtained with a bilinear spline interpolation of just those points with an accuracy higher than 0.85. Figures 6.7 and 6.8 illustrate those DSMs and the difference with the corresponding reference DSM. The global accuracies of the six DSMs are reported in Tables 6.9 and 6.10 for Region 1 and Region 2 respectively. The statistics were evaluated on the 95% of the whole population; the threshold for the rejection is indicated in the last column of Tables 6.9 and 6.10. Comparing Tables 6.9 and 6.10 with Tables 6.7 and 6.8, it can be noticed that the use of higher coherent points is worthy as the generated DSMs accuracies increase of half a meter or more.

Model	**Numbers of cells**	**RMSE [m]**	**sigma [m]**	**bias [m]**	**LE95**
DSM_A	82324	7.37	7.22	-1.44	18.90
DSM_D	82324	9.20	9.14	1.01	22.04
DSM_{AD}	82324	6.77	6.33	-1.39	17.37

Table 6.9: Region 1: Bilinear interpolated $DSMs$ accuracy (coherence > 0.85).

Model	**Numbers of cells**	**RMSE [m]**	**sigma [m]**	**bias [m]**	**LE95**
DSM_A	76560	8.10	7.91	-1.73	21.30
DSM_D	76560	11.08	11.06	-0.65	33.20
DSM_{AD}	76560	7.98	7.81	-1.63	22.19

Table 6.10: Region 2: Bilinear interpolated $DSMs$ accuracy (coherence > 0.85).

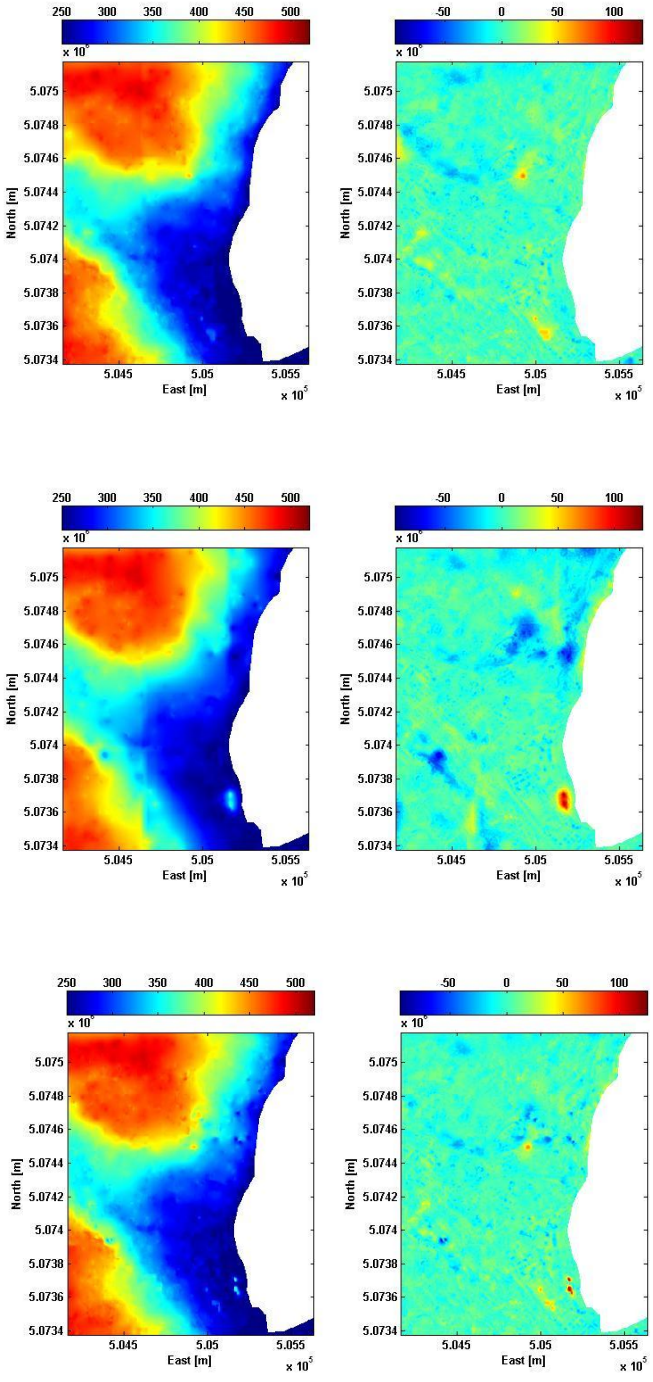

Figure 6.7: Region 1 (coherence > 0.85). Top: (left) DSM_A, (right) $DSM_A - DSM_{LiDAR}$; Center: (left) DSM_D, (right) $DSM_D - DSM_{LiDAR}$; Bottom: (left) DSM_{AD}, (right) $DSM_{AD} - DSM_{LiDAR}$.

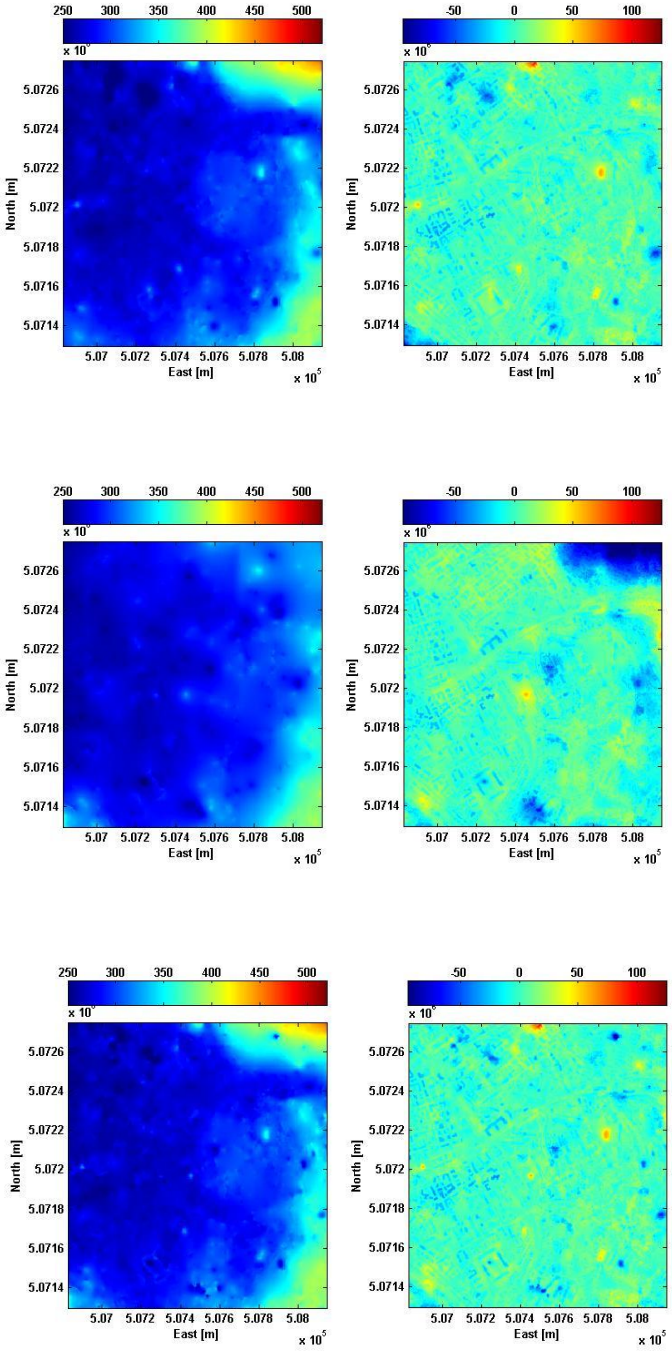

Figure 6.8: Region 2: coherence > 0.85. Top: (left) DSM_A, (right) $DSM_A - DSM_{LiDAR}$; Center: (left) DSM_D, (right) $DSM_D - DSM_{LiDAR}$; Bottom: (left) DSM_{AD}, (right) $DSM_{AD} - DSM_{LiDAR}$.

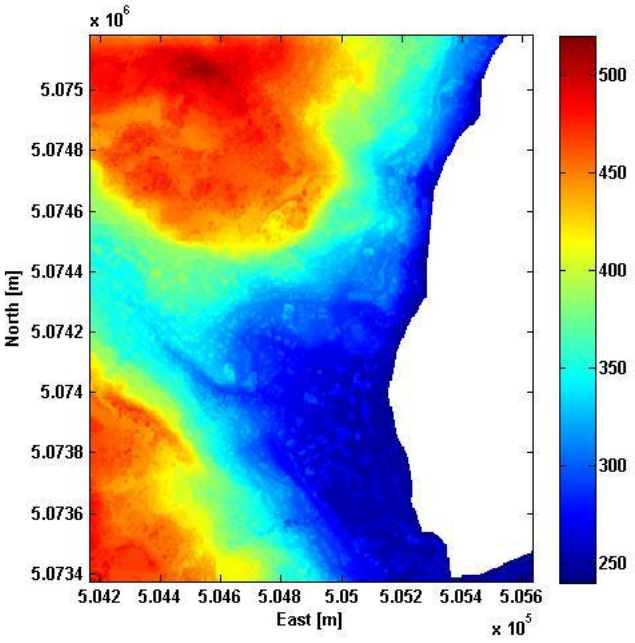

Figure 6.9: The LiDAR derived 5m × 5m resolution model (R1LB5).

6.7 Slope and aspect classification

6.7.1 Region 1

As in the case of ASTER and SRTM (Section 4.2.3) the LiDAR derived model in Region 1 (R1LB5) was used for a morphology dependent accuracy estimate (Figure 6.9 shows the reference DSM). Figure 6.10 and Figure 6.11 illustrate the surface of region 1 classified by slope only, by aspect only and by slope and aspect together. Classes of accuracy were formed according to 4 classes of slope (the limits between the different classes, 15°, 27°, 40° corresponds to the 25^{th}, 50^{th} and 75^{th} percentile of the dataset) and 8 classes of aspect (North, North-East, East, South-East, South, South-West, West, North-West). Table 6.11 reports the class size of the slope-aspect classification.

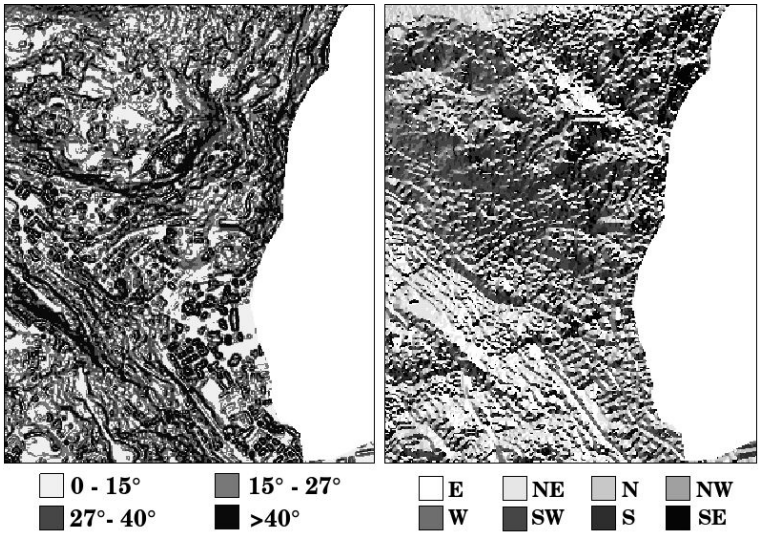

Figure 6.10: Region 1: classification based on slope (left) and on aspect (right).

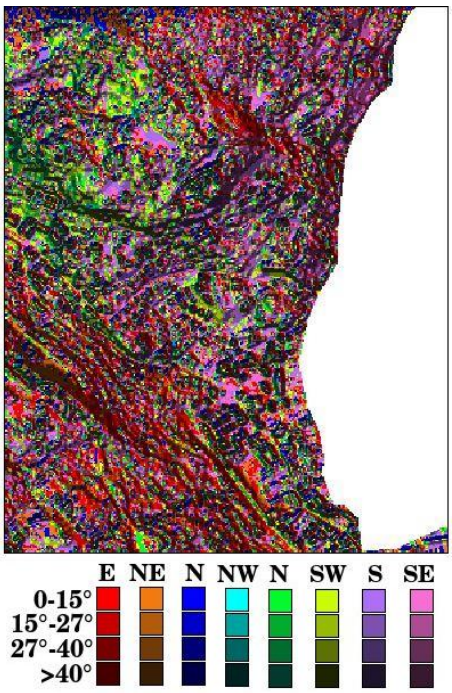

Figure 6.11: Region 1: classification based on slope and on aspect.

		Aspect							
		N	NW	W	SW	S	SE	E	NE
Slope	$0 - 15°$	1759	1566	1845	2387	2940	3044	2827	2338
	$15 - 27°$	1779	1467	1794	2632	3357	3665	3550	2533
	$27 - 40°$	1759	1318	1629	2518	3387	3835	3934	2718
	$> 40°$	1448	1082	1420	2348	2999	3678	3982	2853

Table 6.11: Region 1: class size.

		Aspect							
		N	NW	W	SW	S	SE	E	NE
Slope	$0 - 15°$	10.00	9.62	9.48	8.72	8.99	9.11	9.66	10.07
	$15 - 27°$	9.39	9.21	9.61	9.53	9.83	9.35	8.53	9.15
	$27 - 40°$	9.08	9.05	10.39	9.98	10.30	9.52	8.46	9.12
	$> 40°$	10.84	10.42	11.65	11.62	11.25	9.86	9.54	11.46

Table 6.12: Region 1: DSM_A accuracy [m].

Model	**Parameter**	$\mathbf{F_{emp}}$	$\mathbf{F_{theo}}$	
			$\alpha = \mathbf{0.01}$	$\alpha = \mathbf{0.05}$
DSM_A	slope	35.16	4.87	3.07
	aspect	17.58	3.64	2.49

Table 6.13: Region 1: analysis of variance results for DSM_A.

Analysis of variance for DSMs generated using all the dataset

Tables 6.12, 6.14 and 6.16 show the value of variance in each slope and aspect class for the three DSMs of Region 1. It can be observed that for all the classes the DSM obtained from the ascending stereo-pairs performs better than that from the descending one. For each DSM the analysis of variance results are also reported (Tables 6.13, 6.15 and 6.17). If the empirical value is higher than the theoretical one, it means that there is a dependence with respect to the parameter. It can be seen that for all analysed DSMs there is a relevant dependence on both the morphological parameters.

		Aspect							
		N	NW	W	SW	S	SE	E	NE
Slope	$0-15°$	13.37	14.47	12.50	11.39	11.32	11.74	11.83	10.72
	$15-27°$	13.11	15.51	13.18	11.64	12.74	14.81	14.00	13.33
	$27-40°$	12.44	15.11	13.87	12.08	14.64	16.57	15.61	14.25
	$>40°$	11.56	12.21	15.01	11.75	16.27	19.58	18.20	15.21

Table 6.14: Region 1: DSM_D accuracy [m].

Model	**Parameter**	$\mathbf{F_{emp}}$	$\mathbf{F_{theo}}$	
			$\alpha = \mathbf{0.01}$	$\alpha = \mathbf{0.05}$
DSM_D	slope	26.29	4.87	3.07
	aspect	22.16	3.64	2.49

Table 6.15: Region 1: analysis of variance results for DSM_D.

		ASPECT							
		N	NW	W	SW	S	SE	E	NE
SLOPE	$0-15°$	9.98	10.77	9.51	8.76	8.34	9.18	9.92	8.95
	$15-27°$	9.43	10.39	9.37	9.19	10.16	9.69	9.14	9.40
	$27-40°$	8.98	9.47	10.85	9.44	10.37	10.21	9.56	9.34
	$>40°$	10.05	9.92	11.55	10.51	11.96	11.45	10.73	10.72

Table 6.16: Region 1: DSM_{AD} accuracy [m].

Model	**Parameter**	$\mathbf{F_{emp}}$	$\mathbf{F_{theo}}$	
			$\alpha = \mathbf{0.01}$	$\alpha = \mathbf{0.05}$
DSM_{AD}	slope	38.43	4.87	3.07
	aspect	8.80	3.64	2.49

Table 6.17: Region 1: analysis of variance results for DSM_{AD}.

Analysis of variance for DSMs generated using just those points with a coherence higher than 0.85

		Aspect							
		N	NW	W	SW	S	SE	E	NE
Slope	$0-15°$	9.90	9.26	9.29	8.98	8.64	8.99	9.56	9.92
	$15-27°$	9.58	9.05	9.38	9.08	9.25	9.05	8.40	9.22
	$27-40°$	8.96	9.08	10.35	9.64	9.47	9.03	7.90	9.06
	$>40°$	9.92	9.28	10.29	10.49	10.07	9.28	8.41	10.38

Table 6.18: Region 1: DSM_A accuracy [m] (coherence>0.85).

Model	**Parameter**	$\mathbf{F_{emp}}$	$\mathbf{F_{theo}}$	
			$\alpha = \mathbf{0.01}$	$\alpha = \mathbf{0.05}$
DSM_A	slope	8.74	4.87	3.07
	aspect	23.01	3.64	2.49

Table 6.19: Region 1: analysis of variance results for DSM_A (coherence>0.85).

		Aspect							
		N	NW	W	SW	S	SE	E	NE
Slope	$0-15°$	12.38	13.68	11.48	10.35	10.08	10.63	10.93	9.93
	$15-27°$	12.75	14.24	12.14	10.74	11.54	13.13	12.95	12.58
	$27-40°$	11.92	14.33	13.07	11.31	13.13	13.53	13.65	13.08
	$>40°$	11.48	11.21	14.07	11.31	14.33	15.97	15.04	14.09

Table 6.20: Region 1: DSM_D accuracy [m] (coherence>0.85).

Model	**Parameter**	$\mathbf{F_{emp}}$	$\mathbf{F_{theo}}$	
			$\alpha = \mathbf{0.01}$	$\alpha = \mathbf{0.05}$
DSM_D	slope	30.95	4.87	3.07
	aspect	17.18	3.64	2.49

Table 6.21: Region 1: analysis of variance results for DSM_D (coherence>0.85).

		Aspect							
		N	NW	W	SW	S	SE	E	NE
Slope	$0-15°$	9.13	9.86	8.24	7.69	7.75	8.18	8.87	8.80
	$15-27°$	8.91	9.40	8.19	8.15	8.65	8.70	8.58	8.85
	$27-40°$	8.44	8.52	9.65	8.64	9.04	8.65	8.26	8.87
	$>40°$	9.17	8.59	10.35	9.45	10.47	9.76	9.30	9.80

Table 6.22: Region 1: DSM_{AD} accuracy [m] (coherence>0.85).

Model	**Parameter**	$\mathbf{F_{emp}}$	$\mathbf{F_{theo}}$	
			$\alpha = \mathbf{0.01}$	$\alpha = \mathbf{0.05}$
DSM_{AD}	slope	26.77	4.87	3.07
	aspect	5.02	3.64	2.49

Table 6.23: Region 1: analysis of variance results for DSM_{AD} (coherence>0.85).

6.7.2 Region 2

Analogously, the LiDAR derived model (R2LB5) was used for a morphology dependent accuracy estimate (Figure 6.12).
The same reasoning was followed for Region 2 where four classes of slope (the limits between the different classes of slopes, 16°-29°-43° corresponds to the 25^{th}, 50^{th} and 75^{th} percentile of the dataset) and eight classes of aspect (North, North-East, East, South-East, South, South-West, West, North-West) were formed. Figure 6.13 shows the slope classification and aspect classification separately, Figure 6.14 the classification based on both of them. Table 6.24 reports the size of the different classes in Region 2.

		Aspect							
		N	NW	W	SW	S	SE	E	NE
Slope	$0-16°$	2691	2690	2719	2129	2114	1724	2189	2177
	$16-29°$	2393	2449	2821	2151	2049	1587	2011	1854
	$29-43°$	2310	2513	3003	2394	2137	1511	2048	1873
	$>43°$	3263	2843	3843	2803	2851	1971	2917	2532

Table 6.24: Region 2: class size.

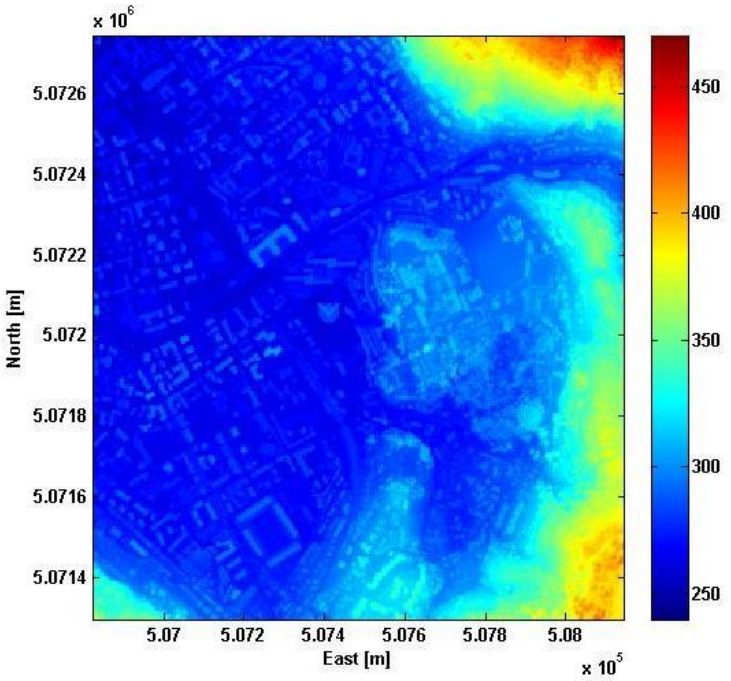

Figure 6.12: The LiDAR derived 5 × 5 m resolution model (R2LB5).

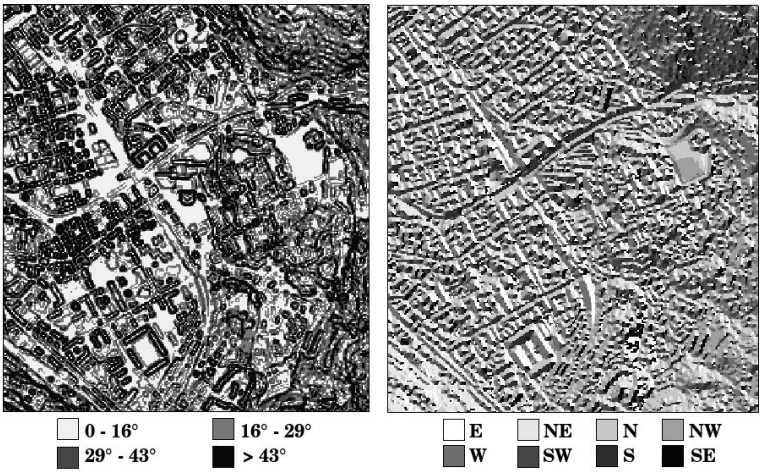

Figure 6.13: Region 2: classification based on slope (left) and on aspect (right).

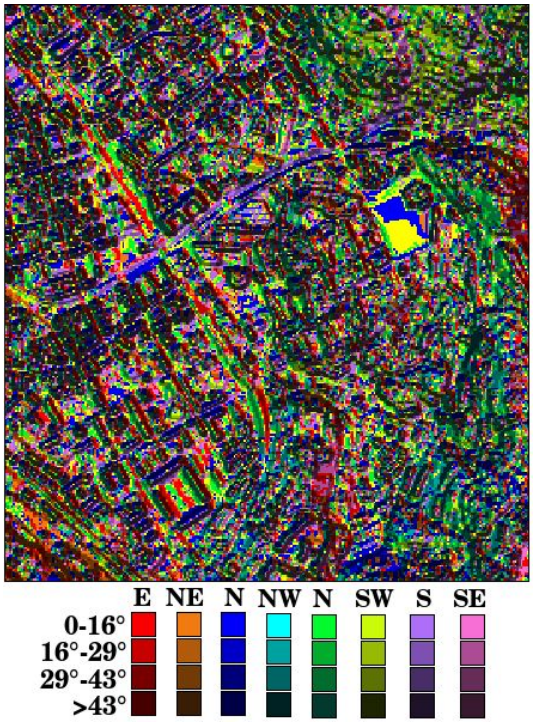

Figure 6.14: Region 2: classification based on slope and on aspect.

Analysis of variance for DSMs generated using all the sparse dataset

Tables 6.25, 6.27 and 6.29 contain respectively the accuracy for the DSM obtained by the ascending (DSM_A), the descending (DSM_D) and the union of ascending and descending points (DSM_{AD}). Table 6.26, 6.28 and 6.30 show the analysis of variance results. Also in this case there is a relevant dependence both slope and aspect.

		Aspect							
		N	NW	W	SW	S	SE	E	NE
Slope	$0-16°$	10.69	13.28	10.20	10.87	10.01	9.75	9.93	10.21
	$16-29°$	10.63	10.66	10.36	11.12	10.59	10.49	10.69	11.27
	$29-43°$	10.83	11.31	10.86	10.99	11.42	11.84	11.72	12.39
	$>43°$	13.51	13.04	12.30	12.68	12.38	12.53	12.99	14.05

Table 6.25: Region 2: DSM_A accuracy [m].

Model	**Parameter**	$\mathbf{F_{emp}}$	$\mathbf{F_{theo}}$	
			$\alpha = \mathbf{0.01}$	$\alpha = \mathbf{0.05}$
DSM_A	slope	61.83	4.87	3.07
	aspect	11.18	3.64	2.49

Table 6.26: Region 2: analysis of variance results for DSM_A.

		Aspect							
		N	NW	W	SW	S	SE	E	NE
Slope	$0 - 16°$	13.57	13.18	15.59	16.34	14.99	14.61	12.86	13.79
	$16 - 29°$	13.30	15.48	17.72	24.95	17.88	15.69	12.93	12.54
	$29 - 43°$	13.55	14.45	18.39	25.46	17.67	15.55	13.08	12.68
	$> 43°$	13.64	15.78	16.95	21.13	15.33	14.03	12.83	14.36

Table 6.27: Region 2: DSM_D accuracy [m].

Model	**Parameter**	$\mathbf{F_{emp}}$	$\mathbf{F_{theo}}$	
			$\alpha = \mathbf{0.01}$	$\alpha = \mathbf{0.05}$
DSM_D	slope	7.84	4.87	3.07
	aspect	85.66	3.64	2.49

Table 6.28: Region 2: analysis of variance results for DSM_D.

		Aspect							
		N	NW	W	SW	S	SE	E	NE
Slope	$0 - 16°$	10.40	12.90	10.55	10.78	10.01	10.11	9.69	10.64
	$16 - 29°$	10.70	11.03	10.36	13.24	10.87	10.78	10.15	10.56
	$29 - 43°$	10.91	10.81	10.74	11.66	11.41	11.43	11.43	11.76
	$> 43°$	12.81	12.64	12.19	12.60	11.98	11.90	12.37	13.12

Table 6.29: Region 2: DSM_{AD} accuracy [m].

Model	**Parameter**	$\mathbf{F_{emp}}$	$\mathbf{F_{theo}}$	
			$\alpha = \mathbf{0.01}$	$\alpha = \mathbf{0.05}$
DSM_{AD}	slope	32.39	4.87	3.07
	aspect	10.53	3.64	2.49

Table 6.30: Region 2: analysis of variance results for DSM_{AD}.

Analysis of variance for DSMs generated using just those points with a coherence higher than 0.85

		Aspect							
		N	NW	W	SW	S	SE	E	NE
Slope	$0 - 16°$	9.94	12.54	9.26	9.57	8.74	8.62	9.09	9.37
	$16 - 29°$	9.66	9.35	9.57	9.85	9.43	9.37	9.67	10.59
	$29 - 43°$	9.86	9.85	9.88	9.74	10.23	10.31	10.60	11.38
	$> 43°$	12.36	11.70	11.11	11.20	10.95	10.85	11.67	12.80

Table 6.31: Region 2: DSM_A accuracy [m] (coherence>0.85).

Model	**Parameter**	$\mathbf{F_{emp}}$	$\mathbf{F_{theo}}$	
			$\alpha = \mathbf{0.01}$	$\alpha = \mathbf{0.05}$
DSM_A	slope	35.92	4.87	3.07
	aspect	11.15	3.64	2.49

Table 6.32: Region 2: analysis of variance results for DSM_A (coherence>0.85).

		Aspect							
		N	NW	W	SW	S	SE	E	NE
Slope	$0 - 16°$	14.64	13.90	17.35	18.63	16.45	16.24	13.42	14.70
	$16 - 29°$	13.92	16.98	21.43	31.30	22.36	18.27	13.75	13.69
	$29 - 43°$	14.28	16.11	22.50	33.51	22.06	17.80	13.11	12.63
	$> 43°$	12.41	15.38	19.25	27.61	19.64	15.63	12.07	13.39

Table 6.33: Region 2: DSM_D accuracy [m] (coherence>0.85).

Model	**Parameter**	$\mathbf{F_{emp}}$	$\mathbf{F_{theo}}$	
			$\alpha = \mathbf{0.01}$	$\alpha = \mathbf{0.05}$
DSM_D	slope	9.80	4.87	3.07
	aspect	97.45	3.64	2.49

Table 6.34: Region 2: analysis of variance results for DSM_D (coherence>0.85).

		Aspect							
		N	NW	W	SW	S	SE	E	NE
Slope	$0 - 16°$	9.96	12.21	9.33	9.37	8.73	8.69	8.69	9.72
	$16 - 29°$	9.48	9.52	9.37	11.88	9.47	9.26	9.44	9.94
	$29 - 43°$	9.87	9.73	9.81	10.09	10.07	10.07	10.37	10.86
	$> 43°$	12.04	11.49	11.12	11.23	10.62	10.64	11.11	12.02

Table 6.35: Region 2: DSM_{AD} accuracy [m] (coherence>0.85).

Model	**Parameter**	$\mathbf{F_{emp}}$	$\mathbf{F_{theo}}$	
			$\alpha = \mathbf{0.01}$	$\alpha = \mathbf{0.05}$
DSM_{AD}	slope	24.37	4.87	3.07
	aspect	9.06	3.64	2.49

Table 6.36: Region 2: analysis of variance results for DSM_{AD} (coherence>0.85).

6.8 Fusion

The purpose of the work was to find a way to merge ascending and descending DSMs to obtain new DSMs with higher accuracies. Fusion was done associating to each grid node a weighted mean between the DSM coming from the ascending stereo-pair (DSM_A) and the DSM coming from the descending one (DSM_D). The weights are given by the inverse of the variances associated to each cell.

$$h = \frac{1}{\sigma^2_{ASC}} h_{ASC} + \frac{1}{\sigma^2_{DESC}} h_{DESC} \tag{6.1}$$

A value of accuracy can be associated to each estimated height; this can be computed in different ways, more precisely:

- the accuracy value obtained comparing the DSM with the LiDAR reference DSM. In this way to all the cell is attributed a value of accuracy equal to the square root of the mean of the square residuals;

- the morphology dependent accuracy.

Tables 6.37 and 6.39 report the results of the fusion of ascending (DSM_A) and descending (DSM_D) models.

Numbers of cells	**Source of error**	**Rmse [m]**	**Sigma [m]**	**Bias [m]**	**LE95**
82324	global estimated accuracy	6.87	6.82	-0.79	17.53
80391	morphology dependent accuracy	6.80	6.74	-0.85	17.39

Table 6.37: DSM accuracy in Region 1 (coherence>0.75).

Numbers of cells	**Source of error**	**Rmse [m]**	**Sigma [m]**	**Bias [m]**	**LE95**
82324	global estimated accuracy	7.04	7.02	-0.54	16.70
80391	morphology dependent accuracy	6.97	6.95	-0.59	16.86

Table 6.38: DSM accuracy in Region 1 (coherence>0.85).

Numbers of cells	**Source of error**	**Rmse [m]**	**Sigma [m]**	**Bias [m]**	**LE95**
76560	global estimated accuracy	8.38	8.37	-0.34	21.37
76560	morphology dependent accuracy	8.18	8.17	-0.42	20.96

Table 6.39: DSM accuracy in Region 2 (coherence>0.75).

Numbers of cells	Source of error	Rmse [m]	Sigma [m]	Bias [m]	LE95
76560	global estimated accuracy	8.16	8.10	-0.96	20.63
76560	morphology dependent accuracy	7.95	7.87	-1.12	20.15

Table 6.40: DSM accuracy in Region 2 (coherence>0.85).

Model	Coherence	Number of cells	RMSE [m]	sigma [m]	bias [m]	LE95
$R1 - DSM_{AD}$	>0.75	82324	7.24	7.08	-1.51	19.72
$R1 - DSM_{AD}$	>0.85	82324	6.77	6.33	-1.39	17.37
$R2 - DSM_{AD}$	>0.75	76560	8.70	8.60	-1.31	22.76
$R2 - DSM_{AD}$	>0.85	76560	7.98	7.81	-1.63	22.19

Table 6.41: Region 1: Bilinear interpolated DSMs accuracies.

The accuracy of the 0.85 coherence DSMs is not significantly different from that of 0.75 coherence DSMs, 7m accuracy for Region 1 and 8m for Region 2. The same can be said from the comparison between the DSMs obtained from the interpolation of the ascending and descending sparse data together and those obtained by the fusion of the separate ascending and descending DSMs. In fact, looking at Table 6.41 which summarizes the results of Table 6.7, 6.8, 6.9, 6.10 it seems that there is no significant difference. The straightforward interpolation of the two datasets, ascending and descending one, seems to be the more convenient in this case, at least at this 95% implemented RMSE evaluation.

Conclusions

The validation of new interferometric products, deformation time series and digital surface models, was the main motivation of this thesis. The work was funded by the Italian Space Agency within two different projects, MORFEO and COSMO-SkyMed, both aiming at the assessment of the potentiality of new Earth observations from satellite-borne sensors and in particular from radar ones.

Interferometric SAR techniques are becoming more and more efficient either in Earth surface deformation monitoring and in surface modelling. Different techniques for the SAR images analysis are available both for the phase and the intensity contents exploitation.

Within the MORFEO project, for instance, the potential support of differential interferometric SAR products to local deformation monitoring, such as landslides, was evaluated within the many other possible consolidated or new techniques available. In this framework two different algorithms SBAS and SPINUA, developed by two different Italian research groups, the CNR-IREA Napoli group and the Politecnico di Bari group, were applied to the same stack of ENVISAT SAR images to determine LOS deformation time series of point lying on landslide test-sites.

Within the COSMOSkyMed project, the validation of differential interferometric SAR products for urban areas deformation monitoring (IREA Napoli) was performed as well as the validation of new digital surface modelling computed by radargrammetric techniques (UNIROMA).

Our contribution to both projects consisted in the definition of procedures for comparison, validation and fusion of the radar products. More precisely, within the MORFEO project we had to perform a cross comparison between landslides deformation time series produced on the same test area of Ivanchic landslide by the two above mentioned DInSAR techniques and a comparison with independent GNSS deformation time series derived from observation campaigns partly performed within the project itself. Within the CSM project the comparison was to be performed between DSMs for validation purposes and fusion strategies were studied for the generation of possible integrated,

high accurate models.
The comparison problem of both projects was approached on two different levels: one more theoretical, the other more practical as we need to produce not only possible methodologies but fully working algorithms and results. We had room to study an optimal validation strategy based on Wiener-Kolmogorov stochastic field linear prediction theory. This was published and fully reported in this dissertation even if it could not be directly applied to the deformation fields or height fields of MORFEO and CSM projects. A stochastic approach was also proposed and implemented to solve for the fusion of DSMs problem which results quite promising but still to be made suitable to a more automatic blind application.
A common principle in all the tackled problems can be invoked: it is that of minimizing the errors introduced in the data manipulations (projections, predictions in space and time) needed to make different aspects of the same field (either surface deformation or height field) seen by different techniques comparable.
The errors depend on the data distribution but also on the field regularity properties. This general issue can be declined in different ways such as for instance what is the best point where to make the comparison and possibly the fusion? Which is the grid where to produce a final DSM? What is the best technique to make interpolation?
There is still a lot to do, but some conclusion can be drawn. For the landslide deformation validation, for instance, it was clearly proven that SAR accuracies need high performing GNSS positioning systems to assure millimetric accuracies of the point coordinates; the landslide behaviour is not homogeneous at all. Very localized predictions are needed especially when a classification of the different moving patches is not possible. Local comparisons based on Nearest Neighbour interpolation were applied to obtain the validation results. In this respect the two techniques produce equivalent results. As for the external validation, this was not possible due to the poor accuracy of the GNSS time series.
The limiting factor in DSM generation and manipulation was their non homogeneous and isotropic behaviour, which makes the stochastic approaches quite useless: such properties are in fact needed for the estimation of the field covariance function. Even in this case a local approach could be a solution, but this is still a challenging issue to deal with. Nevertheless, comparisons were performed by applying possible and reasonable, even if not optimal, interpolation techniques depending on the kind of data at hand. Outlier rejection based on internal consistency tests and external validation against a very accurate and high resolution LiDAR DSM were performed always obtaining accuracies comparable with the nominal ones. Moreover,

morphology dependent accuracies were evaluated based on a previous terrain classification by slope and aspect characteristics. Those accuracies were then used to improve a simple weighted average solution to the fusion problem. Radargrammetric DSMs in two different test sites in COMO were generated by bilinear interpolation on a 5m resolution grid. They were then validated always against a LiDAR DSM showing an accuracy of about 7.5m. The use of such detailed local SAR derived models could be used to integrate the SRTM low resolution global DSM. Again the way to perform such an integration represents an interesting topic in the field this thesis tried to explore.

Acknowledgments

I would like to thank the group of IREA of Naples, the group of Dipartimento Interateneo di Fisica of the Politecnico di Bari, in particular Davide Nitti, and Giovanna Ober of Carlo Gavazzi Space for their helpfulness and kind collaboration throughout the MORFEO validation study.

Acknowledgements go to the group of professor Radicioni of the University of Perugia and to CNR IRPI Perugia for all their technical and logistic support during the GPS measuring campaigns held in Assisi in April 2009, April 2010 and October 2010.

Thanks go to the team of the Geodesy and Geomatic Area of the University of Rome La Sapienza, in particular to Andrea Nascetti, for providing radargrammetric data and for their collaboration within the COSMO-SkyMED project.

Finally, I would like to thank my tutor Giovanna Venuti for her support during all my Ph.D. studies.

Bibliography

M. Abrams, S. Hook, B. Ramachandran, and E.D. Center. Aster user handbook, version 2. *Jet Propulsion Laboratory*, page 112, 2002.

F.J. Aguilar, F. Aguera, M.A. Aguilar, and F. Carvajal. Effects of terrain morphology, sampling density, and interpolation methods on grid dem accuracy. *Photogrammetric engineering and remote sensing*, 71(7):805, 2005.

ASI. Cosmo-skymed system description & user guide. `http://www.asi.it/it/attivita/osservazione_terra/cosmoskymed`, 2007.

ASI. Morfeo. `http://www.morfeoproject.it`, 2011.

P. Audenino, L. Rognant, J.M. Chassery, and J.G. Planes. Fusion strategies for high resolution urban dem. In *Remote Sensing and Data Fusion over Urban Areas, IEEE/ISPRS Joint Workshop 2001*, pages 90–94. IEEE, 2001.

E.P. Baltsavias. Airborne laser scanning: basic relations and formulas. *ISPRS Journal of Photogrammetry and Remote Sensing*, 54(2):199–214, 1999.

R. Bamler and P. Hartl. Synthetic aperture radar interferometry. *Inverse problems*, 14(4):R1–R54, 1998.

G. e Lanari R. e Sansosti E. Berardino, P. e Fornaro. A new algorithm for surface deformation monitoring based on small baseline differential sar interferograms. *Geoscience and Remote Sensing, IEEE Transactions on*, 40(11):2375 – 2383, 2002.

L. Biagi. I fondamentali del gps. *Geomatics Workbooks*, 8, 2006.

F. Bovenga, A. Refice, R. Nutricato, L. Guerriero, and MT Chiaradia. Spinua: a flexible processing chain for ers/envisat long term interferometry. In *Proceedings of ESA-ENVISAT Symposium, Salzburg, Austria*, pages 6–10, 2004.

C. Brenner. Aerial laser scanning - systems, processing, spplications. International Summer School, Digital recording and 3D Modeling, Aghios Nikolaos, Crete, Greece, 2006.

M.A. Brovelli and S. Lucca. Inverse calibration of lidar filtering parameters: Ucode/grass integration. ISPRS Hannover Workshop, 2009.

P. Canuti, E. Marcucci, S. Trastulli, P. Ventura, and G. Vincenti. Studi per la stabilizzazione della frana di assisi. In *Nat. Geotech. Congress, Bologna*, pages 14–16, 1986.

P. Capaldo, M. Crespi, F. Fratarcangeli, A. Nascetti, and F. Pieralice. High-resolution sar radargrammetry: A first application with cosmo-skymed spotlight imagery. *Geoscience and Remote Sensing Letters, IEEE*, (99):1–5, 2011.

L. Cascini, D. Peduto, G. Fornaro, R. Lanari, G. Zeni, and F. Guzzetti. Spaceborne radar interferometry for landslide monitoring. *Rainfall-induced landslides: mechaisms, monitoring*, 2009.

V. Chaplot, F. Darboux, H. Bourennane, S. Leguedois, N. Silvera, and K. Phachomphon. Accuracy of interpolation techniques for the derivation of digital elevation models in relation to landform types and data density. *Geomorphology*, 77(1-2):126–141, 2006.

M.E. Cilli, F. Radicioni, and A. Stoppini. Analisi dei risultati di recenti campagne di misura nella rete di monitoraggio gps della frana di assisi. Number 2830. CNR-GNDCI, December 2002. Conservazione della montagna a rischio idrogeologico.

F. Cilloccu, S. Dequal, M. Brovelli, M. Crespi, and A. Lingua. Ortoimmagini 10k e modelli altimetrici: specifiche tecniche, 2007.

J. Colesanti, C. e Wasowski. Indagare frane con spaziali radar ad apertura sintetica (sar) interferometria. *Geologia applicata*, 88:173–199, 2006.

M. Crespi, P. Capaldo, F. Fratarcangeli, A. Nascetti, and F. Pieralice. Dsm generation from very high optical and radar sensors: Problems and potentialities along the road from the 3d geometric modeling to the surface model. In *Geoscience and Remote Sensing Symposium (IGARSS), 2010 IEEE International*, pages 3596–3599. IEEE, 2010.

M. Crosetto. *Interferometric SAR for DEM Generation: Validation of an Integrated Procedure Based on Multisource Data*. PhD thesis, Doctorate in Geodetic and Surveying Sciences, Politecnico di Milano, 1998.

M. Crosetto and F. Pérez Aragues. Radargrammetry and sar interferometry for dem generation: Validation and data fusion. In *SAR workshop: CEOS Committee on Earth Observation Satellites*, volume 450, page 367, 2000.

A. Cuartero, A.M. Felicisimo, and F.J. Ariza. Accuracy, reliability, and depuration of spot hrv and terra aster digital elevation models. *Geoscience and Remote Sensing, IEEE Transactions on*, 43(2):404–407, 2005.

R. Dach, U. Hugentobler, P. Fridez, and M. Meindl. Bernese gps software version 5.0. *Astronomical Institute, University of Bern*, 2007.

N. El-Sheimy, C. Valeo, and A. Habib. *Digital terrain modeling: acquisition, manipulation, and applications*. Artech House, 2005.

ESA. ESA mission, ENVISAT. `http://envisat.esa.int`, 2011.

G. Fastellini, F. Radicioni, and A. Stoppini. The assisi landslide monitoring: a multi-year activity based on geomatic techniques. *Applied Geomatics*, pages 1–10, 2011.

A. Ferretti, C. Prati, and F. Rocca. Permanent scatterers in sar interferometry. *Geoscience and Remote Sensing, IEEE Transactions on*, 39(1):8–20, 2001.

M. Gilardoni, F. Sansò, and G. Venuti. Optimal cross validation of different surveying techniques. In *Atti del 7° Hotine-Marussi Symposium*, pages 1–9. Springer Verlag, 2010.

F. Guzzetti, L. Candela, R. Carlà, G. Fornaro, R. Lanari, A. Mondini, G. Ober, F. Fiorucci, and G. Zeni. MORFEO project: use of remote sensing technology for mapping, monitoring and forecasting landslides. In *EGU General Assembly 2009*, volume 11, page 7896, 2009a.

F. Guzzetti, M. Manunta, F. Ardizzone, A. Pepe, M. Cardinali, G. Zeni, P. Reichenbach, and R. Lanari. Analysis of ground deformation detected using the sbas-dinsar technique in umbria, central italy. *Pure and Applied Geophysics*, 166(8):1425–1459, 2009b.

A. Hirano, R. Welch, and H. Lang. Mapping from aster stereo image data: Dem validation and accuracy assessment. *ISPRS Journal of Photogrammetry and Remote Sensing*, 57(5-6):356–370, 2003.

Jet Propulsion Laboratory. Aster (advanced spaceborne thermal emission and reflection radiomater). `http://asterweb.jpl.nasa.gov`.

R.F. Keim, A.E. Skaugset, and D.S. Bateman. Digital terrain modeling of small stream channels with a total-station theodolite. *Advances in water resources*, 23(1):41–48, 1999.

W. Knöpfle, G. Strunz, and A. Roth. Mosaicking of digital elevation models derived by sar interferometry. *International Archives of Photogrammetry and Remote Sensing*, 32:306–313, 1998.

K.R. Koch. *Parameter estimation and hypothesis tersting in linear models*. Springer Verlag, 1999.

T. Krarup. *in Mathematical Foundation of Geodesy: selected papers of Torben Krarup*. Springer Verlag, 2006.

K. Kraus. *Photogrammetry: Vol. 1: Fundamentals and standard processes*. Dummler, 1992.

F.G. Lemoine, S.C. Kenyon, J.K. Factor, R.G. Trimmer, N.K. Pavlis, D.S. Chinn, C.M. Cox, S.M. Klosko, S.B. Luthcke, M.H. Torrence, et al. The development of the joint nasa gsfc and the national imagery and mapping agency(nima) geopotential model egm 96. *NASA*, (19980218814), 1998.

Z. Li. On the measure of digital terrain model accuracy. *The Photogrammetric Record*, 12(72):873–877, 1988.

Z. Li, Q. Zhu, and C. Gold. *Digital terrain modeling: principles and methodology*. CRC, 2005.

S. Lucca. *Validation and Fusion of Digital Surface Model*. PhD thesis, Doctoral Programme in Environmental and Infrastructure Engineering, Politecnico di Milano, 2012.

C.L. Miller and R.A. Laflamme. *The Digital Terrain Model: Theory & Application*. MIT Photogrammetry Laboratory, 1958.

A.V. Monti Guarnieri. Notes of the course "sar imaging". `http://www.egecomo.polimi.it/`, 2011.

O. Mora, J.J. Mallorqui, and A. Broquetas. Linear and nonlinear terrain deformation maps from a reduced set of interferometric sar images. *Geoscience and Remote Sensing, IEEE Transactions on*, 41(10):2243–2253, 2003.

H. Papasaika, D. Poli, and E. Baltsavias. A framework for the fusion of digital elevation models. *The International Archives of the Photogrammetry, Remote Sensing and Spatial Information Sciences, Beijing*, 2008.

H. Papasaika, D. Poli, and E. Baltsavias. Fusion of digital elevation models from various data sources. In *Advanced Geographic Information Systems & Web Services, 2009. GEOWS'09. International Conference on*, pages 117–122. IEEE, 2009.

A. Papoulis. Probability, random variables, and stochastic processes, 1991.

B. Rabus, M. Eineder, A. Roth, and R. Bamler. The shuttle radar topography mission a new class of digital elevation models acquired by spaceborne radar. *ISPRS Journal of Photogrammetry and Remote Sensing*, 57(4):241–262, 2003.

H. Raggam, K. Gutjahr, R. Perko, and M. Schardt. Assessment of the stereo-radargrammetric mapping potential of terrasar-x multibeam spotlight data. *IEEE Transactions on Geoscience and Remote Sensing*, 48(2):971–977, 2010.

M. Reguzzoni and G. Venuti. Notes of the course "statistical analysis for environmental data". `http://geomatica.como.polimi.it/corsi/tratt_oss`, 2011.

E. Rodriguez, C.S. Morris, and J.E. Belz. A global assessment of the srtm performance. *Photogrammetric Engineering and Remote Sensing*, 72(3): 249–260, 2006.

P. Salvati, C. Bianchi, and F. Guzzetti. Catalogo delle frane e delle inondazioni storiche in umbria. *CNR IRPI e Fondazione Cassa di Risparmio di Perugia, ISBN-10*, pages 88–95172, 2006.

F. Sansó. *Il trattamento statistico dei dati*, chapter 5: L'inferenza per le stime della teoria dei minimi quadrati. Clup, 1993.

F. Sansò. Quaderni di trattamento statistico dei dati, 1996.

F. Sansò, G. Venuti, IN Tziavos, GS Vergos, VN Grigoriadis, and G. Vergos. Geoid and sea surface topography from satellite and ground data in the mediterranean region-a review and new proposals. *BGG*, 67(3):155 – 201, 2008.

H. Schultz, E.M. Riseman, F.R. Stolle, and D.M. Woo. Error detection and dem fusion using self-consistency. In *Computer Vision, 1999. The Proceedings of the Seventh IEEE International Conference on*, volume 2, pages 1174–1181. IEEE, 1999.

A.V. Team. Aster global dem validation summary report. `http://lpdaac.usgs.gov`, 2009.

P.J.G. Teunissen. *GPS for Geodesy*, volume 60. Springer, 1996.

T. Toutin. Impact of terrain slope and aspect on radargrammetric dem accuracy. *ISPRS journal of photogrammetry and remote sensing*, 57(3): 228–240, 2002.

T. Toutin and R. Chénier. 3-d radargrammetric modeling of radarsat-2 ultrafine mode: preliminary results of the geometric calibration. *Geoscience and Remote Sensing Letters, IEEE*, 6(2):282–286, 2009.

D. Triglione. Metodi e algoritmi di validazione di terreni digitali in grass. Master's thesis, Politecnico di Milano, Facoltà di Ingegneria di Como, 1999.

S. Usai. A least squares database approach for sar interferometric data. *Geoscience and Remote Sensing, IEEE Transactions on*, 41(4):753–760, 2003.

H. Wackernagel. *Multivariate geostatistics. An introduction with applications. Third edition.* Springer, Berlin, 1995.

A. Wehr and U. Lohr. Airborne laser scanning–an introduction and overview. *ISPRS Journal of Photogrammetry and Remote Sensing*, 54(2-3):68–82, 1999.

B.M. Whelan, A.B. McBratney, and B. Minasny. Vesper 1.5 spatial prediction software for precision agriculture. In *Precision Agriculture, Proc. 6th Int. Conf. on Precision Agriculture, ASA/CSSA/SSSA, Madison, WI, USA*, 2002.

Appendix A

Optimal cross-validation of different surveying techniques

When monitoring deformations by means of different sensors, one has to be sure that the various observations do see the same variations in time of the Earth surface. As an example one can think of a deformation as seen by the SAR technique and the deformation of the same surface as seen by GPS (see Chapter 2). To this aim a hypothesis testing procedure has to be set up (Koch [1999]). The first question is how to compare the different data sets, which usually do not refer neither to the same positions in space nor to the same time. The standard prediction of one set of variables from the other, for instance, is not always the best solution. It is better to use both observation sets to predict one and the same functional of the "random field" describing the deformation pattern and to evaluate the difference between the two predictions. This difference has to be small on condition that the signal we try to estimate has a fixed amplitude in mean quadratic sense. The problem is formally solved and a few examples are illustrated. This work was presented at the 7° Hotine-Marussi symposium held in Rome in July 2009 (Gilardoni et al. [2010]).

A.1 Definition of the problem

The problem we want to discuss, described in abstract form is as follows: let $\{u(t)\}$, $t \in T$, be a random field, defined on some set $T(T \subseteq \Re^n)$, with zero mean

$$E\{u(t)\} = 0, \tag{A.1}$$

and covariance function

$$E\{u(t)u(s)\} = C(t,s) \tag{A.2}$$

and assume that there is a vector of "observations" performed on $u(t)$, which are linear functionals of $u(t)$ with some additive noise

$$\underline{Y} = \underline{L}(u) + \underline{\nu}. \tag{A.3}$$

For (A.3) to be meaningful we need that the components $L_i(\ i = 1, \ldots, N)$ of $\underline{L}$ to be bounded linear stochastic functionals; namely we shall assume that, adopting Krarup's notation (Krarup [2006])

$$E\{L_i(u)^2\} = L_{it}\{L_{is}[C(t,s)]\} = C(L_i, L_i) < +\infty; \tag{A.4}$$

in addition it is assumed that

$$E\{\underline{\nu}\} = 0, \quad E\{\underline{\nu}\underline{\nu}^+\} = C_\nu \tag{A.5}$$

where C_ν is a known covariance matrix, and finally that u and ν are linearly independent, implying

$$E\{\underline{L}(u)\underline{\nu}^+\} = 0; \tag{A.6}$$

Note that, under the above conditions, the covariance of $\underline{Y}$ is known and given by

$$C_Y = C(\underline{L}, \underline{L}^+) + C_\nu. \tag{A.7}$$

Suppose that a similar situation is independently duplicated; namely there is another random field $\{w(t)\}$, $t \in T$, generally not centered, but with the same covariance for u, and another vector of observations

$$\underline{Z} = \underline{K}(w) + \underline{\eta} \tag{A.8}$$

with, $\underline{K} = \{K_i;\ i = 1, 2, \ldots, M)$ and

$$C(k_i, k_i) < +\infty, \tag{A.9}$$

$$E\{\underline{\eta}\} = 0, \quad E\{\underline{\eta}, \underline{\eta}^+\} = C_\eta, \quad E\{\underline{K}(w)\underline{\eta}^+\} = 0. \tag{A.10}$$

We further assume that $\underline{\nu}$ and $\underline{\eta}$ are linearly independent of one another and, both, of $u(t)$ and $w(t)$.
The hypothesis to test is:

$$H_0 : u = w, \tag{A.11}$$

i.e. that the two sets of measurements $\underline{Y}$ and $\underline{Z}$ refer to one and the same random field. Among other things, this implies that there is no bias between

u and w. So the problem becomes that of finding a suitable statistics to verify (A.11). To be simple, we will try to find a linear function of the observables that becomes zero in the average when (A.11) is satisfied and that is as small as possible in variance, in a suitable sense, so as to be very sensitive to all departures from (A.11). To understand the possible applications of a schema like that we make two examples.
Example 1: Assume you want to build a digital elevation model (DEM), Chapter 3, for a piece of the Earth surface considering data coming from two different techniques; e.g. a SAR surveying (SRTM) and photogrammetry. The two techniques will produce fields with different knots so that the hypothesis that there is no bias between them is not immediately verifiable. Even more the SAR will give a grid of mean heights, while the photogrammetric model refers to almost point-wise observations.
Example 2: Assume a landslide to be monitored by SAR and GPS. The first techniques observes the on going deformation along the line of sight (LOS) at some highly coherent points; the second observes the deformation vector at some other points in the same area. In this case, by projecting the GPS $3D$ deformation vector along the SAR LOS, $u(\underline{t})$ will be the LOS component of the deformation pattern (see Chapter 2). The hypothesis is now that the two techniques see the same pattern, so that one can be used to validate the other.

In Section A.2 those problems will be formalized through a suitable target function that will be minimized. Then Section A.3 example 2 is developed.

A.2 The optimization problem

As we said, under the assumption (A.1), the sensible thing to do is to try to estimate a linear functional $M(\cdot)$ from both observation sets and then to take the difference of the estimates. As we know that, by a Wiener-Kolmogorov optimal predictor (see Section 1.3), no information can be drawn on any subspace of functionals orthogonal to both $\underline{Y}$ and $\underline{Z}$, instead of defining one problem for a general $M(\cdot)$, we rather define directly the statistic

$$S = \underline{\lambda}^{+}\underline{Y} - \underline{\mu}^{+}\underline{Z} \tag{A.12}$$

that we shall try to make as small as possible in mean quadratic sense. Under the assumption (A.1) and hypothesis (A.11), S has zero average and its variance, representing the departure from zero, is:

$$F(\underline{\lambda}, \underline{\mu}) = \sigma^2(S) = E\{S^2\} = \underline{\lambda}^{+} C_Y \underline{\lambda} + \underline{\mu}^{+} C_Z \underline{\mu} - 2\underline{\lambda}^{+} C_{YZ} \underline{\mu} \tag{A.13}$$

where (from (A.7))

$$\begin{aligned} C_Y &= C(\underline{L}, \underline{L}^+) + C_\nu, \\ C_Z &= C(\underline{K}, \underline{K}^+) + C_\eta, \\ C_{YZ} &= C(\underline{L}, \underline{K}^+). \end{aligned} \tag{A.14}$$

Obviously, we cannot look for an unconstrained minimum of the variance (A.13), because this is indeed obtained at $\underline{\lambda} = 0$, $\underline{\mu} = 0$. Therefore we must keep the couple $(\underline{\lambda}, \underline{\mu})$ on a surface far away from zero by imposing a suitable condition. The theory gets its simplest and most elegant form, if we choose the following normalization condition:

$$G(\underline{\lambda}, \underline{\mu}) = E\{(\underline{\lambda}^+ \underline{Y} + \underline{\mu}^+ \underline{Z})^2\} = \underline{\lambda}^+ C_Y \underline{\lambda} + \underline{\mu}^+ C_Z \underline{\mu} + 2\underline{\lambda}^+ C_{YZ} \underline{\mu} = 1 \tag{A.15}$$

It is interested to remark that exactly the same equations would be obtained by imposing separately the two variables $\underline{\lambda}^+ \underline{Y}$ and $\underline{\mu}^+ \underline{Z}$ to have a unit variance. The minimization of the Lagrange target function

$$\mathcal{L}(\underline{\lambda}, \underline{\mu}) = F(\underline{\lambda}, \underline{\mu}) - \gamma G(\underline{\lambda}, \underline{\mu}) \tag{A.16}$$

leads to the following normal system:

$$\begin{pmatrix} C_Y & -C_{YZ} \\ -C_{ZY} & C_Z \end{pmatrix} \begin{pmatrix} \underline{\lambda} \\ \underline{\mu} \end{pmatrix} = \gamma \begin{pmatrix} C_Y & C_{YZ} \\ C_{ZY} & C_Z \end{pmatrix} \begin{pmatrix} \underline{\lambda} \\ \underline{\mu} \end{pmatrix} \tag{A.17}$$

This is a generalized eigenvalue problem: for each eigenvalue γ_n, we have the corresponding eigenvector $[\underline{\lambda}_n^+, \underline{\mu}_n^+]^+$, which can be normalized with condition (A.15). By multiplying A.17 by $[\underline{\lambda}_n^+, \underline{\mu}_n^+]$, and taking into account (A.15), one gets:

$$\gamma_n = F(\underline{\lambda}_n, \underline{\mu}_n), \tag{A.18}$$

and the original problem becomes that of finding the minimum eigenvalue of (A.17) and the corresponding eigenvector. This is similar to canonical analysis discussed in literature (Wackernagel [1995]). It can be observed that the problem can be dimensionally reduced. Getting, for instance, $\underline{\lambda}$ from the first row of (A.17)

$$\underline{\lambda} = \alpha C_Y^{-1} C_{YZ} \underline{\mu} \tag{A.19}$$

and substituting in the second one, it results

$$(C_Z - \alpha^2 C_{ZY} C_Y^{-1} C_{YZ}) \underline{\mu} = 0 \tag{A.20}$$

with

$$\alpha = \frac{1+\gamma}{1-\gamma} \tag{A.21}$$

Note that (A.21) implies

$$\gamma(\alpha) = \frac{\alpha-1}{\alpha+1} \tag{A.22}$$

and that

$$\gamma(-\alpha) = \frac{1}{\gamma(\alpha)} \tag{A.23}$$

Since $F(\underline{\lambda}, \underline{\mu})$ is positive by definition (see A.13) , due to (A.18), γ is positive too. Then from (A.22) it can be seen that either $\alpha > 1$ or $\alpha < -1$, which is complying with the fact that the values of α from (A.20) come in couples with the same modulus. Since (A.22) $\alpha > 1$ implies $\gamma < 1$, then from (A.23) we have that $\alpha < 1$ implies $\gamma > 1$.
It follows that we have to find the minimum positive α, such that α^2 is an eigenvalue of (A.20), and the corresponding eigenvector $\underline{\mu}$. There on, we compute λ from (A.19). It is not difficult to see that, if $(\alpha, \underline{\lambda}, \underline{\mu})$ is the triple corresponding to γ_{min}, then $(-\alpha, \underline{\lambda}, -\underline{\mu})$ is the triple corresponding to γ_{max}.
Remark 1. Let us consider a particular case that we shall develop in Section A.3: this is when Z is one dimensional. In this case, we have:

$$C_Z = \sigma_Z^2 = C(K,K) + \sigma_\eta^2 \tag{A.24}$$

$$C_{YZ} = \begin{bmatrix} \vdots \\ C(L_i, K) \\ \vdots \end{bmatrix} \equiv \underline{c}_z \tag{A.25}$$

and the equation for the eigenvalues is simply

$$\sigma_Z^2 - \alpha^2 \underline{c}_Z^+ C_Y^{-1} \underline{c}_Z = 0 \tag{A.26}$$

with the two solutions:

$$\alpha = \pm \frac{\sigma_Z}{\left[\underline{c}_Z^+ C_Y^{-1} \underline{c}_Z\right]^{1/2}} \tag{A.27}$$

Getting the positive root, which is the one that provides the value γ_{min}, the corresponding eigenvector is

$$\left[\underline{\lambda} = \alpha\mu C_Y^{-1} \underline{c}_Z, \mu\right], \tag{A.28}$$

where μ has to be fixed so as to satisfy the normalization condition (A.15). Indeed, this last condition is quite irrelevant, while the interesting this is that by using (A.28) one finds the sought statistics

$$S = \mu(\alpha \underline{c}_Z^+ C_Y^{-1} Y - Z) \tag{A.29}$$

In turn, by using (A.27), this can be written as:

$$S = \mu\sigma_Z \left[\frac{\underline{c}_Z^+ C_Y^{-1} Y}{\sqrt{\underline{c}_Z^+ C_Y^{-1} \underline{c}_Z}} - \frac{Z}{\sigma_Z} \right] \tag{A.30}$$

The multiplicative constant in S has not a particular meaning, in fact it is one and the same scale for both S and its standard deviation. What is in parenthesis, though, is quite suggestive: S is basically the best linear predictor of Z from Y, normalized to have variance 1, minus Z, also normalized to variance 1. That seems a good solution to our validation problem. It is interesting to apply (A.30) when Y too is one dimensional. To make it simple, we assume even that $\sigma_Y = \sigma_Z = 1$ and $\rho > 0$. By applying (A.30) we find

$$S = \mu\,(Y - Z) \tag{A.31}$$

A.3 A case study

As deeply described in Chapter 2, within the Space Italian Agency project MORFEO, the Politecnico of Milano had to perform the DInSAR data validation by means of GPS. The optimal statistic previously described was applied considering GPS data and SBAS DInSAR LOS deformation time series regarding the Ivancich landslide (section 2.1); in particular the estimated coordinates, for the year 2006 and 2007, of 25 points belonging to the GPS monitoring network (Section 2.3) and SBAS (Section 2.2) deformations series available on 55 highly coherent points located as in Figure A.1. Since the GPS data used referred to 2006 and 2007 campaigns, from the DInSAR deformation series we retrieved those related to the same time span. The optimal statistics (A.30) was applied, by comparing the multi-dimensional SAR data set, denser then the GPS one, with each GPS point, that is to say, performing 25 different tests.

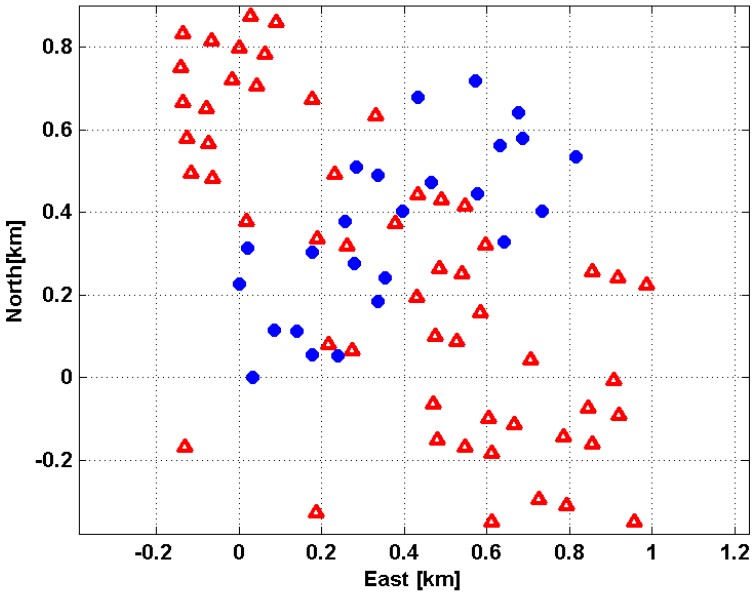

Figure A.1: GPS (circles) and SAR (triangles) points on the monitored landslide.

The field u defined on $t \in T \equiv \Re^2$, observed by both GPS and SAR, apart from the mean, is the LOS deformation field, that it is assumed to have a homogeneous and isotropic variogram

$$\gamma(|s-t|) = \frac{1}{2} E\left\{[u(t) - u(s)]^2\right\} \tag{A.32}$$

which is related to the covariance function by the following relation

$$\gamma(|s-t|) = C(t,t) + C(s,s) - 2C(s,t). \tag{A.33}$$

Note that the LOS is considered constant over the area. From SAR data we estimated the covariance function of u, by computing first their empirical variogram (Figure A.2) and then exploiting relation A.33 (Sansò et al. [2008]).

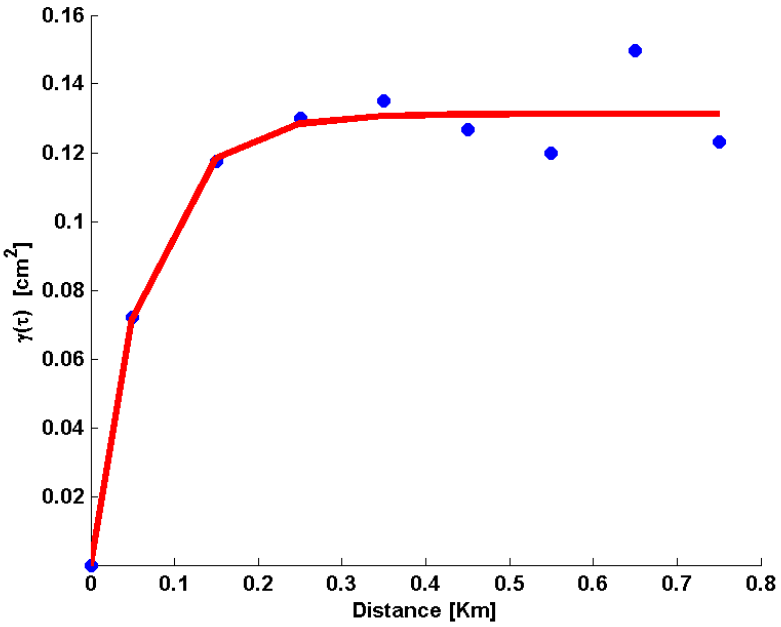

Figure A.2: Empirical variogram (blue circles) and interpolated, conditionally negative defined, model (red line).

Even more, the estimate of the nugget effect gave us an estimate of noise variance σ_ν^2 of the SAR data, which can not be directly computed by the SAR data analysis.
We found

$$C(|s-t|) = 0.13\ e^{(-15.31|s-t|)} \tag{A.34}$$

while the nugget effect results to be negligible. The values predicted from SAR and the GPS LOS projected observations are shown in Figure A.3. The $\underline{Y}$ vector is now that of LOS SAR deformations after their estimated mean removal, while Z is the GPS LOS projected deformation again after the same mean removal.

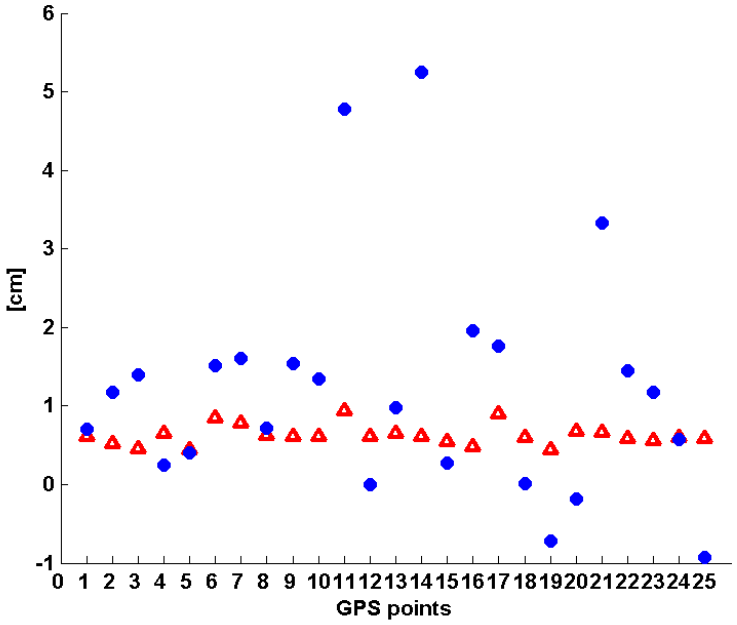

Figure A.3: SAR predicted LOS deformations (triangles)and GPS LOS projected observations (circles)

The GPS LOS deformations reduced by their average with the accordingly propagated standard deviation and the predicted values (from the SAR data, after the mean removal) with the relative prediction error standard deviation are reported in Table A.1. In the last column of the same table we report the corresponding statistics S values. By assuming S to be normally distributed, and by using a significance level $\alpha = 5\%$, as it can be seen from Table A.1, for all the points but two the hypothesis is accepted.

A.4 Conclusions

The conclusion about "equivalence" of SAR and GPS is somehow obscured by the relatively large variance of noise in GPS data. Anyway, by performing a proper noise propagation, the result is that the two data sets must be considered compatible but for two points, which have to be monitored separately. As a general remark, the assumption of zero average for $u(t)$ is critical. The full use of a kriging approach would show that basically the disagreement within the two data sets is in the average.

n.	Y [cm]	$\sigma_{\mathbf{Y}}$ [cm]	Z [cm]	$\sigma_{\mathbf{Z}}$ [cm]	S
1	0.00	0.36	0.09	0.66	0.01
2	-0.08	0.31	0.57	0.54	-1.13
3	-0.15	0.27	0.79	0.33	-2.22
4	0.04	0.34	-0.36	1.31	0.43
5	-0.16	0.29	-0.21	0.52	-0.39
6	0.25	0.31	0.91	0.45	-0.16
7	0.17	0.27	0.99	0.87	-0.25
8	0.02	0.36	0.11	0.73	0.89
9	0.00	0.36	0.93	0.88	-0.63
10	0.00	0.36	0.74	1.08	0.05
11	0.34	0.29	4.17	1.22	-1.29
12	0.01	0.36	-0.61	0.88	1.41
13	0.04	0.36	0.37	0.67	0.75
14	-0.00	0.36	4.64	0.95	-3.27
15	-0.06	0.36	-0.34	0.82	-0.45
16	-0.13	0.31	1.35	0.79	-1.82
17	0.29	0.30	1.15	1.58	0.62
18	-0.01	0.34	-0.60	1.17	0.29
19	-0.17	0.32	-1.33	0.55	0.79
20	0.08	0.32	-0.79	1.01	0.92
21	0.06	0.34	2.72	1.41	-0.97
22	-0.02	0.34	0.84	1.15	-0.65
23	-0.05	0.35	0.57	0.84	-0.81
24	-0.01	0.36	-0.04	0.41	-0.35
25	-0.02	0.36	-1.54	0.71	1.06

Table A.1: Test results: residual LOS deformation predicted from SAR (Y), standard deviation of the estimated prediction error (σ_Y), residual GPS LOS deformation (Z); standard deviation of the residual GPS LOS deformation (σ_Z), value of the statistic S.